Modeling and Characterization of Lithium Iron Phosphate Battery Electrodes

by

Mohammad Farkhondeh Borazjani

A thesis
presented to the University of Waterloo
in fulfillment of the
thesis requirement for the degree of
Doctor of Philosophy
in
Chemical Engineering

Waterloo, Ontario, Canada, 2016

AUTHOR'S DECLARATION

I hereby declare that I am the sole author of this thesis. This is a true copy of the thesis, including any required final revisions, as accepted by my examiners.

I understand that my thesis may be made electronically available to the public.

Abstract

A detailed understanding of lithiation/delithiation dynamics of battery active materials is crucial both for optimizing the existing technologies and for developing new materials. Among all, $LiFePO_4$ (LFP) has been subject to intensive fundamental research due to its intriguing phase-transformation dynamics which, unexpectedly, yields an outstanding rate capability and a long cycle life for electrodes made of this insertion material. In this thesis mathematical models are used as cheap and simple tools to investigate the electrochemical performance of LFP electrodes.

The thesis begins with the investigation of the solid-state transport (bulk effects) and electronic conductivity (surface effects) of LFP by means of variable solid-state diffusivity (VSSD) and resistive-reactant (RR) models, respectively. Both models are effectively validated against experimental galvanostatic discharge data over a wide range of applied currents. However, a very small solid-state diffusion coefficient ($\sim 10^{-19}\ m^2\ s^{-1}$) is required for both models to fit the experimental data. VSSD model features a particle-size distribution (PSD) which is estimated via model-experiment comparison. The fitted PSD, which is a geometric property and essentially invariable, requires to be different at different rates for the model to match experimental data; it is shifted towards smaller particles in order to accurately predict the electrode performance during galvanostatic discharge at higher applied currents. A contact-resistance distribution (CRD) replaces the PSD in the RR model. The fitted CRD turns out to be extremely broad spanning from ~ 1 to $\sim 10^2\ \Omega\ m^2$.

Next, following recent observations of ultra fast lithiation/delithiation of LFP, a simple mesoscopic model is developed which, in contrast to the first part of this research, completely disregards solid-state diffusion limitations. Instead, the model accounts for the inherent inhomogeneity of physico-chemical properties and bi-stable nature of phase-change insertion materials such as LFP with no consideration of any geometric detail of the active material. The entire active material domain is discretized into meso-scale units featuring basic thermodynamic (non-monotonic equilibrium potential as a function of composition) and kinetic (insertion/de-insertion resistance) properties. With only these two factors incorporated, the model is able to simultaneously explain a number of unique features associated with lithium iron phosphate electrochemical performance including the quasi-static potential hysteresis, high rate capability, cycle-path dependence, mismatch in electrode polarization during GITT when compared with continuous

cycling at the same current, bell-shaped current response in PITT and the most recently observed memory effect. Detailed analysis of the electrode dynamics suggests that a necessary condition for the memory effect to appear in an LFP electrode is the existence of a non-zero residual capacity at the onset of memory-release charging which may originate either from a non-zero initial SOC or from an imbalanced writing cycle. A memory effect should therefore not be observed in an electrode that has been preconditioned at extremely low currents (i.e., zero initial SOC) and has undergone an extremely slow memory-writing cycle (i.e., approaching a balanced cycle).

In the next step, the mesoscopic model developed at the unit level is incorporated into porous-electrode theory and validated by comparing the simulation results with experimental data from continuous and intermittent galvanostatic discharge of a commercial $LiFePO_4$ electrode at various operating conditions. A bimodal lognormal resistance distribution is assumed to account for disparity of insertion dynamics among elementary units.

Good agreement between the model and experimental data confirms the fidelity of the model. Investigation of three different GITT experiments suggests that the slow evolution of electrode polarization during each current pulse and the subsequent relaxation period is contributed by the inter-unit rather than intra-unit Li transport in $LiFePO_4$ electrodes. As such, GITT experiments once formulated for the determination of diffusion coefficient of inserted species in solid-solution systems may also be used to estimate the single-unit equilibrium potential (i.e., thermodynamic properties) as well as the dynamic properties (e.g., resistance distribution) of phase-change insertion materials.

Further analysis of the GITT experiments suggest that, depending on the overall depth-of-discharge of the electrode and the incremental depth-of-discharge of each GITT pulse, the solid-solution capacity available in the Li-rich end-member may be able to accommodate Li insertion entirely without the need for active (closed-circuit) phase transformation. Instead, redistribution of Li among units during relaxation equilibrates the solid-solution composition by transforming a few Li-poor units to Li-rich ones.

Despite rigorous research in the literature, this thesis presents the first attempt to quantitatively explain the above-mentioned irregularities simultaneously using a single unifying model and pinpoint the dominant contributing factors under various operating conditions.

A realistic account of porous-electrode effects in the experimental validation of the mesoscopic model requires accurate estimation of the electrolyte transport properties. In addition to

the modeling of phase-change electrodes, this thesis work presents a novel four-electrode-cell method to determine transport properties and the thermodynamic factor of concentrated binary electrolytes. The cell consists of two reference electrodes (i.e., potential sensors) in addition to the working and counter electrodes. The sensors measure the closed-circuit as well as open-circuit potential in response to an input current across the working and counter electrodes. The new method requires the application of only a single galvanostatic polarization pulse and appropriate concentration-cell experiments.

By fitting a suitable model to the data obtained from these experiments, the three independent transport properties of a concentrated binary electrolyte, namely, ionic conductivity, diffusion coefficient and transference number as well as the thermodynamic factor can be determined. In particular, the measurement of the closed-circuit potential using this cell provides a simpler and essentially more accurate means to estimate the transference number than the conventional semi-infinite diffusion method.

Acknowledgements

First and foremost, I am deeply indebted to my advisors Prof. Michael Fowler and Prof. Mark Pritzker for continuous support they have given to me during my PhD, for their broad knowledge, patience, warm encouragement and thoughtful guidance. They were always there to listen and to give advice. I greatly appreciate their efforts to fund the project and to pay me with no hesitation and gratefully acknowledge the many research opportunities they created for me during these years.

I am very grateful to Prof. Thomas Fuller for graciously agreeing to be my external examiner. I would also like to express my gratitude to the rest of my thesis committee: Prof. Zhongwei Chen, Prof. Aiping Yu and Prof. Roydon Fraser for patiently reviewing my work. Special thanks to Prof. Chen and Prof. Yu for generously allowing me to use their research facilities.

My sincere thanks to Dr. Charles Delacourt, whose challenges and insightful comments have provided an invaluable input to this project. In addition to our research collaboration, I greatly value the close personal rapport that Charles and I have forged over the years.

I am very thankful to my good friend Dr. Mohammadhosein Safari for valuable discussions and constructive feedbacks. Many thanks to Bert Habicher for his kind assistance in fabricating the four-electrode cell and to my lab mates and fellow grad students Zhiyu Mao, Manoj Mathew, Muneendra Prasad, Ushnik Mukherjee, Zachary Cano and John Cotton and the co-op students Andrew Jiang, Simon Liu, Steven Sherman and Melody Gao who helped me in all respects during the completion of my PhD.

Last, but not least, I thank my family for their endless support and encouragement beyond geographic distances without which this thesis would never have been written.

Dedication

To my mother, Fatemeh whose unconditional love, support and encouragement have nourished me throughout life.

Table of Contents

List of Figures

List of Tables

List of Symbols

A	symbol for single salt
A_1, A_2	Margules model parameters
a_k	active surface area of the k^{th} LFP particle per unit volume of the electrode, $\text{m}^2\ \text{m}^{-3}$
B, C	parameters of the high-order term in the thermodynamic model
$c_{\max}$	maximum concentration of Li-intercalated sites (LiS) in LFP, $\text{mol}\ \text{m}^{-3}$
c	electrolyte concentration, $\text{mol}\ \text{m}^{-3}$
c_i	concentration of species i in the solution, $\text{mol}\ \text{m}^{-3}$
c_{T}	total concentration of solution, $\text{mol}\ \text{m}^{-3}$
c_q	concentration of reacting species in $q = \text{PS, WE, CE}$, $\text{mol}\ \text{m}^{-3}$
c_{ini}	initial electrolyte concentration, $\text{mol}\ \text{m}^{-3}$
$\mathcal{D}$	diffusion coefficient of electrolyte based on a thermodynamic driving force, $\text{m}^2\ \text{s}^{-1}$
$\mathcal{D}_{ij}$	Stefan-Maxwell diffusion coefficients, $\text{m}^2\ \text{s}^{-1}$
D	chemical diffusion coefficient of electrolyte on a molar basis, $\text{m}^2\ \text{s}^{-1}$
$\mathcal{D}_{\text{LiS}}$	binary solid-state diffusion coefficient, $\text{m}^2\ \text{s}^{-1}$
$D_{\text{LiS},k}$	chemical solid-state diffusion coefficient, $\text{m}^2\ \text{s}^{-1}$
E	electric field applied to electrolyte, $\text{V}\ \text{m}^{-1}$
e^-	symbol for electron
F	Faraday constant, 96,487 C mol^{-1}
f	mixing parameter
f_i	molar activity coefficient of species i in solution
$f_\pm$	mean molar activity coefficient of electrolyte
g	interaction coefficient (regular solution model)
i^0	exchange current density for LFP lithiation/delithiation independent of solid-state surface concentration referred to the active surface area, $\text{A}\ \text{m}^{-2}$
i_k^0	exchange current density for lithiation/delithiation of the k^{th} particle group referred to the active surface area, $\text{A}\ \text{m}^{-2}$
$i_{\text{n},k}$	current density normal to the surface of the k^{th} LFP particle, $\text{A}\ \text{m}^{-2}$
i_k	partial current entering/leaving the k^{th} LFP unit, $\text{A}\ \text{mol}^{-1}$

i_{Li}^{0}	effective exchange current density of lithium foil counter electrode based on a 1 M reference concentration, referred to the counter electrode area, A m^{-2}
$\mathbf{i}_1$	electronic current density through porous electrode referred to the geometric area, A m^{-2}
$\mathbf{i}_2, \mathbf{i}$	ionic current density across solution phase referred to the geometric area, A m^{-2}
I	total current density referred to the geometric area, A m^{-2}
I_{app}	applied current, A
k_q^0	charge-transfer reaction rate constant $q = \mathrm{Li}, \mathrm{LFP}, \mathrm{PS}, \mathrm{WE}, \mathrm{CE}$
l	component thickness, m
L	length of the four-electrode cell, m
M_i	molecular weight of species i, g mol^{-1}
M_e	molar weight of electrolyte, g mol^{-1}
M_0	molar weight of solvent, g mol^{-1}
$\mathrm{M}_i^{z_i}$	symbol for species i in solution
n	number of electrons involved in electrode reaction
N	number of elementary-unit bins (Chapter 4 and 5), number of species in the solution (Chapter 6)
$\mathbf{N}_i$	molar flux density of species i, mol m^2 s^{-1}
$N_{\mathrm{LiS},k}$	flux density of intercalated lithium (LiS) in the k^{th} LFP particle, mol m^2 s^{-1}
p	pressure, Pa
P_m	probability density function of the m^{th} resistance distribution
r	radial distance from center, m
r_f	borosilicate glass fiber radius, m
$\hat{\mathbf{r}}$	radial component unit vector
R	universal gas constant, 8.314 J mol^{-1} K
R_{cell}	cell radius, m
R_k	ohmic resistance of the k^{th} LFP elementary-unit bin, Ω mol
$R_{\mathrm{p},k}$	radius of the k^{th} LFP particle, m
$R_{\mathrm{c},k}$	conductive matrix/active material contact resistance of the k^{th} LFP particle, Ω m^2
$\bar{R}$	mean resistance, Ω mol

R_{eq}	equivalent resistance, Ω mol
R_{min}	minimum resistance, Ω mol
R_{max}	maximum resistance, Ω mol
s_i	stoichiometric coefficient of species i in electrode reaction
S	standard deviation of normal resistance distribution, Ω mol
t	time, s
t_+^0	transference number of cation (i.e., Li^+) in the solution
T	temperature, K
U_k	equilibrium potential of the k^{th} LFP unit versus Li, V
$U_{s,k}$	equilibrium potential at the surface of the k^{th} LFP particle versus Li, V
U^0	standard equilibrium potential of LFP versus Li, V
U_q	equilibrium potential of electrode $q = \mathrm{PS, WE, CE}$ vs. reference electrode used to define solution electric potential, V
$\mathbf{v}$	mass-average velocity of solution, m s^{-1}
$\mathbf{v}_i$	velocity of species i in solution, m s^{-1}
$\bar{V}_i$	partial molar volume of species i in solution, m^3 mol^{-1}
$\bar{V}_e$	partial molar volume of electrolyte in solution, m^3 mol^{-1}
x	distance from the lithium foil electrode towards the cathode current collector, m
y_i	mole fraction of species i in solution
y_k	mole fraction of Li-intercalated sites (LiS) in the k^{th} elementary-unit bin (or particle)
$y_{s,k}$	mole fraction of Li-intercalated sites at the surface of the k^{th} LFP particle
z	axial distance along centerline of the four-electrode cell, m
z_i	charge number of species i in solution
$z_{\mathrm{eq},l}$	equilibrium locus between cathodic and anodic poles of the potential sensor l, m
$\hat{\mathbf{z}}$	axial component unit vector

Greek

α	thermodynamic factor of electrolyte
$\alpha_{\mathrm{LiS},k}$	solid-state thermodynamic factor inside the k^{th} LFP particle
β_q	charge transfer coefficient $q = \mathrm{Li, LFP, PS, WE, CE}$

γ	Bruggeman exponent
Γ	concentration polarization, V
δ	potential sensor width, m
ε_k	fraction of the k^{th} LFP bin with respect to the total active material volume
ε_t	total volume of the cathode active material per unit volume of the electrode
ε	component porosity
η_k	Insertion/de-insertion overpotential of the k^{th} LFP unit bin, V
$\eta_{\text{PS},l}$	overpotential at interface between solution and potential sensor l, V
κ	ionic conductivity of electrolyte, S m^{-1}
K	permeability of separator, m^2
λ	spacing between working/counter electrode and potential sensor, m
μ	dynamic viscosity of solution, Pa.s
μ_i	chemical potential of species i in solution, J mol^{-1}
μ_e	chemical potential of electrolyte, J mol^{-1}
μ_e^θ	chemical potential of electrolyte at the secondary reference state θ, J mol^{-1}
μ_m	mean of $\ln R_k$ for the m^{th} log-normal distribution
ν	total number of moles of ions into which one mole of salt dissociates
ν_i	number of moles of ion i produced by salt dissolution
ξ	Bruggeman coefficient
ρ	solution density, kg m^{-3}
σ	bulk electronic conductivity of cathode, S m^{-1}
σ_m	standard deviation of $\ln R_k$ for the m^{th} log-normal distribution
$\Phi_{1,k}$	solid-phase electrical potential at the surface of the k^{th} LFP particle, V
Φ_1	electrical potential of the cathode conductive matrix, V
Φ_2	electrical potential of electrolyte, V
Φ	electrical potential of electrode in Chapter 4 and of electrolyte in Chapter 6, V
Φ_q	electrical potential of electrode $q = \text{Li, WE, CE, PS}$, V

Subscripts:

cat	cathode

sep	separator
eff	effective value
Li	Li foil reference/counter electrode
LFP	$LiFePO_4$
WE	working electrode
CE	counter electrode
PS	potential sensor

List of Acronyms

AM	active material
CCV	closed-Circuit Voltage
CE	counter electrode
CRD	contact-resistance distribution
CSSD	constant solid-State diffusivity
DMC	dimethyl carbonate
DEC	diethyl carbonate
EC	ethylene carbonate
EPDM	ethylene propylene diene monomer
EV	electric vehicle
FSR	full-scale range
GF	glass microfiber filter
GITT	galvanostatic intermittent titration technique
HEV	hybrid electric vehicle
ICV	internal combustion engine
IEA	International Energy Agency
KJMA	Kolmogorov-Johnson-Mehl-Avrami
LDV	light-duty vehicle
LFP	lithium iron phosphate
LIB	lithium-ion battery
MRR	modified resistive-reactant model
MUMPS	multifrontal massively parallel sparse direct solver
MRI	magnetic resonance imaging
NMP	N-Methyl-2-pyrrolidone
NMR	nuclear magnetic resonance
OCP	open-circuit potential
OCV	open-circuit voltage
OECD	Organization for Economic Co-operation and Development
PHEV	plug-in hybrid electric vehicle

PITT	potentiostatic intermittent titration technique
PS	potential sensor
PSD	particle-size distribution
PTFE	polytetrafluoroethylene
RR	resistive-reactant
RD	resistance distribution
SEI	solid-electrolyte interphase
SEM	scanning electron microscopy
SEQ	single-unit equilibrium potential
SOC	state of charge
TEM	transmission electron microscopy
VSSD	variable solid-state diffusivity
WE	working electrode
XRD	X-rate diffraction

Chapter 1
Introduction

Transportation is responsible for 19% of worldwide energy consumption [1] which mainly comes from fossil fuels (about 60% of total oil consumption in OECD countries). Ever-growing population, modernization of the society and economic growth especially in developing countries could lead to a two to three fold increase in global energy consumption compared to current levels [2]. The continual depletion of fossil-fuel resources and possible environmental problems associated with their use has driven decision makers to seek sustainable alternatives. Based on assumptions regarding future technological progress, several optimistic scenarios have been proposed such as the ACT and BLUE Map according to which energy consumption can be reduced to 67% of current levels. Based on the BLUE Map scenario, the use of conventional internal combustion vehicles (ICV) will constitute only about 10% of the light-duty vehicle (LDV) market, while electric (EV) and hybrid electric vehicles (HEV) will contribute more than 50% of total LDV sales by 2050, not to mention possible electrification of buses and medium-duty trucks (Figure 1-1).

Apart from widespread development of renewable energy generation plants/farms, this revolutionary vision requires the extensive use of on-board electrochemical energy storage systems (i.e., batteries and supercapacitors). Due to their higher cell voltage, longer lifetime and superior energy and power density (2 to 3 times those of conventional rechargeable batteries) [3], lithium-ion batteries (LIB) are being counted on to play a key role in this strategic roadmap.

The successful development of Li-ion batteries suitable for this role necessitates tremendous fundamental research in material design and engineering efforts for cell optimization. Many factors such as electrode composition, electrode thickness and particle size are important for cell design. However, it is impractical and expensive to optimize cell design purely by experimental means. When coupled with experimental measurements, mathematical modeling is a valuable step in the design process and can help identify the role of each parameter and lead to various possible designs for a given cell chemistry. Moreover, rigorous investigation of battery degradation and battery life prediction is made simpler by using the mathematical models and comparing simulation results with experimental data.

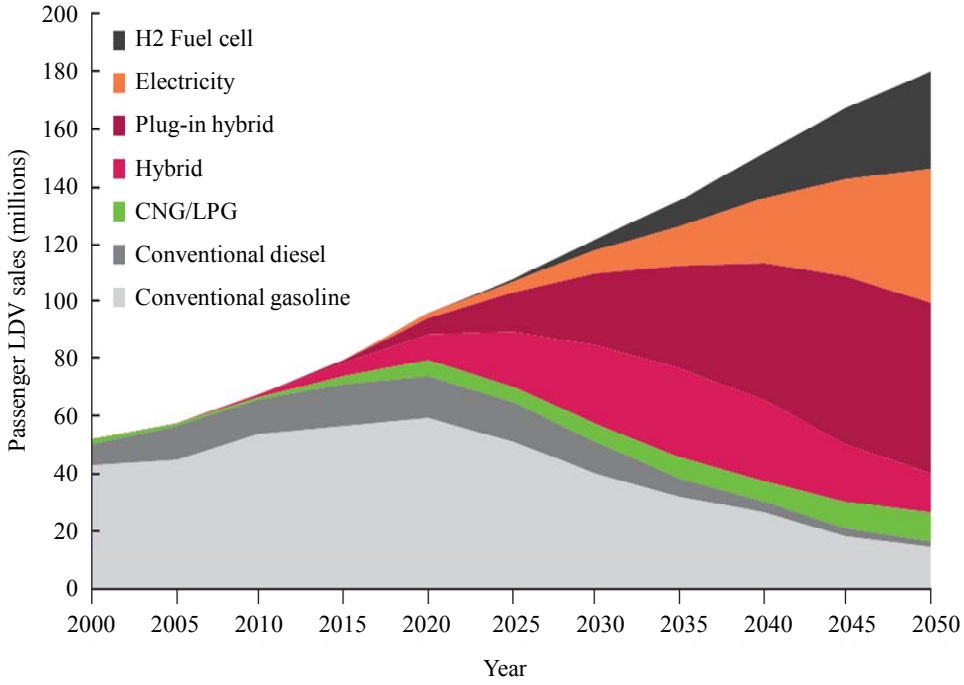

Figure 1-1. Annual light-duty vehicle sales by technology type according to BLUE Map scenario. Adopted from IEA's 2011 Technology Roadmap report on electric and plug-in and hybrid electric vehicles, Ref. [4].

1.1 Li-Ion Battery Technology

A battery is a transducer that converts chemical energy into electrical energy and vice versa [5]. Lithium-ion batteries are categorized as secondary batteries (rechargeable batteries); they can be reused many times in contrast with the primary batteries that are used once and discarded. A lithium-ion battery consists of two composite electrodes coated on metallic current collectors (i.e., copper for the positive electrode and aluminum for the negative electrode) and separated by an ion-conducting and electron-insulating electrolytic medium. The electrolyte conducts lithium ions from the positive electrode (cathode) to the negative electrode (anode) during charge and from the anode to the cathode during discharge. The electrons, on the other hand, flow through an external path to close the circuit and deliver electric work to a load during discharge or gain energy from a power supplier during charge. The electrolyte can be a solid ceramic, a polymer, or a non-aqueous liquid soaked in a porous separator. Composite electrodes are composed of an electrochemically active material (AM), conductive filler, polymeric binder and electrolyte-filled pores.

The operation of a rechargeable lithium-ion battery is based on the "intercalation" concept where the active material reversibly accepts/donates lithium ions with no alteration of its crystallographic structure. Graphite, $LiCoO_2$, $LiFePO_4$ are among intercalation compounds used in LIBs. The negative electrode contains a low-potential active material (e.g., graphite) whereas a high-potential active material (e.g., $LiFePO_4$) is used in the cathode. The following reactions occur at the surface of the anode and cathode active materials in a cell undergoing discharge:

$$\begin{aligned} &Li_xC_6 \rightarrow C_6 + xLi^+ + xe^-, \text{anode delithiation} \\ &FePO_4 + xLi^+ + xe^- \rightarrow Li_xFePO_4, \text{cathode lithiation} \\ &\text{----------} \\ &Li_xC_6 + FePO_4 \rightarrow C_6 + Li_xFePO_4, \text{cell discharge} \end{aligned} \tag{5-1}$$

where $0 < x < 1$. During cell discharge, lithium ions tend to leave the anode active material and, after traveling through the electrolyte, intercalate into the cathode particles. In other words, one electrode active material ($LiFePO_4$) is electrochemically reduced at the expense of the other (graphite) being oxidized releasing stored energy. This process involves 2 charge-transfer reactions and various mass transport processes (e.g., diffusion inside the solid particles) that impose limitations on the deliverable power; the larger the C-rate (the rate of 1C is the theoretical amount of current a battery delivers when fully discharged in one hour), the higher are the transport losses and the lower is the power received from the cell. Figure 1-2 shows a schematic of fundamental processes that occur in a lithium-ion battery.

Despite intensive research on high capacity anode materials such as silicon and Li-alloys, graphite is still the most common negative electrode material in today's Li-ion batteries due to its abundance, low cost and satisfactory electrochemical performance ($372\ \text{mAh}\ g^{-1}$ of theoretical capacity). Layered lithium cobalt oxide ($LiCoO_2$), on the other hand, was the first cathode material introduced into commercial Li-ion batteries manufactured by Sony Corporation in 1991 [3]. The limited electrochemical and thermal stability and cost of this compound (i.e., depletable cobalt) in addition to the requirements of long calendar and cycle life targeted for EV/HEV battery packs have motivated investigations into new cathode chemistries for large-scale LIBs [6]. Lithium iron phosphate has recently emerged as a suitable alternative to other high-potential positive electrode active materials due its longevity, low cost and compatibility with the environment.

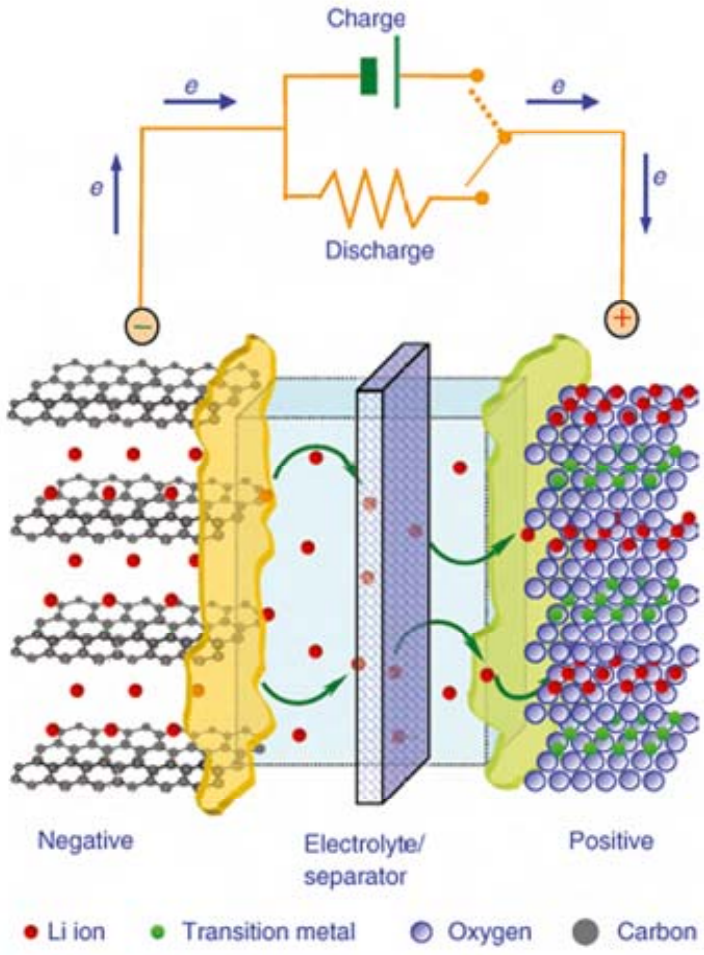

Figure 1-2. Schematic of a lithium-ion battery with the anode and cathode intercalation active materials [7].

1.2 Motivation

Physics-based mathematical models are valuable tools for the design and optimization of Li-ion batteries given that the underlying physico-chemical phenomena are well understood and physical properties are known. More specifically, they allow optimization of design parameters such as electrode thickness, porosity, particle size, electrode formulation, chemical composition, manufacturing process and mechanical cell design (e.g., pouch, cylindrical, prismatic, etc.) for a specific application. They also help the end-user to assess electrochemical performance of the cells and their life cycle and to design proper thermal management systems for the final large-scale battery packs on-board EVs/HEVs.

In conjunction with *in-situ* and ex-situ experimental observations (electrochemical and non-electrochemical), physics-based continuum modeling can help to fathom physico-chemical processes occurring during electrode charge/discharge, which are not well understood, and disentangle the obscured complexities. As such, experimental observations and theoretical analysis combined can yield a detailed description of the electrode behavior.

Among all Li insertion materials, $LiFePO_4$ has recently emerged as a suitable positive electrode material due to its durability, low cost and minimal environmental impact [6, 8]. Lithiation/delithiation of LFP occurs through a biphasic mechanism between Li-rich $Li_{1-\epsilon'}FePO_4$ and Li-poor $Li_{\epsilon}FePO_4$ end-members [6, 9] which have the same crystal structure (*Pnma* space group) but differ in their Li content and lattice parameter [6]. Its unexpectedly outstanding performance and irregular electrochemical behavior have made LFP a perfect model to study oddities associated with the lithiation/delithiation of phase-change insertion materials. Aside from the flat equilibrium potential, LFP electrodes exhibit other unusual qualities, namely: (i) outstanding rate capability [10], (ii) development of positive intensities between the X-ray diffraction (XRD) peaks of the end-members during high-rate cycling [11, 12], (iii) cycle-path dependence [13], (iv) quasi-static potential hysteresis [14], (v) non-monotonic current response to potential steps [15], (vi) polarization mismatch between the electrode responses to intermittent and continuous galvanostatic operations [16, 17] and (vii) memory effect. Despite rigorous research in the literature, a single unifying model that can predict all of the above-mentioned irregularities and pinpoint the dominant contributing factors is still lacking.

Electrode charge/discharge dynamics is influenced not only by kinetic and transport processes at the particle level but also by diffusion and ionic migration processes in the electrolyte and electronic percolation in the solid matrix at the electrode level. Therefore, accurate analysis of the electrode performance requires the electrode-level parameters to be known. The power of batteries is strongly dependent upon the electrolyte transport properties. Thus, it is not surprising that the search for ever more effective battery electrolytes has received a great deal of attention in recent years [18-30]. The conventional methods for the estimation of the transport properties of an electrolyte are time-consuming, inaccurate, rare and have been limited to a few of the most commonly used electrolytes [31-44]. Faster progress in developing new batteries will be possible if the techniques to measure these properties can be made as fast and accurate as possible.

1.3 Objectives

Multi-scale physics-based battery models are required both for cell design and development by the manufacturer and for performance analysis and battery management systems by the consumer (e.g., car manufacturers). An inadequate model at the particle and electrode scales can yield misleading implications and inaccurate predictions which, overall, increase the cost of the energy storage system. It has been particularly challenging to model phase-transforming insertion electrodes.

The objective of this thesis consists in two parts:

- To develop a mathematical model for $LiFePO_4$ as a model phase-change insertion material that is able to describe the electrode charge/discharge dynamics under various operating conditions. The model should be able to shed light on the internal dynamics of phase-transforming insertion electrodes, explain unique phenomena observed in $LiFePO_4$ that have been enumerated in section 1.2 and accurately predict the experimental charge/discharge data.

- To develop a fast and reliable method to estimate transport and thermodynamic properties of concentrated battery electrolytes. The characterization method involves a physics-based mathematical model that is compared with experimental data with transport properties as fitting parameters.

The proposed electrode model and the estimated physical properties are at the very core of electrochemical and thermal models at the cell, module and pack scales which are extensively used by engineers for performance analysis, thermal management and degradation studies or as a part of vehicle powertrain simulators under various operating conditions.

1.4 Thesis Outline

This thesis will continue in Chapter 2 with a brief review of experimental observations of $LiFePO_4$ lithiation/delithiation dynamics reported in the literature. Various approaches for mathematical modeling of this phase-change insertion compound are also discussed. Two bulk-transport-limited and surface-transport-limited models are developed and compared in Chapter 3 to investigate the applicability of conventional models to the simulation of $LiFePO_4$ electrodes. Following the shortcomings of these models, a simple mesoscopic model is proposed in Chapter 4 that simulates phase transformation and is able to explain peculiar behavior of LFP electrode including quasi-static

potential hysteresis and memory effect during electrochemical operation. Further analysis of $LiFePO_4$ lithiation/delithiation dynamics is presented in Chapter 5; the mesoscopic phase-transformation model is embedded into the well-established porous-electrode theory in this chapter. The resulting model is validated by comparing it with experimental data from continuous and intermittent galvanostatic discharge of a commercial LFP electrode, given the transport and thermodynamic properties of the electrolyte estimated in Chapter 6.

Chapter 6 presents a novel four-electrode electrochemical-cell method for the estimation of transport and thermodynamic properties of concentrated binary electrolytes. The cell design is thoroughly discussed and a general mathematical model for the property estimation is elaborated in this chapter. The proposed methodology is applied to two commercially available battery electrolytes one of which is used in the Li/LFP half-cell setup used to acquire experimental data for the mesoscopic model validation in Chapter 5. The final chapter presents thesis conclusions and provides recommendations for future work.

Chapter 2
Background and Literature Review

2.1 $LiFePO_4$ Electrode

First reported by Padhi et al. [6, 8], $LiFePO_4$ is now a serious rival to other well-established high-voltage insertion compounds for use in high power Li-ion batteries. Special packing of PO_4 polyanion tetrahedra and FeO_6 octahedra making up the phospho-olivine structure gives unique properties to this material. LFP exhibits remarkable thermal stability [45] as well as reasonable air and humidity stability [46] that makes it easy to process and handle. Additionally, the Fe^{3+}/Fe^{2+} redox potential is well located in the stability window of most commercially available liquid and polymer electrolytes resulting in high electrochemical stability and a potentially long battery life [47]. The abundance of Fe makes this non-toxic iron-based cathode material relatively cheap and environmentally benign.

The main drawback of this electrode material, however, is its low intrinsic electronic conductivity ($\sim 10^{-7}$ S m^{-1}) [48-51]. The application of a carbon coating onto the particles is a widely accepted method to overcome their low electronic conductivity [49, 50]. Another approach of doping LFP with supervalent cations (e.g., Nb^{5+} and Zr^{4+}) is claimed to dramatically improve the electronic conductivity (~ 8 orders of magnitude increase compared to the pristine LFP sample) [52], although some researchers have questioned the doping effects and have attributed the conductivity enhancement to the formation of secondary conductive phases that provide electrical conduits over the surface of the particles in the same way as a carbon coating operates [48, 51, 53]. For many years, Li diffusion inside LFP particles (i.e., estimated diffusion coefficient of $\sim 10^{-17} - 10^{-20}$ m^2 s^{-1}) was believed to be another main factor that limits the performance of bulk LFP for which the reduction of the particle size to nano-scale was considered as the best strategy to minimize the diffusion length and thus speed up diffusion within its structure [54, 55].

2.1.1 Thermodynamics and Experimental Observations

Lithium insertion/deinsertion into/from LFP is a two-phase process. This process is characterized by a flat equilibrium potential curve, i.e., an equilibrium potential independent of degree of lithiation over a wide range of Li concentration, which, according to Gibbs' phase rule, is the signature of a biphasic system (Figure 2-1). This is in line with crystallographic studies where the diffraction peaks corresponding to one phase lose intensity in favor of growing peaks of the second phase at different

states of charge (SOC) [6, 56]. However, the measured lattice parameters differ slightly from those of stoichiometric $FePO_4$ and $LiFePO_4$ end-members suggesting that the two phases in equilibrium are in fact lithium-poor $Li_\epsilon FePO_4$ and Li-rich $Li_{1-\epsilon'}FePO_4$ solid solutions (ϵ and $\epsilon' \ll 1$), leading to two narrow solid-solution regions at the onset and the end of the electrode potential profile [56, 57]. The two phases are isostructural and belong to the same *Pnma* space group with slightly different unit-cell parameters [58].

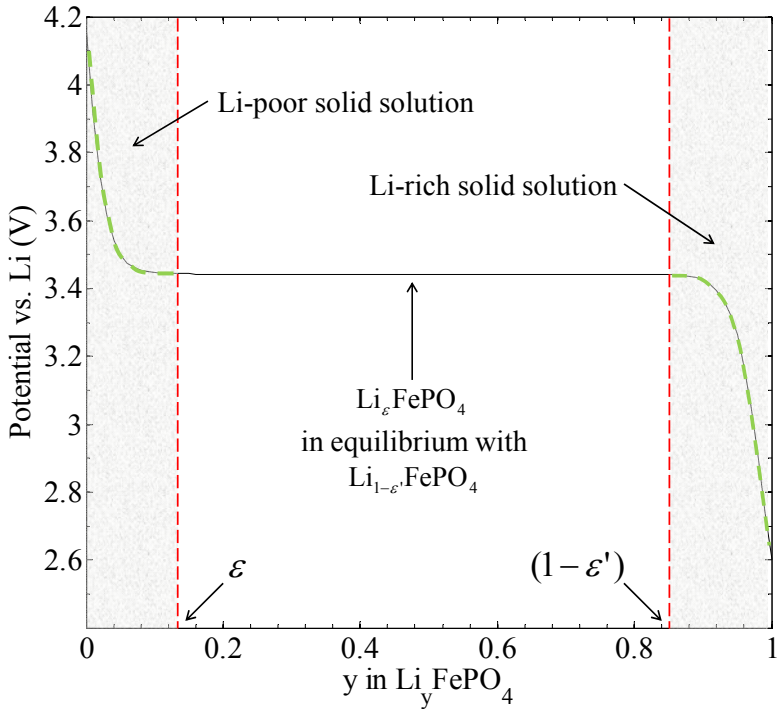

Figure 2-1. Equilibrium potential of an LFP electrode estimated by averaging low rate (C/100) galvanostatic charge and discharge data [59].

Although a great deal of research has been focused on room temperature characterization of the system, thermodynamics of phase mixing/separation at different temperatures must be determined. Delacourt et al. [60, 61] and Dodd et al. [58, 62] separately compiled phase diagrams for Li_yFePO_4 ($0 \leq y \leq 1$) based on X-ray diffraction analysis of LFP powder at different temperatures and Li content, shown in Figure 2-2. The solid-solution ranges expand as temperature increases. At elevated temperatures (i.e., greater than $\sim 350℃$ and less than $\sim 500℃$), the two triphylite ($Li_\epsilon FePO_4$) and heterosite ($Li_{1-\epsilon'}FePO_4$) phases transform to a single solid-solution phase which can transform back to the two-phase arrangement as temperature is reduced. However, it has been shown

that, under certain conditions, LFP solid solution can recast into a metastable intermediate phase ($Li_{0.64}FePO_4$, eutectoid composition) upon cooling to room temperature [60, 61]. The appearance of the eutectoid point renders LFP phase diagram to be significantly different from typical binary immiscible systems (i.e., dome-shaped temperature-composition curve). LFP decomposes to non-olivine compounds at temperatures greater than ~ 500°C [61]. First-principles calculations by Zhou et al. [63] have confirmed the experimental phase diagram and attribute the eutectoid behavior to the electronic rather than ionic configuration entropy. The increased entropy at high temperatures accounts for the shrinkage of the miscibility gap between the two phases and the formation a stable solid-solution phase prior to chemical decomposition.

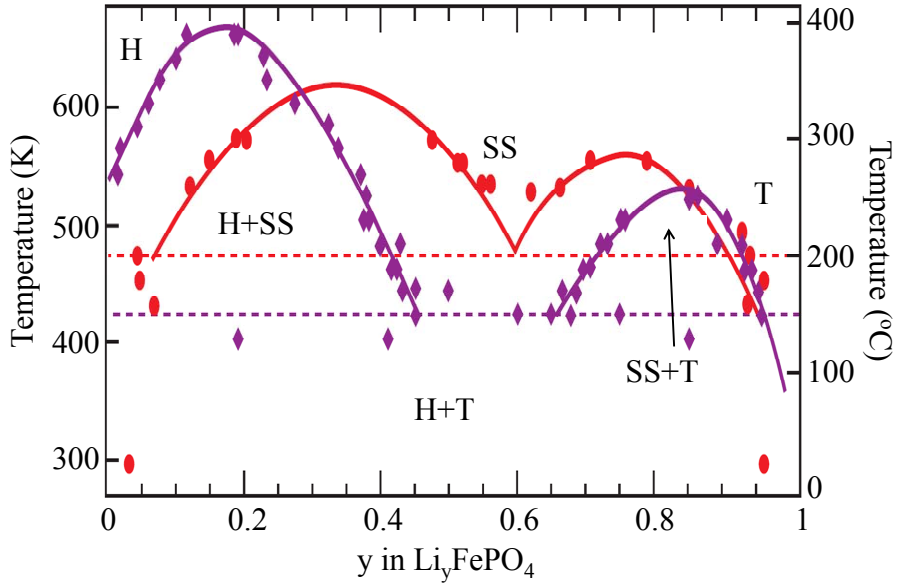

Figure 2-2. Experimental phase diagram of LFP by Dodd et al. [58] (red circles) and Delacourt et al. [61] (purple diamonds). H stands or heterosite, T for triphylite and SS for solid solution. Horizontal lines indicate the eutectoid transition temperature. The figure is adopted from Ref. [64].

In addition to the effect of temperature, particle size has been found to dramatically influence the solubility limits of the two phases in an LFP particle. Gibot et al. [65] demonstrated that, by reducing the particle size to 40 nm, room-temperature galvanostatic charge/discharge of an LFP electrode exhibits a sloping potential curve even at very low rates (C/40) while the lattice parameter variations follow Vegard's law (i.e., signature of solid-solution systems). Similar observations were reported in Ref. [66] suggesting that there exists a critical particle size below which the miscibility

gap completely disappears. This size-effect is explained by the excess surface, interface and coherent stress-strain energy penalties destabilizing the coexistence of the two phases inside a single LFP particle.

High-resolution electron microscopy study of micron-sized LFP particles by Chen et al. [67] and Laffont et al. [68] confirmed the theoretical calculations [69, 70] that Li diffusion in the bulk occurs strongly anisotropically along the *b*-axis in the *Pnma* space group. Their observations suggest that the Li insertion/de-insertion occurs at the phase boundary parallel to the *bc* plane progressing in the direction of *a*-axis. In a separate research Chen et al. [71] reported a contradictory observation where the phase boundary lie on the *ac* plane perpendicular to the 1-D diffusion channels in solid-solution samples cooled to room temperature. A similar observation was recently reported using an *in-situ* atomic-scale transmission electron microscopy (TEM) of LFP in a micro-electrochemical cell [72].

The advent of high resolution phase mapping tools has lead to more accurate characterization of the charge/discharge dynamics of LFP electrodes [11, 12, 73-82]. Maier et al. [77] tracked the phase boundary propagation in a large millimeter-scale LFP single crystal during chemical delithiation and observed the formation of a large amount of microstructural defects such as pores and cracks. Cabana et al. [78] used soft X-ray ptychographic microscopy (with a spatial resolution of ~ 5 nm) and X-ray absorption spectroscopy to investigate the chemical and morphological evolution of micron, submicron and nano LFP particles upon chemical delithiation. They observed a complex spatial distribution of the new phase inside larger micron and submicron particles which correlates well with the distribution of microstructural defects (cracks and pores) [78], in line with the observation of Maier et al. [77] and others [79, 80]. Cabana et al. [78] also reported biphasic nano particles with very few cracks indicating that the smaller particles could withstand coherency stresses and remain mechanically stable during lithiation/delithiation [78].

Unlike chemical delithiation studies, *in-situ* [11, 12, 81, 82], and ex-situ [74-76] phase mapping of electrochemically delithiated LFP electrodes made of nano particles have ubiquitously reported a discrete pattern for the lithiation/delithiation of particles in the electrodes. The two phases appear to be distributed between one group of particles containing the Li-poor phase and another group containing the Li-rich phase in contrast to the coexistence of both phases within chemically delithiated LFP single particles (be it coherent or incoherent). These observations are interpreted as being caused by the suppression of intra-particle phase boundary formation and propagation; instead,

they suggest that inter-particle exchange of Li^+ ions and electrons (i.e., via the electrolyte and conductive matrix, respectively) takes place in the electrode and is less energetically expensive than intra-particle boundary formation and propagation [14, 83].

The above observations outline three major lithiation/delithiation mechanisms: i) intra-particle phase transformation causing mechanical damages (incoherent) [77-80], ii) intra-particle phase transformation with no mechanical damages (coherent) [78] and iii) inter-particle phase transformation in an ensemble of electronically and ionically connected particles which are present either in a Li-rich or Li-poor single solid-solution phase [11, 12, 74-76, 81, 82]. The dominant mechanism is determined by factors such as particle size and shape [78, 84], quality of conductive coating (both ionic and electronic), synthesis route, structural defects, electrode formulation and microstructure, temperature, applied potential/current [11, 12], and even the conditioning cycles or cycling history [77].

2.1.2 Mathematical Modeling

Conventional continuum models describe FP-LFP phase transformation by juxtaposing the two phases within the bulk throughout the charge/discharge process [15, 16, 57, 85-100]; the formed phase boundary, either sharp or diffuse, travels across the material at a rate closely proportional to the charge/discharge rate of the electrode.

A group of these models depicts the electrochemically-driven phase transition using statistical nucleation and growth formulations such as the Kolmogorov-Johnson-Mehl-Avrami (KJMA) model [15, 98, 99]. A second group including the reformulated phase-field models for open systems relies on the spontaneous spinodal decomposition mechanism and automatically tracks the phase boundary by minimizing the Cahn-Hilliard free energy functional [85, 86, 90, 91, 93-97]. Core-shell-type models constitute the third group of models and locate a well-defined interface between the two phases. Some models of that group attribute the phase-change kinetics to interface mobility [57, 87-89, 92, 101]. Since the two phases differ in composition, diffusion processes transporting species to the reacting interface can be limiting depending on the kinetics of the phase change. Finally, the fourth group of models describes LFP insertion as a strongly non-ideal solid-solution process in which the phase boundary itself is shaped on the basis of variable solid-state lithium diffusivity that goes through a minimum in the intermediate Li composition range [16, 100, 102].

Based on an analogy with the inflation/deflation of a system of interconnected rubber balloons [103, 104], Dreyer and co-workers developed a so-called "many-particle" model where particles in a porous electrode are allowed to randomly exchange Li^+ ions and electrons through the electrolyte and the conductive matrix, respectively [14, 83]. Dreyer's many-particle model, however, does not rely on any specific mechanism for mass transfer/phase transition within individual particles and only concludes the thermodynamics of the porous electrode.

2.2 Transport Property measurement of Concentrated Binary Electrolytes

Different electrode systems including insertion- and conversion-type as well as sulfur and air electrodes have been developed in recent years and are able to store various charge carriers such as Li^+, Na^+, Mg^{2+}, Zn^{2+}, etc. In order for a battery to be effective, high potential (i.e., cathode) and low potential (i.e., anode) electrodes must be combined and separated by an electrolyte that enables ionic transport between the two electrodes. An ideal electrolyte should be chemically stable with respect to the anode and cathode potentials to guarantee long battery life. As a result, the operating battery voltage is constrained by the stability window of the electrolyte. Therefore, any improvement in the electrolyte chemistry (and additives) that leads to a more stable electrode/electrolyte interface will improve the energy and power density of a given anode/cathode pair [18]. At the same time, the power is also dependent upon the electrolyte transport properties. In addition to conventional rechargeable batteries, redox flow systems in which an anolyte and a catholyte are responsible for both charge storage and transport, are experiencing a rapid growth for large-scale stationary applications [105, 106]. Thus, it is not surprising that the search for ever more effective battery electrolytes has received a great deal of attention in recent years [18-30]. Since the effectiveness of these electrolytes depends strongly on their transport properties, faster progress in developing new and useful batteries will be possible if the techniques to measure these properties can be made as straightforward and accurate as possible.

In most cases, the electrolyte is a concentrated solution of one salt dissolved in one or more solvents [18]. According to the Stefan-Maxwell equation, full characterization of a multi-component concentrated solution requires estimation of $N(N-1)/2$ parameters where N is the number of independent species in the solution [107]. Despite a well-developed theory for concentrated solutions, direct estimation of its parameters is often impracticable for multi-component systems with more than three species and limited, in practice, to binary electrolytes (i.e., $N = 3$) [107]. In a binary electrolyte where the solution of a binary salt in a single solvent produces three species (i.e., one cation, one

anion and one solvent), three independent properties need to be known. These Stefan-Maxwell parameters which are all concentration- and temperature-dependent are related to measurable properties, i.e., ionic conductivity of the solution, diffusion coefficient of the solute and cation (or anion) transference number [107], which are required for numerical simulation of electrochemical systems such as Li-ion batteries [100, 108-111].

Ionic conductivity is the most frequently measured property, usually using standard AC impedance methods. However, estimation of the other two parameters is rare and has been limited to a few of the most commonly used electrolytes [31-44].

Restricted diffusion theory, as extended to concentrated solutions by Newman and Chapman [112], is a powerful means for estimating the salt diffusion coefficient at a given concentration. Restricted diffusion experiments track the temporal decay of an already established concentration gradient in a cell either electrochemically (i.e., via electric potential difference between two reversible electrodes [113]) or non-electrochemically (i.e., via changes of the local refractive index of the solution [112], using UV/vis. absorption [38] or via local conductometry [114]).

The thermodynamic factor reflects solution non-ideality and must be estimated in addition to the three transport properties. Standard concentration-cell experiments are most commonly employed for this purpose which, although reliable, enable only the product of the thermodynamic factor and anion transference number to be determined [107].

Various techniques to estimate the transference number are available: Hittorf [115], moving boundary [116] and emf [117] methods directly estimate the transference number of concentrated solutions. However, each of these methods has drawbacks due to experimental complexities [112, 117]. Alternatively, the semi-infinite diffusion method has become a common practice by researchers since its development and first application to a solid polymer electrolyte by Ma et al. [31] in 1995 and further validation for liquid electrolytes by Hafezi et al. [118] in 2000. In this method, a symmetric two-electrode cell is first polarized by applying current for a short enough time that the concentration boundary layer developed at the electrode surfaces does not reach the center of the cell so that semi-infinite diffusion conditions can be assumed. The open-circuit voltage (OCV) of the cell immediately after the current is interrupted is related to the solute concentration build-up (or depletion) adjacent to the electrodes. Voltage measurements are conducted at numerous combinations of applied pulse current and duration while maintaining the semi-infinite diffusion assumption. A least-square fit of a plot of cell voltage versus $\text{current} \times \text{time}^{1/2}$ is required to obtain the transference number at a given

bulk concentration. Moreover, since double-layer discharging/charging dominates the response of each electrode at the very onset of the open-circuit step immediately after the current is interrupted, errors in the transference number obtained using this method can result if no accounting for this effect is made [31, 32, 36, 37, 39, 40, 43, 44, 118, 119].

Measurements from the semi-infinite diffusion analysis must be combined with those from the restricted diffusion and concentration-cell experiments, which are carried out using two separate setups. As a result, a large amount of experimentation conducted in three different cells is required to estimate a complete set of transport properties at a given concentration [31]. Since conventional methods assume that the transport properties do not change across the cell, the experimental conditions and the cell design must be strictly controlled to assure that only a small concentration gradient exists across the cell. However, this assumption is made only to ensure that an analytical solution to the mass transport equations exists. If the charge and mass balance equations are solved numerically, the parameters can be allowed to depend on concentration (and hence spatial location) [32, 36, 39, 40, 43, 44], which loosens the constraints on operating conditions and cell design.

A steady-state current (potentiostatic polarization) method which accounts for solution non-ideality can also be used to estimate the transference number of ions in concentrated solutions [120-122]. However, similar to the semi-infinite diffusion method, it requires prior knowledge of the solute diffusion coefficient and thermodynamic factor. Recently, nuclear magnetic resonance (NMR) spectroscopy has been used to carry out *in-situ* space- and time- resolved imaging of species concentrations which could then be used to estimate the solute diffusion coefficient and transference number [41, 42] once coupled with a mathematical model. However, MRI-based techniques require elaborate and expensive instrumentation, which is not usually available in regular electrochemistry labs.

Chapter 3

Simulation of a Commercial $LiFePO_4$ Electrode Accounting for Bulk and Surface Effects: A Comparative Analysis

The following chapter is based on previously published work by M. Farkhondeh, M. Safari, M. Pritzker, M. Fowler, T. Han, J. Wang and C. Delacourt in *J. Electrochem. Soc.* entitled:

"Full-Range Simulation of a Commercial $LiFePO_4$ Electrode Accounting for Bulk and Surface Effects: A Comparative Analysis"

This thesis author's specific contribution to this paper was to develop the model, conduct simulations, prepare all the graphics and results, prepare the manuscript and reviewer edits with direction from the project advisors who were co-authors. All authors reviewed the manuscript.

Reproduced from Ref. [100] with permission of the Electrochemical Society.

3.1 Introduction

The growing interest in LFP for use in high energy/power Li-ion batteries necessitates in-depth studies of its electrochemical performance using mathematical models. A suitable model can enhance our understanding of the governing physico-chemical phenomena and help better decipher/quantify electrode limitations eventually leading to an improved electrode design. At the same time, this model should be simple enough to serve as a handy tool for use in thermal and aging studies and prediction of full-sized commercial batteries lifetime.

LFP lithiation dynamics was first modeled by Srinivasan and Newman [57] based on the core-shell concept that describes Li insertion in a spherical LFP particle through a shrinking core of lithium-poor $Li_{\epsilon}FePO_4$ phase surrounded by a shell of lithium-rich $Li_{1-\epsilon'}FePO_4$ phase ($\epsilon \; and \; \epsilon' \ll 1$) advancing toward the center. Fick's first law with a constant diffusion coefficient is used to describe Li transport through the Li-rich shell and a lithium mass balance at the interface accounts for phase boundary movement. However, since the model is not able to account for the initial solid-solution domain, it is used to simulate the discharge process only from the moment the second phase begins to exist.

The shrinking-core model for LFP was later extended by other researchers [87, 88] to include phase-transformation kinetics which can be rate-limiting alone or in combination with lithium

diffusion. Phase transformation is driven by the departure of both interfacial concentrations from their corresponding equilibrium values, the excess free energy of interface and the energy of elastic/plastic deformation at the interface. Although enlightening, these considerations introduce a number of new parameters that must be estimated and lead to a model that is more sophisticated but is still based on a non-realistic physical picture of the mechanism of Li insertion. Moreover, porous-electrode effects are ignored in these models which introduce errors, particularly when analyzing discharge at high rates (20C).

More recently, Dargaville and Farrell [89] developed a multi-scale continuum model for an LFP electrode featuring an intermediate secondary-particle or agglomerate scale (i.e., additional to the primary particle and electrode scales) which had not been previously included. The original core-shell model of Srinivasan of Newman [57] is implemented to describe the lithiation dynamics at the smallest scale and porous-electrode theory of Newman [123] is used to describe the phenomena operating at both the agglomerate and electrode scales. However, the introduction of this new intermediate scale doubles the number of model parameters which are not easily determined by direct or indirect measurements.

All of these aforementioned core-shell models have been applied to describe the electrode performance under galvanostatic discharge mode only. Difficulties arise if a multi-pulse cycling operation is to be simulated where tracking of the movement of the two-phase boundary requires a great deal of numerical computation.

As an alternative to the classical Stefan moving-boundary problem, Han et al. [90] applied phase-field theory based on the Cahn-Hilliard formulation as an approach to describe lithiation dynamics of two-phase intercalation materials. Singh et al. [91] showed that in the so-called surface-reaction-limited regime, a Cahn-Hilliard-based phase-field model is able to predict the wave-like propagation of the phase-transformation front in the direction perpendicular to that of lithium diffusion (i.e., the *b*-axis in *Pnma* space group), in line with some experimental observations [67, 68, 124].

The poor electronic conductivity of LFP and the effect of non-uniform carbon coatings were addressed in the so-called resistive-reactant (RR) model initially proposed by Thomas [92]. According to this model, a distributed ohmic drop at the particle surface was incorporated into the core-shell model of Srinivasan and Newman. The model was able to capture the sloping behavior observed in experimental 5C galvanostatic discharge curves commonly attributed to porous-electrode

effects across the cell in regular porous-electrode models. Thorat et al. [102, 125] included a set of two inter-particle contact resistances in their model to fit the experimental data. Using the same concept, Safari and Delacourt [59] developed a simple multi-particle RR model consisting of a four-bin contact-resistance distribution that was refined by fitting low-rate galvanostatic charge/discharge data. This approach yielded promising results and was able to simulate the cycle-path dependence of the electrode experimentally observed for LFP. However, this model does not include porous-electrode effects and is not valid under large current operation.

In 2009, Thorat [125] proposed a solid-solution model for LFP with a concentration-dependent solid-state diffusion coefficient referred to as phase-change diffusivity. The aim was to include the $FePO_4/LiFePO_4$ phase transformation in the model without having to track the displacement of the two-phase front. However, the author concluded that the phase-change diffusivity overpredicted the solid-phase mass-transfer resistance and so ultimately resorted to Fickian diffusion with a constant solid-state diffusivity to simulate battery performance. Recently, Farkhondeh and Delacourt [16] developed the variable solid-state diffusivity (VSSD) model based on the approach proposed by Thorat [102, 125] to simulate galvanostatic charge and discharge processes of 3 commercial LFP electrodes with different designs (e.g., particle size and active material loading). A similar approach has been applied to other insertion materials (e.g., graphite, $LiCoO_2$, $LiFeSO_4F$) in the past [126-131]. The variable diffusivity was derived from the corresponding equilibrium potential of each electrode. Porous-electrode effects were ignored. Promising results were obtained for all the samples although experimental validation was limited to low C-rates only (1C or less). On the basis of a comparison of the model parameters for the three samples, the authors concluded that resistive-reactant effects also contribute to the performance of LFP electrodes composed of nanoparticles [16, 59].

Among the lithiation/delithiation models proposed for LFP in the literature, the VSSD and RR models appear to be the simplest, yet remain physically significant. Bulk transport limitations are assumed to exist and lumped into a concentration-dependent diffusion coefficient in the VSSD model and surface effects are represented by a set of contact resistances in the RR model, avoiding explicit inclusion of the microstructural details of LFP which is still a matter of debate among researchers. The objective of this chapter is to perform a comparative analysis of these two models to clarify ambiguities associated with the dynamics of Li insertion into LFP particles and identify/decipher rate limitations of a specific LFP electrode. Special attention is paid to expand the two models in order to

comply with high C-rate conditions which involve a larger number of adjustable parameters and require improved methods for parameter estimation. Both the comparison of the two models and the juxtaposition of the low-rate and high-rate simulations help highlight the effect of the low electronic conductivity of LFP and the presumed sluggish lithium transport within LFP on its performance as an electrode.

3.2 Model Development

To simulate the electrochemical performance of an LFP electrode, the variable solid-state diffusivity [16] and resistive-reactant models [59] are implemented to describe the lithiation/delithiation dynamics at the particle level. These two specific models are chosen to investigate both intra-particle transport limitations (i.e., bulk effects using the VSSD model) and electronic losses (i.e., surface effects using the RR model) of LFP in a comparative manner. Moreover, these models are relatively easy to implement and simple to interpret [57, 87-91].

The half-cell assembly is made of a porous LFP electrode as the working electrode, elemental lithium as the counter/reference electrode and a porous separator soaked with an electrolyte positioned between the two. In order to make high-rate charge/discharge simulations possible, the two models are separately incorporated into Newman's porous-electrode theory [108, 123] to describe electrode-level transport phenomena, as done by Doyle et al. [108] in developing their pseudo-2-dimensional (P2D) battery model. Both the VSSD and RR models are applied to a small coin cell for which a 1-D analysis at the electrode level (i.e., along the cell thickness) suffices. Concentrated-solution theory describes the transport of ions in the electrolyte [107]. Charging/discharging of the double-layer capacitance is not significant in the case of long galvanostatic charges/discharges and so is neglected in the current model. The concept of porous-electrode theory, concentrated-solution theory, assumptions and complete derivations are thoroughly discussed elsewhere [107, 123, 132] and so are not described in detail here for conciseness. In a two-electrode half-cell configuration where a lithium foil serves simultaneously as the counter electrode and reference electrode, it is necessary to correct for the surface overpotential especially at large current density. For this purpose, Butler-Volmer equation is used to relate the rate of the lithium deposition/stripping reaction to the counter electrode surface overpotential [16, 59]. The governing equations and corresponding boundary conditions used in both the VSSD and RR models of the Li/LFP half-cell are listed in Table 3-1. The VSSD and RR models presented here are extensions of previous versions since they account for porous-electrode effects and are valid for both low and high C-rates (see Refs. [59] and [16]). They

will be used to carry out simulations under both low-rate and high-rate conditions (hereafter referred to as "full-range") that are compared to experimental galvanostatic discharge data in "Results and Discussion".

3.2.1 Variable Solid-State Diffusivity Model

As mentioned before, the VSSD model focuses on the effect of slow lithium transport in the bulk of LFP without including a detailed micro-scale intercalation mechanism. The active material is envisaged to be a non-ideal binary solution of empty sites (S) and Li-intercalated sites (LiS) and the driving force for diffusion of a species is the gradient of its chemical potential [16]. In this model, the LFP electrode is assumed to be made up of a few groups of spherical particles with different sizes to account for possible effects of the distribution of particle sizes of active material (PSD).

At constant temperature, pressure and volume, the flux density of LiS ($N_{\mathrm{LiS},k}$) according to concentrated-solution theory is written as [16, 107]

$$N_{\mathrm{LiS},k} = -c_{\max}\alpha_{\mathrm{LiS},k}\mathcal{D}_{\mathrm{LiS}}\frac{\partial y_k}{\partial r} \tag{3-1}$$

where $c_{\max}$ is the maximum (saturation) concentration of LiS equal to the lithium concentration in fully lithiated LFP, $\mathcal{D}_{\mathrm{LiS}}$ is the binary diffusion coefficient, $y_k(r,t)$ is the mole fraction of LiS in the k^{th} particle group and r is the radial distance from the particle center. $\alpha_{\mathrm{LiS},k}$ is called the thermodynamic factor and is evaluated as follows from the equilibrium potential of the electrode [16, 129]:

$$\alpha_{\mathrm{LiS},k} = -\frac{F}{RT}y_k(1-y_k)\frac{\partial U_k}{\partial y_k}. \tag{3-2}$$

U_k is the equilibrium potential of the k^{th} particle group that depends on the LiS concentration and is determined experimentally, F is the Faraday constant, R is the gas constant and T is temperature.

The Butler-Volmer equation is used to describe the charge-transfer reaction kinetics on the surface of each particle group:

$$i_{\mathrm{n},k} = i_k^0\left[\exp\left(\frac{(1-\beta_{\mathrm{LFP}})F}{RT}\eta_k\right) - \exp\left(\frac{-\beta_{\mathrm{LFP}}F}{RT}\eta_k\right)\right]. \tag{3-3}$$

$i_{\mathrm{n},k}$ represents the current density normal to the active surface of the k^{th} particle group and is positive for electrode delithiation (charge) and negative for electrode lithiation (discharge). β_{LFP} is the charge-transfer coefficient (same for all particle groups), i_k^0 is the exchange current density and η_k is the surface overpotential for the k^{th} particle group. The exchange current density corresponding to the k^{th} particle group i_k^0 is given by the following expression:

$$i_k^0 = Fk_{\mathrm{LFP}}^0 c^{1-\beta_{\mathrm{LFP}}} c_{\max} \left(1 - y_{\mathrm{s},k}\right)^{1-\beta_{\mathrm{LFP}}} {y_{\mathrm{s},k}}^{\beta_{\mathrm{LFP}}}, \tag{3-4}$$

with k_{LFP}^0 being a rate constant (same for all particle groups), c the salt concentration in the electrolyte adjacent to the particle surface and $y_{\mathrm{s},k}$ the mole fraction of LiS at the surface of the k^{th} particle group. This treatment is valid for an ideal electrode and electrolyte. The effect of non-idealities can be included by replacing concentrations with the corresponding activities. The complete derivation of such a thermodynamically-consistent kinetic equation is found in Ref. [129]. In the current model, however, the exchange current density is taken to depend only on the electrolyte concentration as follows:

$$i^0 = Fk_{\mathrm{LFP}}^0 c_{\max} c^{1-\beta_{\mathrm{LFP}}}. \tag{3-5}$$

The exchange current density will be constant during charge/discharge at low rates where the spatial variation of electrolyte concentration is negligible [16]. Assuming perfect electronic connection between active-material particles and the adjacent conductive matrix, the surface overpotential is written as

$$\eta_k = \Phi_1 - \Phi_2 - U_{\mathrm{s},k}, \tag{3-6}$$

where Φ_1 is the potential of the solid phase, Φ_2 is the liquid-phase potential and $U_{\mathrm{s},k}$ is the equilibrium potential at the surface of particles in the k^{th} group and depends on the LiS concentration. A detailed derivation of model equations for the VSSD model can be found in Ref. [16].

3.2.2 Resistive-Reactant Model

The undesirable insulating property of LFP is in practice partially overcome by applying a carbon coating to the particle surface. The conductivity improvement has been shown to depend not only on the amount of carbon applied but also on the quality of the coating (e.g., chemical nature and uniformity) and on the distribution of conductive filler particles (e.g., acetylene black) surrounding the active material [59, 92, 133, 134]. The RR model developed here highlights the non-uniform

distribution of the conductive filler around LFP particles. For this purpose, we adopt the multi-particle RR model of Safari et al. [59] in which the contact resistance between an active particle and the conductive matrix impedes Li insertion/de-insertion at the particle surface. The active material particles are considered to be spherical with a uniform size (i.e., no particle size distribution is considered in contrast to the VSSD model) but with varying electronic connectivities to the conductive matrix. The surface overpotential used in the kinetic equation (i.e., Butler-Volmer, Eq. (3-3)) is modified to account for this difference in electronic connectivity:

$$\eta_k = \Phi_{1,k} - \Phi_2 - U_{\mathrm{s},k}, \tag{3-7}$$

where $\Phi_{1,k}$ is the solid-phase potential at the surface of an LFP particle in particle group k which differs from the potential Φ_1 of the surrounding cathode conductive matrix. In this model, particle groups are distinguished on the basis of the inter-particle contact resistance $R_{\mathrm{c},k}$. The difference between Φ_1 and $\Phi_{1,k}$ corresponds to the ohmic polarization between the conductive matrix and the active particle induced by the contact resistance [59, 92, 125], i.e.,

$$\Phi_{1,k} = \Phi_1 - R_{\mathrm{c},k} i_{\mathrm{n},k}. \tag{3-8}$$

Contrary to the VSSD model, the resistive-reactant model assumes that an ideal solid solution governs the bulk behavior of the material. As a result, the solid-state thermodynamic factor $\alpha_{\mathrm{LiS},k}$ is set to 1 and Fick's law with a constant diffusion coefficient is applied to describe the diffusion of LiS species inside LFP particles:

$$N_{\mathrm{LiS},k} = -\mathcal{D}_{\mathrm{LiS}} c_{\max} \frac{\partial y_k}{\partial r}. \tag{3-9}$$

The reader is referred to Ref. [59] for a detailed description of the multi-particle resistive-reactant model.

Table 3-1. Summary of governing equations and corresponding boundary conditions used for Li/LFP half-cell simulations.

Governing equations for particle-level phenomena

Variable solid-state diffusivity model	Resistive-reactant model
$c_{\max} \frac{\partial y_k}{\partial t} = -\frac{1}{r^2} \frac{\partial}{\partial r}\left(r^2 N_{\mathrm{LiS},k}\right)$	$c_{\max} \frac{\partial y_k}{\partial t} = -\frac{1}{r^2} \frac{\partial}{\partial r}\left(r^2 N_{\mathrm{LiS},k}\right)$

$\left(\text{B.C.}: \quad N_{\text{LiS},k}\big|_{r=0} = 0 \text{ and } N_{\text{LiS},k}\big|_{r=R_{\text{p},k}} = \frac{i_{\text{n},k}}{F}\right)$ $\left(\text{B.C.}: \quad N_{\text{LiS},k}\big|_{r=0} = 0 \text{ and } N_{\text{LiS},k}\big|_{r=R_{\text{p},k}} = \frac{i_{\text{n},k}}{F}\right)$

$N_{\text{LiS},k} = -\alpha_{\text{LiS},k}\mathcal{D}_{\text{LiS}}c_{\max}\frac{\partial y_k}{\partial r}$ $N_{\text{LiS},k} = -\mathcal{D}_{\text{LiS}}c_{\max}\frac{\partial y_k}{\partial r}$

$\alpha_{\text{LiS},k} = -\frac{F}{RT}y_k(1-y_k)\frac{\partial U_k}{\partial y_k}$ $i_{\text{n},k} = i^0\left[\exp\left(\frac{(1-\beta_{\text{LFP}})F}{RT}\eta_k\right) - \exp\left(\frac{-\beta_{\text{LFP}}F}{RT}\eta_k\right)\right]$

$i_{\text{n},k} = i^0\left[\exp\left(\frac{(1-\beta_{\text{LFP}})F}{RT}\eta_k\right) - \exp\left(\frac{-\beta_{\text{LFP}}F}{RT}\eta_k\right)\right]$ $\eta_k = \Phi_1 - \Phi_2 - R_{\text{c},k}i_{\text{n},k} - U_{\text{s},k}$

$\eta_k = \Phi_1 - \Phi_2 - U_{\text{s},k}$

Governing equations for electrode-level phenomena

Cathode equations	Boundary conditions
$\nabla\cdot\mathbf{i}_2 = \sum a_k i_{\text{n},k}$	continuity at $x = l_{\text{sep}}$ and $\mathbf{i}_{2,x}\big\|_{x=l_{\text{sep}}+l_{\text{cat}}} = 0$
$a_k = \frac{3}{R_{\text{c},k}}\varepsilon_k\varepsilon_t$	
$\mathbf{i}_2 = -\kappa_{\text{eff,cat}}\left(\nabla\Phi_2 - \frac{2RT(1-t_+^0)}{F}\left(1+\frac{\partial\ln f_\pm}{\partial\ln c}\right)\nabla\ln c\right)$	
$\kappa_{\text{eff,cat}} = \kappa\varepsilon_{\text{cat}}^{\gamma}$	
$\nabla\cdot\mathbf{i}_1 = -\sum a_k i_{\text{n},k}$	$\mathbf{i}_{1,x}\big\|_{x=l_{\text{sep}}} = 0$ and $\mathbf{i}_{1,x}\big\|_{x=l_{\text{sep}}+l_{\text{cat}}} = I$
$\mathbf{i}_1 = -\sigma_{\text{eff}}\nabla\Phi_1$	
$\sigma_{\text{eff}} = \sigma(1-\varepsilon_{\text{cat}})^{\gamma}$	
$\varepsilon_{\text{cat}}\frac{\partial c}{\partial t} = \nabla\cdot\left(\varepsilon_{\text{cat}}D_{\text{eff,cat}}\nabla c\right)$ $-\frac{\mathbf{i}_2\cdot\nabla t_+^0}{F} + \frac{(1-t_+^0)}{F}\sum a_k i_{\text{n},k}$	continuity at $x = l_{\text{sep}}$ and $\nabla c\big\|_{x=l_{\text{sep}}+l_{\text{cat}}} = 0$
$D_{\text{eff,cat}} = D\varepsilon_{\text{cat}}^{\gamma\text{-}1}$	
$D = \frac{c_{\text{T}}}{c_0}\left(1+\frac{\partial\ln f_\pm}{\partial\ln c}\right)\mathcal{D}$	
Separator equations	**Boundary conditions**
$\nabla\cdot\mathbf{i}_2 = 0$	$\Phi_2\big\|_{x=0} = 0$ and continuity at $x = l_{\text{sep}}$
$\mathbf{i}_2 = -\kappa_{\text{eff,sep}}\left(\nabla\Phi_2 - \frac{2RT(1-t_+^0)}{F}\left(1+\frac{\partial\ln f_\pm}{\partial\ln c}\right)\nabla\ln c\right)$	
$\kappa_{\text{eff,sep}} = \kappa\varepsilon_{\text{sep}}^{\gamma}$	

$$\varepsilon_{\text{sep}} \frac{\partial c}{\partial t} = \nabla \cdot \left(\varepsilon_{\text{sep}} D_{\text{eff,sep}} \nabla c\right) - \frac{\mathbf{i}_2 \cdot \nabla t_+^0}{F} \qquad \varepsilon_{\text{sep}} \nabla c\big|_{x=0} = -\frac{I(1-t_+^0)}{F D_{\text{eff,sep}}} \text{ and continuity at } x = l_{\text{sep}}$$

$$D_{\text{eff,sep}} = D\varepsilon_{\text{sep}}^{\gamma\text{-}1}$$

$$D = \frac{c_{\text{T}}}{c_0}\left(1 + \frac{\partial \ln f_{\pm}}{\partial \ln c}\right)\mathcal{D}$$

Li foil counter electrode

$$I = i_{\text{Li}}^0 \left(\frac{c}{c_{\text{ini}}}\right)^{1-\beta_{\text{Li}}} \left[\exp\left(\frac{(1-\beta_{\text{Li}})F}{RT}(\Phi_{\text{Li}} - \Phi_2)\right) - \exp\left(\frac{-\beta_{\text{Li}}F}{RT}(\Phi_{\text{Li}} - \Phi_2)\right)\right]$$

Equilibrium potential functions

C/50 charge:
$$U_k = 3.451 - 8.8\times10^{-3}(1-y_k) + 0.668\exp(-81.002(1-y_k)^{1.18}) + 2.374\times10^{-9}\exp(25.22(1-y_k)^{3.48}) - 2.637\times10^{-9}\exp(25.12(1-y_k)^{3.49})$$

C/50 discharge:
$$U_k = 3.428 - 2.027\times10^{-2} y_k + 0.509\exp(-81.16 y_k^{1.01}) + 7.644\times10^{-8}\exp(25.361 y_k^{3.30}) - 8.4410\times10^{-8}\exp(25.262 y_k^{3.31})$$

3.2.3 Solution Procedure

The system of the time-dependent governing equations for both models (Table 3-1) is numerically solved by means of the finite-element-based COMSOL Multiphysics simulation package. The dimensionless electrode and separator thicknesses are each discretized into 10 equal elements. The mesh in the interior of an LFP particle in the radial direction consists of 20 elements that shrink in size as its surface is approached with the smallest element being 0.2 times the largest one. The solver is supervised in MATLAB using COMSOL LiveLink™ for MATLAB.

3.3 Results and Discussion

The models are used to analyze experimental galvanostatic discharge data over a wide range of rates from C/25 to 5C (defined as full range) obtained from a previous study of a commercial LFP electrode (see Ref. [16]; high-rate data were not reported nor analyzed in this previous study). Aside from a hysteresis in potential between low-rate charge and discharge, the models predict virtually identical responses during charging and discharging and therefore only simulations of the discharge mode are presented in this analysis.

The LFP electrode was cycled between 2.5 V (lower cut-off potential) and 4.1 V (upper cut-off potential) versus lithium in a CR2032-type coin-cell setup ($A_{\mathrm{geom}} = 1.202\ \mathrm{cm}^2$) at 25˚C. Whatman GF/D borosilicate glass fiber was soaked in a solution containing 1M $LiPF_6$ in EC/DMC (1:1 wt) to form the electrolytic medium between the electrodes in the coin cell. No measurement of the true *in-situ* thickness of the separator during cell operation is available and so its dry, uncompressed thickness taken from the product specification sheet is used in the simulations. Reasonable values are assumed for the electrode and separator porosities. The thorough description of the procedure for sample preparation and experiments can be found in an earlier reference [16]. Reasonably low-rate galvanostatic charge and discharge profiles are commonly averaged to yield a single set of equilibrium potentials as a function of lithium content in the active material. In the case of LFP, a zero-current hysteresis exists between charge and discharge potentials [14, 16, 135] that is not accounted for in most continuum models in the literature. As in Ref. [16], C/50 charge and discharge curves are used separately to determine the equilibrium potentials during charging and discharging and so the need to predict the thermodynamic hysteresis is avoided. The origin of this potential hysteresis has not been firmly identified and its inclusion is beyond the scope of this research. The empirical expressions relating the equilibrium potential to the lithium concentration y_k obtained in this way during charging and discharging are listed at the bottom of Table 3-1.

The parameter values for both particle-level and electrode-level properties are listed in Table 3-2. Values marked as "taken from literature" are extracted from Ref. [16] except for the cation transference number, the separator thickness and the effective electrode conductivity that are found in Refs. [136], [137] and [138], respectively. Since only small discrepancies exist among the reported estimates of the cation transference number [37], it is fairly reasonable to take a constant value for this parameter from the literature. The initial conditions are a uniform Li concentration in all particle groups in the fully charged state and $c_{\mathrm{ini}} = 1000\ \mathrm{mol\ m^{-3}}$.

Table 3-2. List of parameters used in both VSSD and RR models at 25°C.

Parameter	Symbol	VSSD model	RR model
Electrode thickness (μm)	l_{cat}	80[1]	80[1]
Separator thickness (μm)	l_{sep}	675[1]	675[1]
Electrode porosity	$\varepsilon_{\mathrm{cat}}$	0.5[a]	0.5[a]

Separator porosity	ε_{sep}	0.6[a]	0.6[a]
Median active-particle diameter (nm)	d_{50}	72[l]	72[l]
Total active-material volume fraction	ε_t	0.351[l]	0.351[l]
Maximum solid-phase lithium concentration (mol m^{-3})	c_{max}	22,806[a]	22,806[a]
Solid-state binary diffusion coefficient ($m^2 s^{-1}$)	$\mathcal{D}_{LiS}$	5×10^{-19}[l]	7×10^{-19}[f]
Solid-state thermodynamic factor	$\alpha_{LiS,k}$	Figure 3-1a[l]	1.0[a]
Cathode equilibrium potential (V vs. Li)	U_k	Table 3-1[l]	Table 3-1[l]
Particle radius (nm)	$R_{p,k}$	Table 3-3[f]	36[l]
Contact resistance (Ω m^2)	$R_{c,k}$	NA	Figure 3-10[f]
Active particle volume fraction	ε_k	Table 3-3[f]	Figure 3-10[f]
Cathode charge-transfer coefficient	β_{LFP}	0.5[a]	0.5[a]
Li foil charge-transfer coefficient	β_{Li}	0.5[a]	0.5[a]
Reaction rate constant (mol m^{-2} s^{-1} $(mol\ m^{-3})^{-1.5}$)	k^0_{LFP}	2.5×10^{-13}[f]	2.5×10^{-13}[f]
Effective Li foil exchange current density referred to 1 M electrolyte concentration (A m^{-2})	i^0_{Li}	19[l]	19[l]
Initial salt concentration in the solution (mol m^{-3})	c_{ini}	1000[l]	1000[l]
Bulk diffusion coefficient of the electrolyte ($m^2 s^{-1}$)	D	5.2×10^{-10}[f]	5.2×10^{-10}[f]
Li^+ transference number	t^0_+	0.363[l]	0.363[l]
Bulk ionic conductivity of the electrolyte (S m^{-1})	κ	1.3[f]	1.3[f]
Effective electronic conductivity of the cathode (S m^{-1})	σ_{eff}	6.75[l]	6.75[l]
Bruggeman exponent	γ	1.5[a]	1.5[a]

[l]: Taken from literature; [a]: Assumed; [f]: Fitted to the experimental data

3.3.1 Variable Solid-State Diffusivity Model

The thermodynamic factor $\alpha_{\mathrm{LiS},k}$ used in the VSSD model is determined using a procedure reported previously [16] that involves averaging the values calculated from Eq. (3-2) for equilibrium potentials corresponding to C/50 charge and C/50 discharge experimental data, as shown in Figure 3-1a. If the binary solution of LiS and S were ideal, the equilibrium potential would be Nernstian and the thermodynamic factor equal to 1. As shown in Figure 3-1b, the magnitude of the resulting Fickian diffusion coefficient $D_{\mathrm{LiS},k}$ ($D_{\mathrm{LiS},k} = \mathcal{D}_{\mathrm{LiS}}\alpha_{\mathrm{LiS},k}$) deviates significantly from the ideal situation, especially in the intermediate stoichiometry range where $\alpha_{\mathrm{LiS},k} \ll 1$, but also in the regions at low and high y_k bounded by the two peaks where $\alpha_{\mathrm{LiS},k}$ >1. These two peaks roughly coincide with the solid-solution composition ranges (i.e., $y < \epsilon$ and $y > 1 - \epsilon'$). On the basis of the non-ideal binary solution assumption, steep changes of the thermodynamic factor with stoichiometry can be interpreted as being due to i) repulsive interactions between inserted lithium ions at $y < \epsilon$ and $y > 1 - \epsilon'$ where LFP behaves as a solid solution [56, 57] and ii) the dominance of strong attractive forces between the guest cations over the miscibility gap $\epsilon < y < 1 - \epsilon'$.

The parameters discussed so far have been determined either experimentally or assumed. The reaction rate constant k^0_{LFP} and particle-size distribution at the particle scale, electrolyte diffusivity D and ionic conductivity κ at the electrode scale are treated as adjustable parameters estimated by manually fitting the computed galvanostatic curves to the experimental data. The solid-state binary diffusivity $\mathcal{D}_{\mathrm{LiS}}$ was treated as an adjustable parameter in Ref. [16] obtained by fitting the model to experimental data corresponding to low-rate conditions. For the sake of consistency of the analysis, the best-fit value ($\mathcal{D}_{\mathrm{LiS}} = 5\times10^{-19}$ m^2 s^{-1}) obtained in that study is used here for the full-range galvanostatic discharge simulations.

Three distinct features that generally appear in galvanostatic potential-capacity curves (see Figure 3-2 as an example) help reduce uncertainties in parameter estimation: i) kinetic overpotential distinguishable at early stages of low-rate discharge, ii) gradual variation of electrode potential at intermediate states of discharge signifying potential loss in addition to kinetic overpotential and iii) sharp rise in potential loss close to the lower/upper cutoff potentials at the end-of-discharge/charge (end-of-discharge capacities) [57].

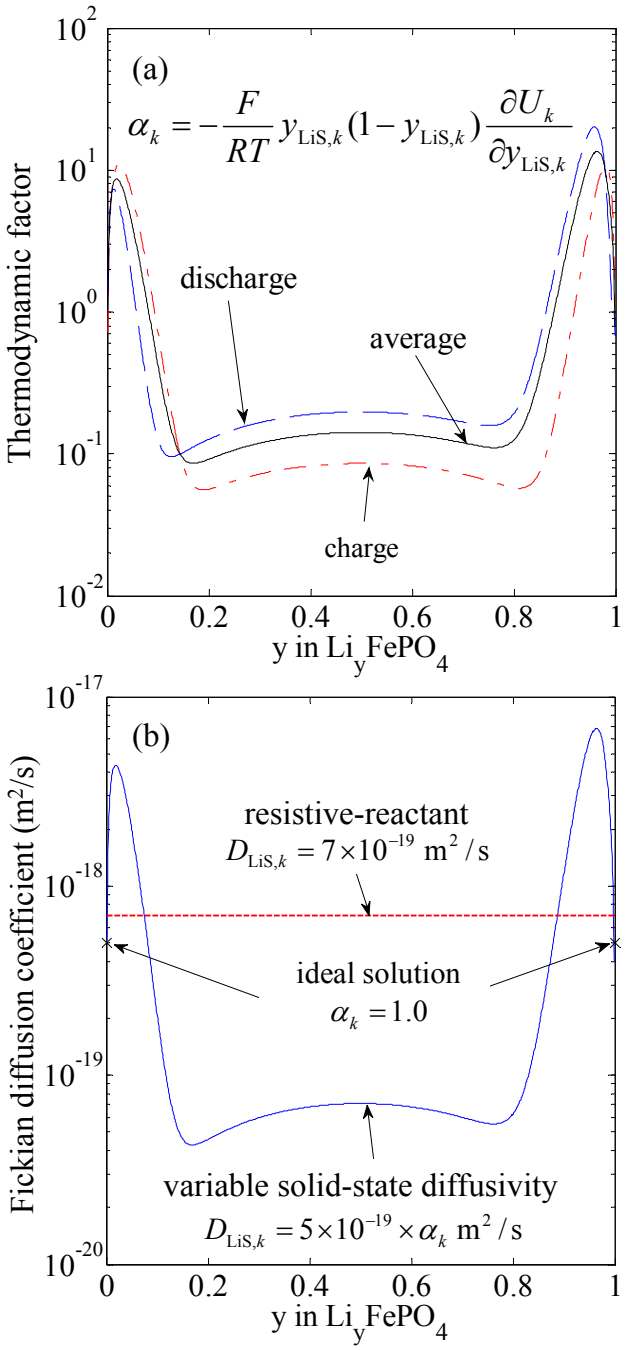

Figure 3-1. (a) Solid-state thermodynamic factor $\alpha_{\mathrm{LiS},k}$ derived from the experimental equilibrium potential and (b) Fickian diffusion coefficients of Li species within an LFP particle used in the VSSD (blue solid line) and RR (red dashed line) models.

To fit the model over the full range of experimental data, the conditions are divided into low-discharge-rate (up to 1C) and high-discharge-rate (from 1C to 5C) domains. Given that electrode-level potential losses are smallest at low applied currents [16, 59, 75, 139, 140], the reaction rate constant k^0_{LFP} can be estimated by fitting the experimental electrode potential at the onset of the potential plateau in the potential-capacity curves (i.e., the first characteristic feature) simultaneously for discharge rates from C/25 up to 1C, while D and κ are kept at arbitrary values since they have no significant impact on the model predictions under these conditions. D and κ can then be adjusted to capture the augmented potential losses that occur at higher rates from 1C to 5C. For simplicity, transport properties of the electrolyte are assumed to be independent of concentration and the electrolyte thermodynamic factor is set to 1. The model parameter values are compiled in Table 3-2.

The second characteristic feature of the potential-capacity curves (sloping potential) is commonly attributed to the displacement of the lithiation front along the electrode thickness from the least resistant (i.e., minimum electrode-level loss) position at the onset to the most resistant (i.e., maximum electrode-level loss) one at the end of discharge. Finally, end-capacities (i.e., the third characteristic feature) are usually ascribed to mass-transport limitations inside the active material.

The Butler-Volmer equation used to describe the insertion of Li^+ into regular active materials typically includes both the electrolyte concentration and the surface concentration of the intercalated lithium LiS (Eqs. (3-3) and (3-4)). However, incorporation of the latter concentration in the kinetic equation turns out to under-predict the electrode potential at the very beginning of the LFP lithiation process (not shown here). Therefore, the LFP lithiation kinetics is taken to be independent of the solid-phase surface concentration in this study (Eqs. (3-3) and (3-5)) [16].

Although the electrolyte transport properties are within the range reported in the literature [37-39, 102], they are not most accurately refined due to the model assumptions and require independent ex-situ measurements for best results. The fitted values, however, are satisfactory for the purposes of this study. The sensitivity of the model to the electrolyte transport properties and electronic conductivity of the electrode has been investigated by varying one parameter at a time while holding the others at their values in Table 3-2. The resulting potential versus capacity curves are plotted in Figure 3-2. Over the range considered, the electrode-level parameter values have no significant effect in the case of the low-rate (C/2) discharge curve unlike the case of the 5C curves, implying that porous-electrode effects are minimal in agreement with the literature [16, 59, 75, 139, 140] and that the value of the reaction rate constant obtained from low-rate simulations is a reliable

estimate. Although porous-electrode effects are included in the simulations, the best-refined rate constant of 2.5×10^{-13} mol m^{-2}s^{-1} (mol m^{-3})$^{-1.5}$ is in a good agreement with those obtained for 3 different LFP electrodes in our previous study (6.75×10^{-14} to 2.38×10^{-13} mol m^{-2}s^{-1} (mol m^{-3})$^{-1.5}$) [16]. The approach of dividing the operating conditions into low-rate and high-rate regimes helps to unravel the origin of the potential losses (i.e., kinetics of charge-transfer reaction at the particle-level versus electrode-level limitations) and enables the simulation of accurate galvanostatic discharges at rates ranging from as low as C/25 up to 5C (i.e., ratio of 125).

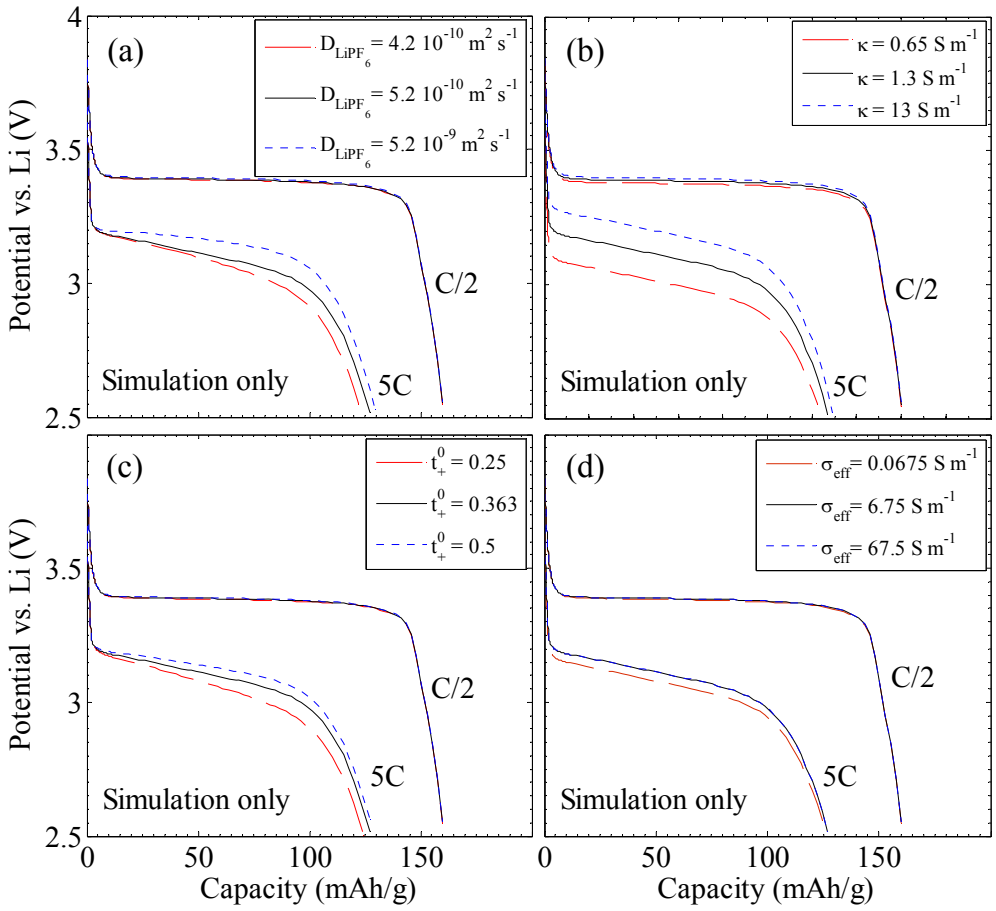

Figure 3-2. VSSD model sensitivity to (a) D, (b) κ, (c) t_+^0 and (d) σ_{eff} at discharge rates of C/2 and 5C and 25°C. Model parameters are given in Table 3-2 and Table 3-3 except for those varied (see legend).

The impact of the particle-size distribution on the overall electrode performance can be analyzed using the VSSD model. Although various methods were examined in Ref. [16] to discretize

the actual PSD from SEM image analysis into 4 bins, the results were unsatisfactory. Ultimately three particle bins were adjusted in order for the simulations to match the low-rate charge/discharge data (i.e., 1C or less). The d_{50} size obtained from the actual PSD was taken as a fixed particle size (i.e., not adjustable) while the other 2 particle sizes and corresponding volume fractions were treated as adjustable parameters. This set of particle bins was used in the present analysis for the full-range simulations, but was found to under-predict the end-of-discharge capacities at rates higher than 1C. However, by including a fourth particle size (44 nm) in this PSD and re-adjusting the volume fractions, the model was successfully fitted to the experimental discharge data at all rates from C/25 up to 5C, as shown in Figure 3-3a.

The refined particle sizes and the corresponding volume- and number-based fractions are listed in Table 3-3. It is worth mentioning that this fitted PSD lies within the range of the actual particle sizes obtained from SEM micrographs [16]. Nonetheless, the transformation of volume-based fractions to number-based fractions reveals the sensitivity of the model to the number-based PSD. For instance, the presence of 5 large particles in a total number of 10,000 can significantly influence the outcome of a simulation. Thus, particle number-based techniques such as SEM image analysis may not give reliable estimates of the real size distribution of active particles in a composite electrode although they are widely used to determine d_{50}.

Table 3-3. Particle-size distribution obtained by fitting the VSSD model to experimental isothermal (T = 25°C) galvanostatic discharge curves at different C-rates ranging from C/25 to 5C.

Particle group	Size, $2R_{\mathrm{p},k}$ (nm)	Volume fraction, ε_k	Number fraction
1	44	0.36	0.7802
2	72	0.42	0.2077
3	124	0.12	0.0116
4	338	0.10	0.0005

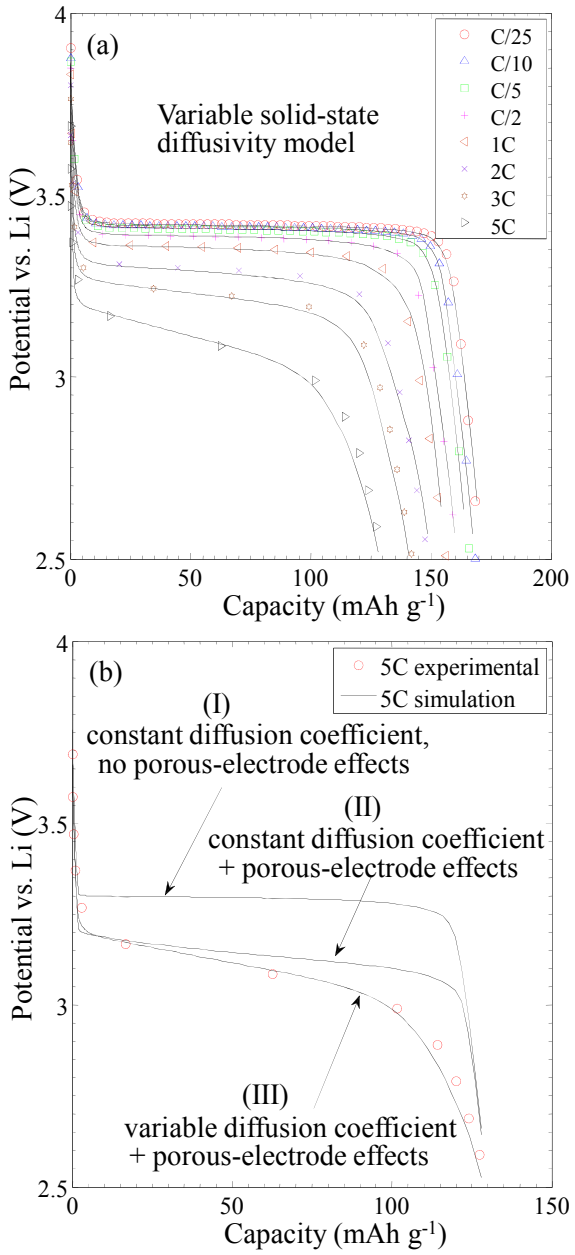

Figure 3-3. (a) Comparison of experimental (symbols) and VSSD model-fitted (solid lines) galvanostatic discharge data at 25°C. (b) Components contributing to the overall potential drop at 5C; the constant-diffusivity ($\alpha_{\mathrm{LiS},k} = 1.0$) simulations are scaled slightly to the experimental end-of-discharge capacity (i.e., from ca. 120 mAh g^{-1} to 128 mAh g^{-1}) for better demonstration. Model parameters are listed in Table 3-2 and Table 3-3.

The 4-bin PSD obtained by fitting to the full range of C-rates is compared with the 3-bin PSD fitted to the low-rate charge/discharge data [16] in Figure 3-4. A shift in particle-size distribution is evident in Figure 3-4b with 44 nm rather than 72 nm constituting the largest number-based fraction in the 4-bin PSD. The actual electrode performs better than predicted by the 3-bin-based model at high applied currents and so a smaller particle is needed in addition to those in the 3-bin PSD previously fitted on the basis of low-rate data [16]. The variation of the fitted values for the PSD at different applied currents is unexpected since particle size is a geometric parameter and should remain invariable. Such an apparent dependence of the fitted particle size on C-rate may arise from the fact that phenomena such as the LFP lithiation mechanism being potential (or C-rate) dependent are not considered in the model. Based on a phase-field model, Tang et al. [97] suggested the existence of a critical particle size below which LFP lithiation may change from a crystalline-to-crystalline pathway (i.e., conventional picture) to various crystalline-to-amorphous pathways depending on the energy barriers of the competing transformation routes. In a recent phase-field study, Bai and co-workers [94] proposed that phase change in a single LFP crystal is suppressed in favor of a facile single-phase lithiation mechanism under an augmented applied current. No firm experimental evidence has yet been reported in the literature. Using a simple single-particle model, Delacourt et al. [141] were able to simulate the onset of charge/discharge data of an LFP electrode with particle size as a unique adjustable parameter which decreases when the applied current increases. They interpreted the apparent rate dependence of particle size by invoking the mosaic model, originally proposed by Andersson et al. [142] to explain the capacity loss of LFP electrode in the first few cycles.

The role that the concentration-dependent solid-state diffusion coefficient and the porous-electrode effects have on the potential losses of an LFP electrode undergoing 5C discharge is examined by breaking down the potential-capacity curve into different components in Figure 3-3b. Several observations can be made concerning this breakdown: i) the potential loss is considerably under-predicted when a constant diffusion coefficient is used and no porous-electrode effects are included, ii) the electrode potential drops visibly by taking into account the porous-electrode effects and iii) inclusion of the experimentally-obtained thermodynamic factor $\alpha_{\mathrm{LiS},k}$ in the model to account for variable solid-state diffusivity (i.e., $D_{\mathrm{LiS},k} = \mathcal{D}_{\mathrm{LiS}}\alpha_{\mathrm{LiS},k}$) significantly improves the model so that it closely matches the experimental data over the entire curve. In the VSSD model, the depressed values of the thermodynamic factor in the intermediate composition range can be interpreted as being due to the strong attractive forces between intercalated ions inside LFP which decrease their mobility in the miscibility-gap range. In fact, the abrupt change in diffusion coefficient from $\sim 10^{-18}$ $\mathrm{m^2\ s^{-1}}$ at

$y < \epsilon$ and $y > 1 - \epsilon'$ to $\sim 10^{-20}$ m^2 s^{-1} at $\epsilon < y < 1 - \epsilon'$ may be related to a shift from a narrow diffusion-limited regime (i.e., the solid-solution end-members at low and high *y*) to a regime where phase-transformation kinetics is most likely limiting (i.e., the two-phase region in the mid-stoichiometry range). Therefore, in addition to single-phase diffusion, the VSSD implicitly accounts for effects related to the phase transformation. With this in mind, the potential loss captured by the VSSD model (case III in Figure 3-3b) can be attributed to sluggish phase-change kinetics within LFP particles.

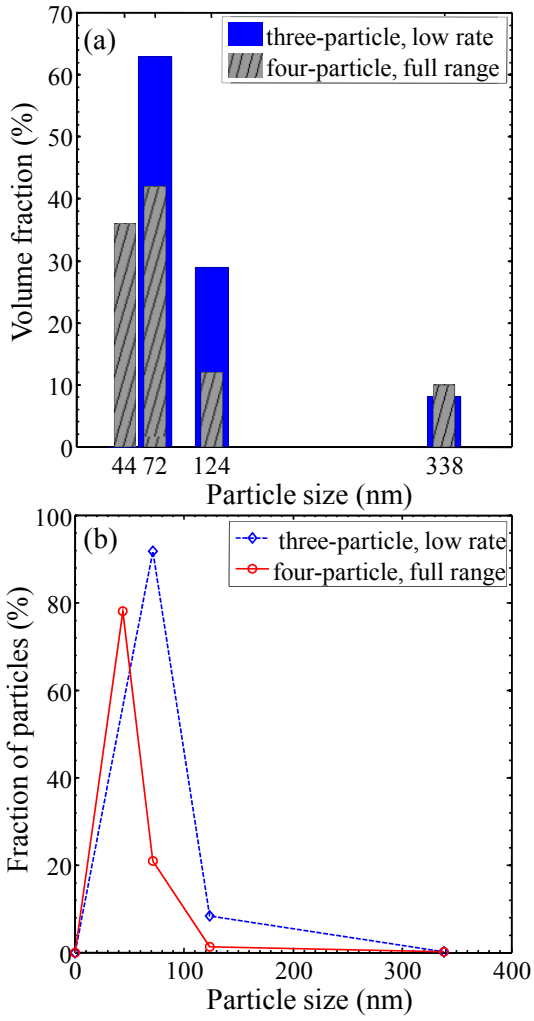

Figure 3-4. (a) Volume-based and (b) number-based PSDs obtained by fitting the VSSD model to the experimental galvanostatic data. The blue series in both figures are the values refined for low rate charge/discharge data (up to 1C) [16], while the red series are the values obtained through analysis of the full-range data (see Figure 3-3).

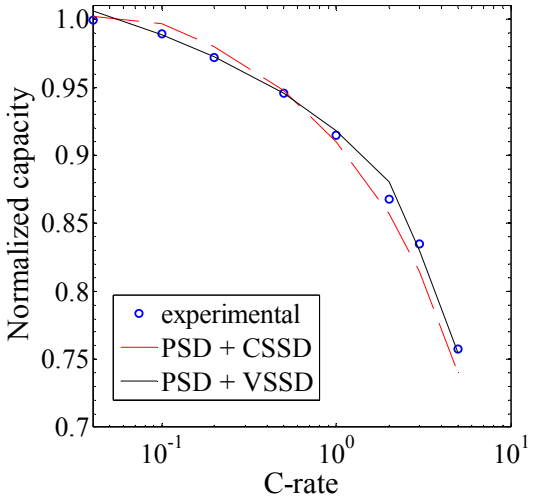

Figure 3-5. Comparison of rate capability plots obtained from experiments (circles), multi-particle constant-diffusivity model (PSD + CSSD, dashed line) and the VSSD model (PSD+VSSD, solid line). The end-of-discharge capacities are normalized with respect to the electrode end-capacity at C/25. PSD: particle-size distribution (Table 3-3), CSSD: constant solid-state diffusivity $\mathcal{D}_{\mathrm{LiS}} = 7\times10^{-19}$ m² s⁻¹ and VSSD: variable solid-state diffusivity (Figure 3-1b).

In Figure 3-5, the experimental (symbols) and simulated (black solid line) rate-capability based on the full VSSD model are compared against results obtained from a modified version of the model (red dashed line) which involves the same distribution of particle sizes, but sets the solid-state diffusion coefficient to a single constant value (i.e., $\alpha_{\mathrm{LiS},k} = 1.0$ and $D_{\mathrm{LiS},k} = 7 \times 10^{-19}$ m^2 s^{-1}). All the other parameters are the same in both versions of the model. Both simulations are found to be in good agreement with the experimental data, suggesting that the PSD is important in determining the rate capability of the electrode while the non-unity thermodynamic factor derived from the experimental equilibrium potential has a much smaller impact on the end-of-discharge capacities.

Radial lithium concentration profiles within the particles in each of the four size groups obtained during discharge at 5C are displayed in Figure 3-6. In each case, the particle is located at the separator/cathode interface. The profiles for each of the four sizes clearly show that the thermodynamically-consistent formulation in the VSSD model of LFP as a concentrated binary solution leads naturally to the two-phase core-shell scheme that has been envisioned for this material

[87, 88] without having to explicitly assume ad hoc that such a core-shell structure forms. The steep concentration profile between high-concentration ($y > 0.9$) and low-concentration ($y < 0.15$) bounds resembles the interface between Li-rich and Li-poor phases that initially forms close to the particle surface and subsequently moves inward as discharge proceeds. The surface concentration rises quickly to a large value ($y \simeq 0.9$) and remains almost constant until the end of discharge which is consistent with the assumption made in this analysis that the exchange current density is independent of the intercalant concentration at the particle surface (Eq. (3-5)).

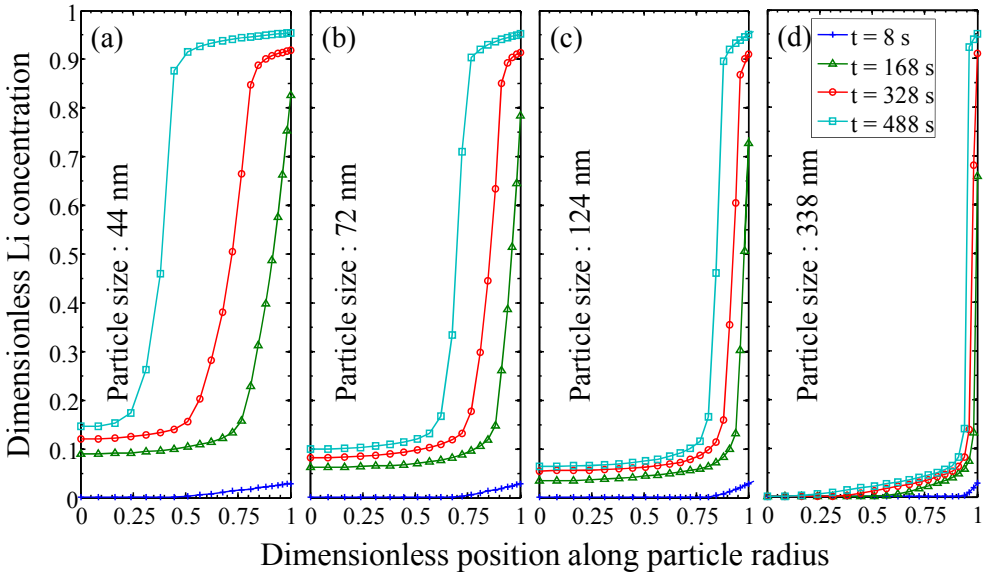

Figure 3-6. Concentration profiles of intercalated lithium within the four particle groups simulated by the VSSD model over the course of discharge at a rate of 5C. The corresponding potential-capacity curve is plotted in Figure 3-3. Particle surface is at *r* =1, center at *r* = 0.

Active material utilization in each particle group is calculated by integrating the concentration profiles with respect to the particle radius and the electrode thickness. Plots showing the variation in utilization of each particle group with overall electrode utilization are presented in Figure 3-7. As expected, the particle utilization at any given electrode utilization increases as particle size decreases. Also, the utilization of the smallest particle is greater than that of the electrode at all C-rates whereas the opposite trend is observed for 124 and 338 nm particles. The utilization of 72 nm particles, however, almost perfectly matches the electrode utilization over the entire capacity range (Figure 3-7b). It is not a coincidence that the d_{50} obtained from SEM image analysis is 72 nm and constitutes the largest active-material volume fraction. Needless to say, the particle utilization would

be equal to the normalized electrode capacity if the size of the LFP particles were assumed to be uniform rather than follow a PSD, as considered in this model.

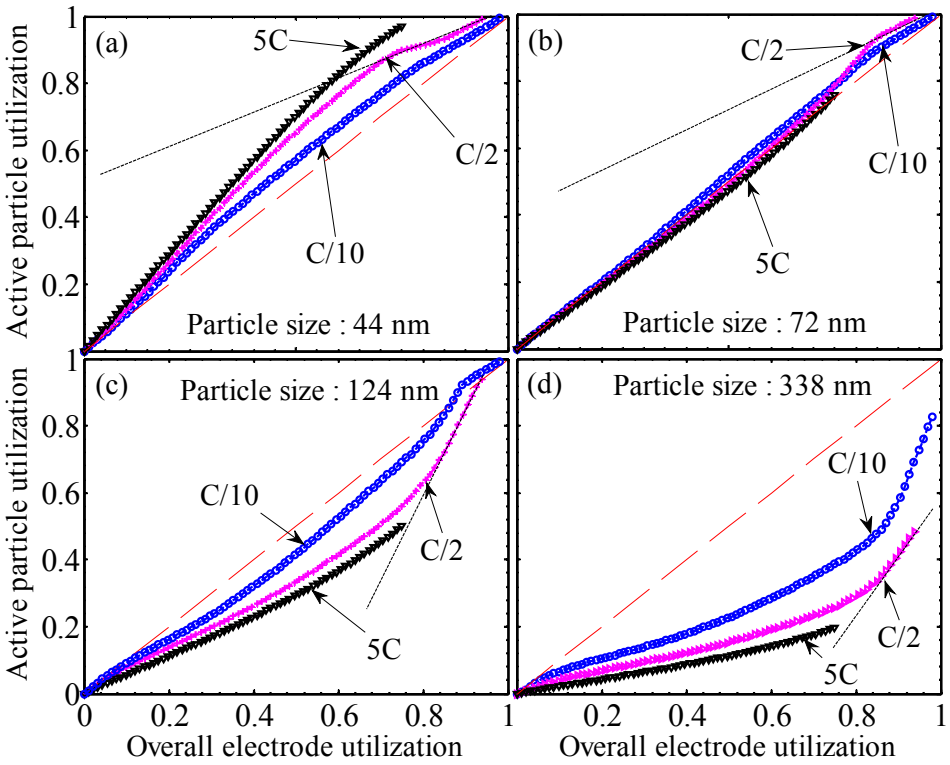

Figure 3-7. Simulated utilization of the four particle groups according to the VSSD model: (a) 44, (b) 72, (c) 124 and (d) 338 nm. Electrode and particle utilization are the ratios of coulombs transferred in an electrode and particle, respectively, at different stages of discharge to the estimated electrode capacity at C/50. The diagonal red dashed line represents the case where only 1 particle size rather than a PSD is considered in the model; the black dotted lines highlight the lithiation rates of each particle towards the end of C/2 discharge.

As evident in Figure 3-7, utilization of the smallest 3 particles reaches close to 1 at the end of C/10 discharge, while the largest particle uses more than 80% of its available capacity at this discharge rate. The 338 nm particle is almost fully lithiated at the end of C/25 discharge (i.e., the lowest current density, not shown here) indicating that the estimates for its size and volume fraction are likely reasonable. The largest two particles (Figure 3-7c and d) experience an increase in the partial current density (related to the rate of change of particle utilization versus the electrode utilization) while the other two (Figure 3-7a and b) approach their fully lithiated state at a decreased rate. This is illustrated by the tangent lines (dotted) to the curves for C/2 discharge. Overall, the

partial current density increases for 44 nm particles as the applied current increases while the opposite trend occurs for 124 and 338 nm particles, clearly demonstrating that the end-of-discharge capacities at different C-rates depend on several particle sizes.

3.3.2 Resistive-Reactant Model

In addition to the quantity of the conductive agent, the quality of carbon coating and the distribution of conductive filler around the LFP particles were shown to influence the electrode performance [92]. As done in the case of the VSSD model in the previous section, the RR model is explored to investigate performance limitations possibly brought about by the poor electronic conductivity of LFP. Similar to the VSSD simulations, high-rate galvanostatic discharges are of special interest since resistive-reactant effects, if significant, are obviously accentuated at high current.

Contrary to the situation of the VSSD model, LFP is assumed to be an ideal binary solution of the intercalant species and empty sites in this model. Consequently, the solid-state thermodynamic factor $\alpha_{\mathrm{LiS},k}$ is set to 1 and the solid-state Fickian diffusion coefficient is a constant. The effect of particle-size distribution is ignored and all particles are assumed to have the same size as the d_{50} obtained from SEM image analysis. The connection between the active material and the conductive matrix is defined in terms of a set of inter-particle contact resistances that are fitted to the data. According to Eqs. (3-3), (3-7) and (3-8), the contact resistances appear in the kinetic expression and modify the surface overpotential of the electrochemical reaction. The best-connected LFP particle experiences the largest reaction driving force and, therefore, is lithiated faster than others; the particle with the poorest connection is lithiated most slowly.

To make a fair comparison between the RR and VSSD models, electrode-level parameters and the rate constant are considered to be identical in both models (refer to Table 3-2). The RR model is fitted to the full-range constant-current discharge curves by adjusting i) the solid-state diffusion coefficient (assumed to be constant), ii) the resistances of the 4 groups of particles in contact with the conductive matrix and iii) the volume fractions of the particle groups. A comparison of the experimental and model-fitted curves for discharge rates ranging from C/25 to 5C is presented in Figure 3-8a. Apart from electrolyte limitations that are equally well accounted for in both models, the RR model can capture the “slanted behavior” of the experimental galvanostatic data at intermediate potentials, i.e., the variation of the electrode potential with the state of discharge, which increases with current density. According to the VSSD model, this particle-level contribution to the overall

potential loss is attributed to bulk limitations in terms of a concentration-dependent diffusion coefficient that accounts for diffusive and phase-change losses inside the LFP particles (Figure 3-3b).

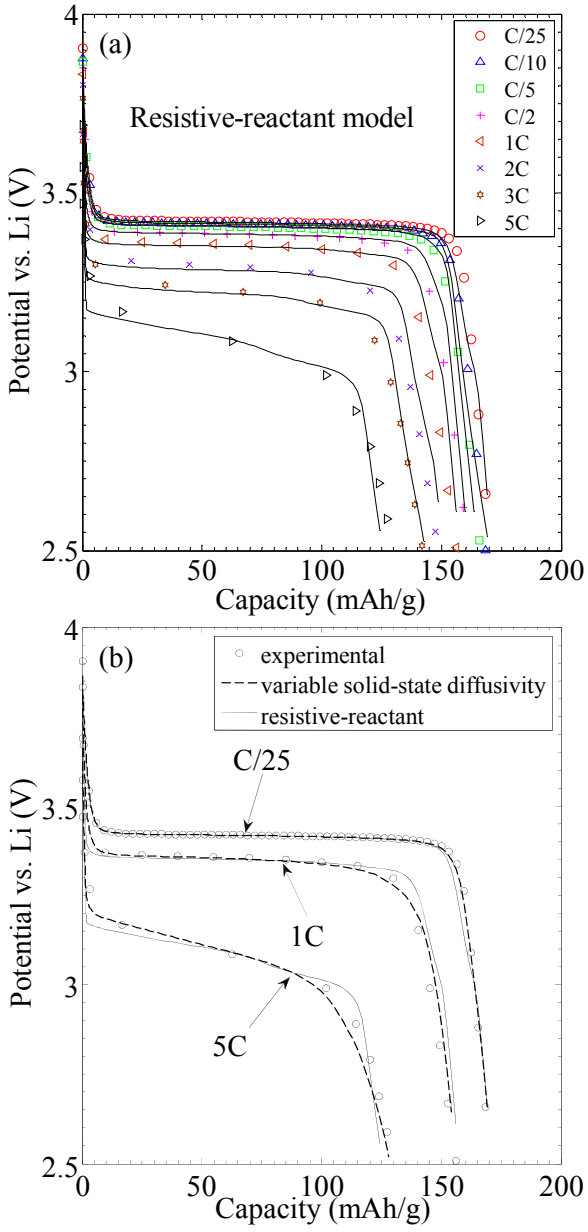

Figure 3-8. (a) Comparison of experimental (symbols) and RR model-fitted (solid lines) galvanostatic discharge curves. (b) Comparison of experimental (symbols) and fitted galvanostatic discharge curves according to the RR (solid lines) and VSSD (dashed lines) models. Model parameters are provided in Table 3-2 and Figure 3-10.

In addition to capturing the slanted behavior of the experimental potential-capacity profiles, the fitting of the contact-resistance distribution (CRD) allows the model to match the end-of-discharge capacities of the electrode especially at high C-rates. The simulated electrode rate capabilities with and without contact resistances are compared with the experimental data in Figure 3-9. The effect of using a CRD and different values of $\mathcal{D}_{\mathrm{LiS}}$ were assessed. The results show that the fit depends on both the use of a CRD and the best fitting value of $\mathcal{D}_{\mathrm{LiS}}$. The contact-resistance distribution impedes lithiation at the surface of the LFP particles until it eventually controls the end-of-discharge capacities (black solid line).

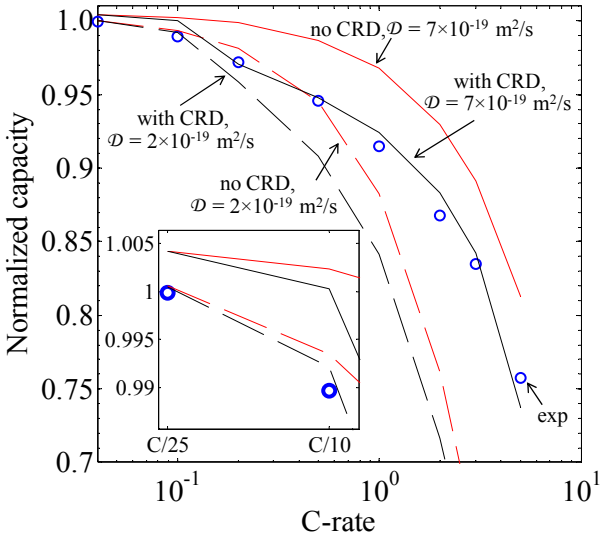

Figure 3-9. Comparison of rate capability curves obtained from experiments (circles) and 4 modifications of the RR model: i) no CRD included and $\mathcal{D}_{\mathrm{LiS}} = 7\times10^{-19}\ \mathrm{m^2\ s^{-1}}$ (red solid line), ii) CRD included and $\mathcal{D}_{\mathrm{LiS}} = 7\times10^{-19}\ \mathrm{m^2\ s^{-1}}$ (i.e., standard RR model, black solid line), iii) no CRD included and $\mathcal{D}_{\mathrm{LiS}} = 2\times10^{-19}\ \mathrm{m^2\ s^{-1}}$ (red dashed line) and iv) CRD included and $\mathcal{D}_{\mathrm{LiS}} = 2\times10^{-19}\ \mathrm{m^2\ s^{-1}}$ (i.e., standard RR model, black dashed line). End-of-discharge capacities are normalized with respect to the capacity measured at C/25. Inset: Mismatch between the end-of-discharge capacities obtained experimentally and from the RR model at low C-rates. Model parameters are found in Table 3-2 and Figure 3-10.

As evident in Figure 3-10, a severely skewed distribution of resistances containing one that is considerably larger than the others (i.e., $R_{c,4} = 100\ \Omega\ m^2 \gg R_{c,1},\ R_{c,2}$, and $R_{c,3}$) is obtained from the best fit of the RR model to the experimental data. However, the use of this CRD leads to some discrepancy of the fit of the model to the measured capacities at very low C-rates (i.e., C/25 and C/10) (see inset in Figure 3-9). From the results, the rate capability of the LFP electrode appears to be more sensitive to the diffusion coefficient than to the contact resistances (compare the simulation results with $\mathcal{D}_{LiS} = 7 \times 10^{-19}$ m^2 s^{-1} to those using $\mathcal{D}_{LiS} = 2 \times 10^{-19}$ m^2 s^{-1} in Figure 3-9), implying that lithium transport within the particles (i.e., diffusion coefficient and particle size) remains the major factor determining the end-of-discharge process even for electrodes that are composed of nano-sized LFP particles. It should be emphasized that the CRD in the RR model developed here accounts simultaneously for both the slanted behavior of discharge curves and the end-of-discharge capacities, in contrast to the VSSD model in which $\alpha_{LiS,k}$ is responsible for the SOC-dependent potential loss and the PSD for the end-of-discharge capacities.

In the final stage, the RR model is augmented by incorporating a distribution of particle sizes identical to that obtained for the VSSD simulations (Table 3-3). The modified resistive-reactant model (MRR) contains 4 groups of particles with different sizes each connected to the conductive matrix through a set of 3 contact resistances resulting in a 12-particle model. Each particle group in the PSD is assumed to have the same 3-bin CRD so that the model is fitted for only 5 additional parameters (i.e., 3 resistances and 2 volume fractions in the CRD). The entire set of PSD and CRD is presented in Table 3-4. The diffusion coefficient, reaction rate constant and electrode-level parameters are identical to those used for the RR simulations (refer to Table 3-2). As shown in Figure 3-11a, the introduction of the PSD into the original RR model improves the quality of the fits, particularly toward the end of discharge. Moreover, the deviation between the fitted and experimental end-of-discharge capacities at C/25 and C/10 is eliminated in this modified version of the RR model (Figure 3-11b). The new set of contact resistances is well distributed within a narrow range estimated to be less than 3 $\Omega\ m^2$, (Table 3-4), which is 2 orders of magnitude smaller than the largest resistance obtained in the original RR model (i.e., $R_{c,4} = 100\ \Omega\ m^2$) indicating that a large $R_{c,4}$ is responsible for low-rate end-of-discharge limitations and embeds possible effects of solid-state diffusion.

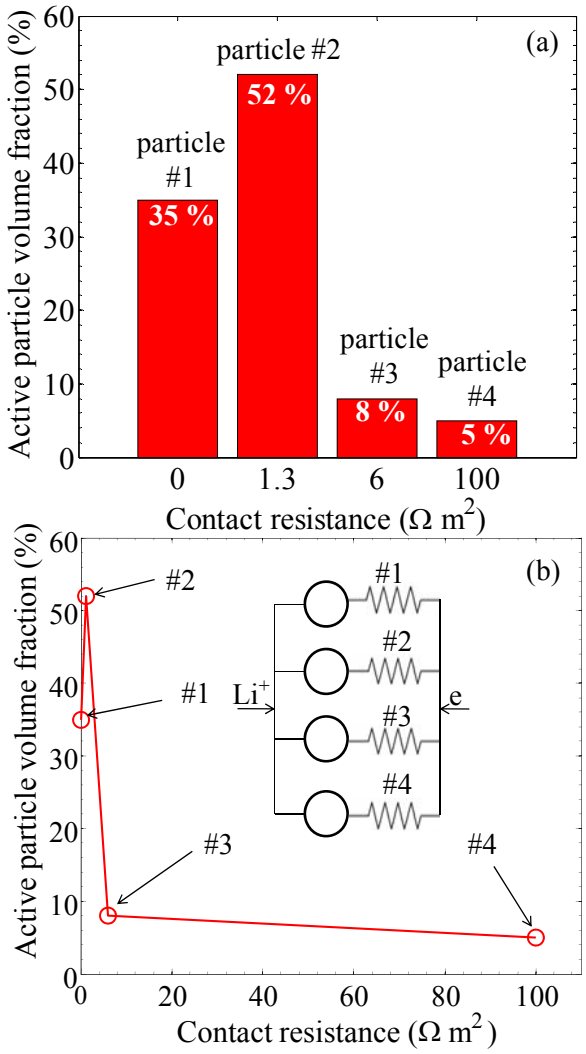

Figure 3-10. Contact-resistance distributions in terms of volume fraction that yields the fit of the RR model to the experimental curves presented in Figure 3-8a. Inset in (b) depicts the four particle groups (circles) with different electronic connectivities to the solid matrix.

Table 3-4. Particle-size and contact-resistance distributions included in the MRR model. *m* and *n* are indices for the particle bins in the PSD and CRD, respectively. $\varepsilon_{m,n}$ is the volume fraction of the $(m \times n)^{\text{th}}$ particle group referred to total active material volume and $\varepsilon_m = \sum_n \varepsilon_{m,n}$ and $\varepsilon_n = \sum_m \varepsilon_{m,n}$.

			n	1	2	3
			$R_{\text{c},n}$ ($\Omega\,\text{m}^2$)	0	1.3	3
			ε_n	0.35	0.40	0.25
m	$2R_{\text{p},m}$ (nm)	ε_m			$\varepsilon_{m,n}$	
1	44	0.36		0.126	0.144	0.09
2	72	0.42		0.147	0.168	0.105
3	124	0.12		0.042	0.048	0.030
4	338	0.10		0.035	0.040	0.025

In the VSSD model, the thermodynamic factor is obtained directly from the experimental equilibrium potential and so is not an adjustable parameter. Moreover, it contains information regarding complex phenomena occurring in the bulk of active material which partially explains the slanted behavior of the potential-capacity curves. Based on a simple size scaling, such a bulk-related potential loss is expected to be greater in larger LFP particles. In addition, under certain conditions, equilibrium thermodynamics of the system is influenced by the particle size [143]. The miscibility gap between the two coexisting phases has been shown to become smaller when the particle size decreases causing the phase-transformation hindrance to diminish and be limited within a narrower composition range [66, 144, 145]. Previous studies suggest that the electrode open-circuit potential deviates from a flat plateau at intermediate stoichiometries if the electrode contains particles with sizes below a critical value (e.g., 40 nm) that has been correlated to the existence of a single homogeneous phase (rather than being biphasic) over the entire stoichiometry range [65]. Aside from the modification of the miscibility gap, particle size has been suggested to inversely affect the redox potential plateau of LFP, i.e., the smaller the particle, the larger the equilibrium potential, although the effect is small (ca. 10 mV) [66, 146, 147]. A distribution of particle sizes will then lead to a

distribution of equilibrium potentials which in turn will cause the LFP electrode to exhibit a sloping open-circuit potential at intermediate stoichiometry [146, 147]. Although not explicitly included in the model, these effects will modify the calculated thermodynamic factor (i.e., proportional to the gradient of the electrode open-circuit potential with respect to the overall stoichiometry) and lead to a smaller potential loss induced by Li transport within LFP particles.

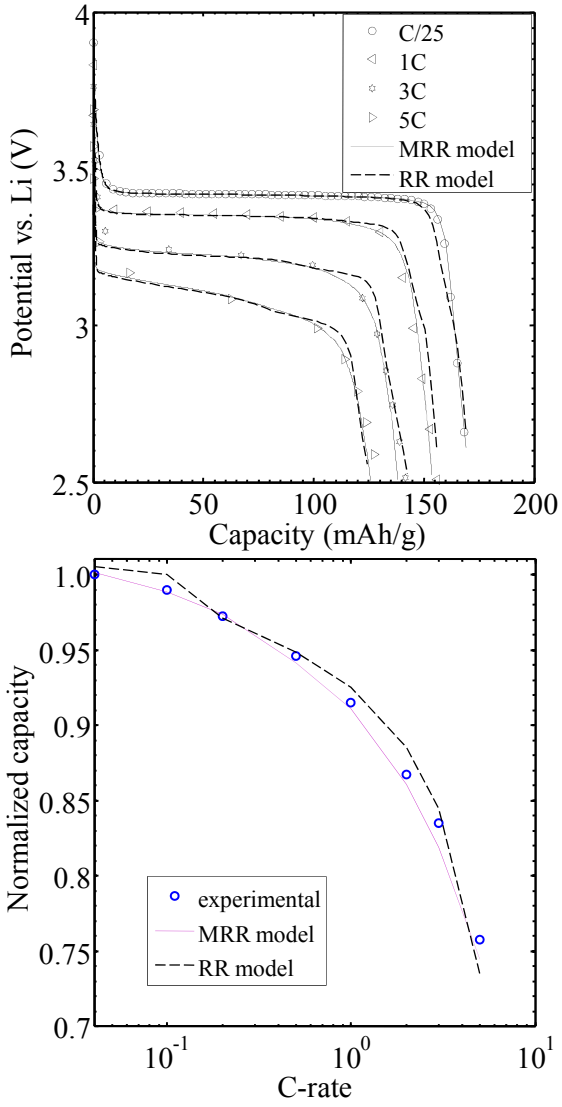

Figure 3-11. (a) Comparison of experimental (symbols), RR model-fitted (dashed lines) and modified RR model-fitted galvanostatic discharge curves. (b) Comparison of rate capability curves obtained from experiments (circles), fitted RR model (dashed line) and fitted modified-RR model (solid line).

On the other hand, some straightforward reasoning concerning the morphology of composite LFP electrodes may give hints about possible correlations between the active material particle size and the resistive-reactant effect. The ratio of the specific surface area of the active material to that of the conductive filler is much larger for an electrode made up of small active-material particles, provided that the surface area of the conductive additive per unit volume of electrode as well as the volume fraction of active-material do not vary from one electrode design to another and that the particle size is the only design parameter. Specifically, fewer contact points per unit active area of the electrode lead to a larger average contact resistance; hence, an electrode comprised of nanosize LFP particles (e.g., d_{50} = 72 nm in this study) is more likely to exhibit a resistive-reactant behavior than one with larger active particles having the same intrinsic properties.

Despite the comprehensiveness of the MRR model, the discrete nature of the CRD requires the incorporation of at least 3 contact resistances per particle size which introduces additional unknown parameters into the model (i.e., need to refine 5 more parameters compared to the VSSD model). This model is laborious in implementation and expensive in computation.

3.4 Conclusion

Two distinct models, the variable solid-state diffusivity model and the resistive-reactant model, are analyzed for a $LiFePO_4$-based electrode to study the two critical features of this compound: presumably slow solid-state Li transport and poor electronic conductivity, respectively. The models were separately applied to fit the experimental galvanostatic discharge data obtained from a commercial LFP electrode. These two models were experimentally validated over a full range of currents ranging from C/25 to 5C.

To obtain reasonable estimates of the adjustable parameters, operating conditions were divided into low discharge rate (up to 1C) and high discharge rate (from 1C to 5C) domains; low-rate simulations are highly sensitive to particle-level parameters but minimally influenced by the electrode-level properties constituting a useful guideline for parameter estimation. Particle-level parameters other than the PSD and CRD were estimated according to the low-rate data whereas electrode-level properties were refined to capture high-rate potential profiles. The particle-size distribution in the VSSD model and contact-resistance distribution in the RR model were obtained by fitting to the full range of currents. The same set of electrode-scale properties were used in both VSSD and RR models. Also, the reaction rate constant is taken to be identical in the two models. In

addition, an almost equal number of adjustable parameters were refined for the two models, i.e., 10 parameters for the VSSD model (if $\mathcal{D}_{\mathrm{LiS}}$ is also counted) and 11 parameters for the RR model.

Full-range simulations confirmed the effectiveness of the variable solid-state diffusivity as it significantly accounted for the electrode potential loss over the entire SOC range and captured the characteristic shape of the experimental discharge profiles. The concentration-dependent diffusion coefficient generates a SOC-dependent potential drop in addition to porous-electrode effects. It can be regarded as a lumped parameter that accounts for 1-D atomic diffusion, grain-boundary diffusion [57], inter-particle ionic transport [146], phase transformation and other effects that may exist in a real LFP electrode. It simplifies the description of the bulk of active material while yielding useful information in terms of overall electrode performance from a practical point of view. The particle-size distribution, on the other hand, turns out to play a pivotal role in predicting the rate capability of an LFP electrode whereas the thermodynamic factor appeared to have very little effect on the galvanostatic end-of-discharge capacities.

In the resistive-reactant model, a set of contact resistances is responsible simultaneously for capturing both the slanted behavior of the potential-capacity curves (i.e., additional to porous-electrode effects) and the end-of-discharge capacities at different C-rates. The model can explain the SOC-dependent part of the electrode potential loss attributed to bulk limitations in the VSSD model. The best fitted CRD, however, over-predicted the capacities at very low C-rates. Further improvement of this model required the incorporation of a particle-size distribution in the RR model.

From a comparison of the RR, modified RR and VSSD models, it appears that the VSSD model is a simpler yet physically descriptive model for use as a reliable platform for practical situations. Such situations include performance analysis, thermal studies and lifetime prediction of LFP-based commercial batteries. To the best of our knowledge, no clear experimental evidence of changes to LFP electrode properties upon aging has been reported in the literature. Nevertheless, if this question is of interest, both models can be used to precisely analyze an LFP electrode at different stages of aging (e.g., increase of contact resistances over time in the RR model and modifications of the PSD in the VSSD model).

Based on the comparative study and the assumptions made, it is concluded that both the resistive-reactant effect and bulk-related rate limitations exist in an LFP electrode and can significantly affect its power capability. Portions of the total electrode potential loss are ascribed to

solid-state Li transport limitations in the VSSD model and to contact resistances at the particle surface in the RR model. Resistive-reactant losses (or bulk-related limitations) are artificially contained within the common model parameters in the VSSD (or RR) model. The two may be combined to yield a comprehensive mixed-control model. With the knowledge that bulk transport, resistive-reactant effects and porous-electrode effects constitute the total potential loss of an electrode, accurate ex-situ measurement of electrode-level transport properties will help quantify the extent of the bulk and surface effects on a specific LFP electrode.

Chapter 4

Mesoscopic Modeling of Li Insertion in Phase-Separating Electrode Materials: Application to Lithium Iron Phosphate

The following chapter is based on previously published work by M. Farkhondeh, M. Pritzker, M. Fowler, M. Safari, and C. Delacourt in *Phys.Chem. Chem. Phys.* entitled:

"Mesoscopic Modeling of Li Insertion in Phase-Separating Electrode Materials: Application to Lithium Iron Phosphate"

This thesis author's specific contribution to this paper was to develop the model, conduct simulations, prepare all the graphics and results, prepare the manuscript and reviewer edits with direction from the project advisors who were co-authors. All authors reviewed the manuscript.

4.1 Introduction

As described in section 2.1, LFP phase transformation is characterized by an equilibrium potential that does not vary with the electrode SOC. Most conventional continuum models describe this phase transformation by juxtaposing the two phases within the bulk throughout the charge/discharge process[15, 16, 57, 85-100]; these models include the Kolmogorov-Johnson-Mehl-Avrami model [15, 98, 99], reformulated phase-field models for open systems [85, 86, 90, 91, 93-97], core-shell-type models [57, 87-89, 92, 101] and non-ideal solid-solution models (developed and presented in Chapter 3) [16, 100, 102].

In contrast to the idea of the two end-members coexisting in the same particle, recent phase mapping experiments on electrochemically lithiated/delithiated LFP electrodes have shown that the total Li content of the electrode is distributed between two distinct groups of particles that are either Li-rich or Li-poor [73-76]. Dreyer's many-particle model predicts this behavior by allowing particles in a porous electrode to randomly exchange Li^+ ions and electrons through the electrolyte and the conductive matrix, respectively [14, 83]. The state of the electrode evolves from a given initial condition quasi-statically (i.e., at a very low rate) whereby the configurational entropy accounts for the stochastic exchange of matter among LFP particles. The model is also able to predict the flat equilibrium potential at the mid-stoichiometry range and the quasi-static hysteresis between the

electrode potential on charge and on discharge. In general, whether the actual particles undergo rapid domino-cascade-like filling/extraction of *b* channels or a non-equilibrium solid-solution lithiation/delithiation pathway during charge and discharge depends on the particle geometry (i.e., size and shape), synthesis route, temperature and applied potential/current [148]. Dreyer's many-particle model, however, does not rely on any specific mechanism for mass transfer/phase transition within individual particles and only investigates the evolution of the LFP electrode from a fully charged (discharged) state to a fully discharged (charged) state merely by incorporating thermodynamic considerations. Only a few continuum models in the literature consider many-particle interactions and attribute the "discrete filling" of LFP nanoparticles to porous-electrode limitations [149, 150] or the architecture of nanoparticulate electrodes [151].

Aside from the flat equilibrium potential, LFP electrodes exhibit other unique features, namely: (i) outstanding rate capability [10], (ii) development of positive intensities between the X-ray diffraction peaks of the end-members during high-rate cycling [11, 12], (iii) cycle-path dependence [13], (iv) quasi-static potential hysteresis [14], (v) non-monotonic current response to potential steps [15] and (vi) mismatch of electrode potential between continuous and intermittent galvanostatic operation modes [16, 17]. The first feature has been attributed to a potential- or current-dependent alteration of the insertion mechanism from a biphasic to a stable single-phase solid-solution pathway in some phase-field simulations [85, 94] and has been addressed by introducing multiple particle bins in the core-shell [57], resistive-reactant [59] and variable diffusivity [100] models (as described in Chapter 3). The second feature has been justified through a rate-dependent phase-transition pathway described in Refs. [85, 94]. The third feature has been accommodated in the core-shell model by the appearance of multiple onion-like layers of Li-rich and Li-poor end members within a single particle whenever charge/discharge cycles are incomplete [13]. In the resistive-reactant model of Ref. [59], this effect has been related to the existence of multiple particle bins with different electronic connectivities to the conductive matrix. The fourth feature has been explained in terms of the inter-particle communication of species in the many-particle model [14], while the fifth has been attributed to the nucleation and growth mechanism in KJMA-based models [15, 98].

In addition to these known features of LFP electrodes, Sasaki and co-workers [17] have recently reported the existence of a so-called "memory effect" for this biphasic Li insertion material. An anomalous increase in the electrode polarization is observed when the full galvanostatic charge/discharge of the LFP electrode is preceded by a partial charge/discharge cycle. They attributed

this effect as well as the galvanostatic pulse polarization mismatch, to many-particle effects and hindrance associated with nucleation or spinodal decomposition within the particles.

Despite rigorous research in the literature, a single practical model that can predict all of the above-mentioned irregularities and pinpoint the dominant contributing factors is still lacking. This chapter presents a simple mesoscopic model that is able to simultaneously explain the memory effect and other unique phenomena observed in phase-transforming battery materials that have just been enumerated.

4.2 Model Development

The model disregards the geometric details associated with choosing between inter- and intra-particle phase-change mechanisms by defining "elementary lithiating/delithiating units" which are large enough to contain a substantial number of reaction sites and for the continuity to hold (in contrast to atomic-scale models), but small enough at the scale of the bulk so that no intra-unit phase transition occurs (Figure 4-1). These mesoscopic units constitute the total active material loading of the electrode and may be interpreted as single Li channels lying along the *b*-axis, crystallites within a polycrystalline particle or even nanoparticles in a nanoparticulate porous electrode. An elementary unit is the smallest entity that can exchange species with its counterparts through the surrounding electronic and ionic conduits and its length scale may be defined according to the type of LFP particles making up the electrode. Such mesoscopic units resemble bi-stable elements in Preisach magnetization models or other homogenized energy models developed earlier for smart materials [152]. The term "unit" is used throughout this manuscript for notional convenience.

The mathematical setting presented is deliberately kept simple and includes only the constituents necessary for demonstrating many-particle effects and avoids the description of phenomena that are already known in a porous battery electrode. Thus, the following main assumptions are made: i) chemical potential of Li in each unit is a non-monotonic function of composition, ii) units are lithiated/delithiated homogeneously, i.e., mass transfer limitations are not included, iii) possible mechanical effects are ignored, iv) a distribution of resistances exists among the units and v) porous-electrode effects are ignored.

In the simplest approximation, the dependence of the single-unit equilibrium potential U_k on its composition y_k can be derived from the regular solution model for a binary system containing occupied and vacant Li sites (one-parameter Margules activity-coefficient model):

$$U_k = U^0 + \frac{gRT}{F}\left(y_k - \frac{1}{2}\right) + \frac{RT}{F}\ln\left(\frac{1-y_k}{y_k}\right), \tag{4-1}$$

where subscript $k \in \{1, 2,\ldots, N\}$ denotes a specific bin containing elementary units with similar properties, U^0 is the standard equilibrium potential, R is the universal gas constant, T is the temperature and F is the Faraday constant. The second term on the right side of Eq. (4-1) is associated with the enthalpy of mixing of the inserted Li atoms and Li vacancies in the solution which can be zero ($g = 0$ in an ideal solution), negative ($g < 0$, repulsion of like neighbors) or positive ($g > 0$, attraction of like neighbors). The significant attraction of like neighbors (i.e., $g > 4$) causes single-phase instability over the intermediate composition range and eventually leads to a non-monotonic dependence of the equilibrium potential on the lithium concentration. In brief, the interaction coefficient determines the extent to which the inserted Li atoms and vacancies are miscible. A similar thermodynamic model was employed in the many-particle model developed in Refs. [14, 83].

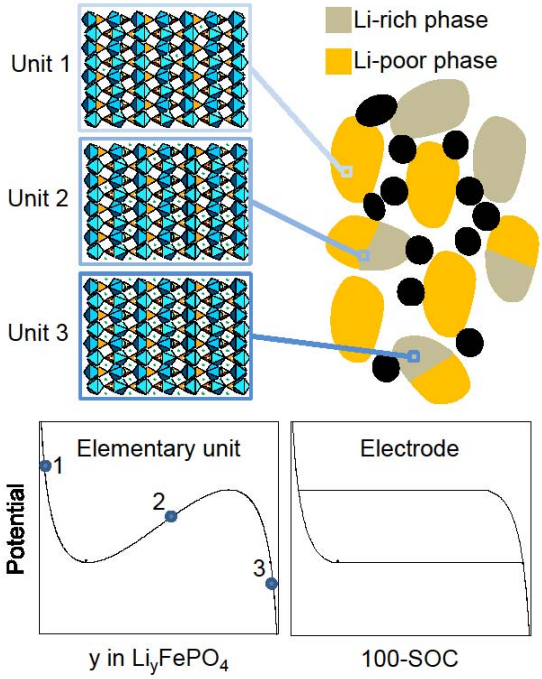

Figure 4-1. Schematic diagram of the mesoscopic model proposed for a phase-change battery electrode. Bi-stable elementary units depicted in the top left above constitute the electrode ensemble shown on the top right.

The overpotential experienced by lithiating/delithiating units is assumed to arise from an ohmic hindrance R_k (in Ω mol) that impedes the insertion/de-insertion reaction and is specific to each bin:

$$\Phi - U_k = R_k i_k, \tag{4-2}$$

where Φ is the electrode potential and i_k is the partial current per mole of active material in bin *k* and is negative when the bin is being lithiated. It should be emphasized that, according to assumption (v) above, all units are connected to an isopotential source/sink of electrons (conductive matrix) and Li ions (electrolyte). This is a reasonable assumption if the porous electrode is sufficiently thin and dilute in terms of active material loading. Assuming a uniform Li concentration within a unit, the partial currents contributed by this unit is related to the change of the Li concentration in the bin through a simple material balance expression:

$$i_k = -F \frac{\partial y_k}{\partial t}. \tag{4-3}$$

The assumption of a uniform concentration within each unit is not too unrealistic; recent experiments on electrochemical [10, 153] and non-electrochemical (gas phase) [154] delithiation of LFP have revealed that Li transport within LFP particles is very fast, with a Fickian diffusion coefficient of ~ 10^{-13} to 10^{-15} m^2 s^{-1} that agrees well with earlier theoretical calculations (~ 10^{-12} m^2 s^{-1}) [69, 155] but at odds with solid-state diffusion-limited models such as those analyzed earlier in Chapter 3.

The total current density *I* applied to the electrode is related to the partial molar currents i_k entering/leaving the parallel bins as follows:

$$I = c_{\max} l_{\text{cat}} \varepsilon_t \sum_{k=1}^{N} \varepsilon_k i_k, \tag{4-4}$$

where l_{cat} is the electrode thickness, ε_t is the total active material volume fraction in the electrode, ε_k is the fraction of active material in bin *k* and $c_{\max}$ is the maximum lithium concentration in the active material (assumed constant since volume changes associated with lithiation/delithiation are ignored). No assumption concerning the unit geometry is made in the model. No transport limitation inside the units is considered and the model only accounts for the ohmic limitations of active material. The resistance varies from $R_{\min}$ for units in bin 1 all the way to $R_{\max}$ for units in bin *N*, according to the

following expression $R_k = \frac{1}{N-1}(R_{\max} - R_{\min})(k-1) + R_{\min}$, and volume fractions of the bins of units are assumed to follow a Gaussian distribution:

$$\varepsilon_k = \frac{\frac{1}{S\sqrt{2\pi}} \exp\left(\frac{-(R_k - \overline{R})^2}{2S^2}\right)}{\sum_{k=1}^{N} \frac{1}{S\sqrt{2\pi}} \exp\left(\frac{-(R_k - \overline{R})^2}{2S^2}\right)} \tag{4-5}$$

where S is the standard deviation and $\overline{R}$ is the mean resistance, i.e., $\overline{R} = (R_{\min} + R_{\max})/2$. This resistance distribution represents a statistically non-uniform physico-chemical property within the LFP electrode. In an electrode where LFP particles are large enough so that they contain a number of units, the distribution reflects that inner units are surrounded by units only whereas outer ones are partially surrounded by electrolyte. In an LFP electrode where units feature LFP nanoparticles, the distribution is in line with earlier resistive-reactant models [59, 92] which rely on the poor electronic conductivity of LFP.

4.3 Results and Discussion

The model parameters used in this study are listed in Table 4-1. The values of l_{cat}, ε_t and $c_{\max}$ correspond to a sample LFP electrode with a total capacity of 2.05 mAh and geometric area of 1.2 cm^2 studied earlier in Chapter 3. The interaction coefficient g is fitted so that the predictions of the model presented here match the experimental data in Ref. [14] under quasi-static conditions. U^0, $\overline{R}$ and S are estimated so that the simulations match the experimental charge/discharge curves at C/2 reported by Sasaki et al. [17].

Table 4-1. Parameters used in the model.

Parameter	Symbol	Value
Number of elementary-unit bins	N	100[a]
Minimum resistance (Ω mol)	$R_{\min}$	6.08×10^{-5}[f]
Maximum resistance (Ω mol)	$R_{\max}$	6.08×10^{-3}[f]
Standard deviation (Ω mol)	S	1.28×10^{-3}[f]

Standard equilibrium potential (V vs. Li)	U^0	3.427[f]
Interaction coefficient in the Margules activity-coefficient model	g	6[f]
Electrode thickness (m)	l_{cat}	80×10^{-6} [100]
Total active-material volume fraction	ε_t	0.351 [100]
Maximum solid-phase Li concentration (mol m^{-3})	$c_{\max}$	22,806[a]

[a]: assumed; [f]: fitted.

Whereas the original many-particle model was limited to quasi-static operation [14, 83], the present model is used for both low- and high-rate conditions, while disregarding transport limitations at the unit and electrode scales for the sake of simplicity. As shown in Figure 4-2a, the model is able to predict the wide potential plateau that is typically observed during both charge and discharge potential-composition curves of two-phase battery materials. In the case shown, a very low rate (C/1000) is considered to galvanostatically charge and discharge an LFP electrode. Points labeled from 1 to 7 correspond to the results obtained over a time sequence during the C/1000 discharge. Also, the simulated curves exhibit hysteresis whereby the plateaus appear at different potentials during charging and discharging without resorting to any consideration of coherency strain energy [135], in agreement with experimental observations and simulation results from a previous many-particle model [14]. The single-unit equilibrium potential is also included in Figure 4-2a for comparison. Figure 4-2b shows the dynamics of quasi-static electrode lithiation. The bin utilization is color-coded from deep blue for fully-delithiated to dark red for fully-lithiated states. Based on the model, units accommodate either the Li-poor phase or Li-rich phase at any given time and only a few bins (e.g., only 1 or 2) have intermediate concentration (i.e., energetically unstable) corresponding to the narrow boundary between the two regions. In other words, units are segregated into two groups, one being Li-rich and the other being Li-poor and the lithiation process occurs in a "unit-by-unit" sequence. The narrow boundary indicates that lithiation proceeds as a distinct reaction front propagating among units during the electrode discharge. The numbered lines correspond to the numbered points on the discharge curve in Figure 4-2a. The reaction front is expanded in Figure 4-2c in terms of the Li content of each bin at the indicated times. At the start of discharge, units are filled together at the same rate (C/1000) while maintaining an identical Li concentration (i.e., solid-solution domain) until a point is reached where even a small change of Li concentration in one unit moves it into the unstable region. This, in turn, triggers the fast traverse of the unit content across the mid-

composition range, which is not energetically favorable (i.e., adequate driving force Φ - $U_k(y_k)$), to the Li-rich branch of the single-unit equilibrium potential. The process starts from the least resistive unit and ends with the most resistive one. Since all units are electronically and ionically connected, they experience the same electric potential Φ throughout the lithiation process. In the case of quasi-static operation, this potential remains almost identical to the single-unit equilibrium potential of the lower spinodal node (i.e., U_k where $\frac{\partial U_k}{\partial y_k} = 0$) until the last unit leaves the spinodal node and crosses the unstable region. The fluctuations in the electrode potential observed along both the discharge and charge plateaus in the simulated potential-utilization curves are artifacts of the model since they are caused by the sequential filling of the bins. They are expected to smooth out and eventually vanish if the resistance is distributed across a larger number of bins (i.e., continuum limit).

With an increase in the applied current, Φ deviates significantly from the spinodal node potential and enough driving force is now provided for all units to participate in charge transfer to an extent that is governed by their resistances. Consequently, the lithiation mechanism moves from a purely sequential unit-by-unit mechanism to a mixed sequential-parallel regime at high-rate charge/discharge. This change in the lithiation mechanism with applied current is demonstrated in Figure 4-3b and Figure 4-3c where a much wider range of bin utilizations between Li-rich and Li-poor states is observed than is found in the quasi-static condition in Figure 4-2b. Along with the presumed fast Li transport inside the units, this effect can explain the outstanding rate capability (end-capacity as a function of applied current) of LFP electrodes. This is in line with the apparent dependence of particle size or rate constant on applied current in the single-particle analyses of Refs. [141] and [59] where lower apparent particle radius or greater rate constant is required, respectively, at high current for model simulations to agree with experiments. It is also in agreement with the analysis of Chapter 3 where the PSD appears to be rate-dependent, i.e., the fitted PSD is shifted towards smaller particles in order to accurately predict the electrode performance during galvanostatic discharge at higher currents. The increase in the population of simultaneously lithiating bins at high rates agrees qualitatively with the change of the insertion mechanism from a two-phase to a solid-solution pathway that was inferred from the development of positive intensities between the $Li_{1-\epsilon'}FePO_4$ and $Li_{\epsilon}FePO_4$ reflections during operando XRD analysis of electrodes under rapid charge/discharge cycles [11, 12]. Units with lower resistance carry higher partial currents until they become fully lithiated (left branch of the curves at given snapshots in Figure 4-3c) after which their

partial currents drop toward zero. Since the total current would have to be accommodated by the remaining more resistive units, this would cause them to become more polarized and the cell potential to drop leading to the downward slope in the discharge curve at intermediate electrode utilization.

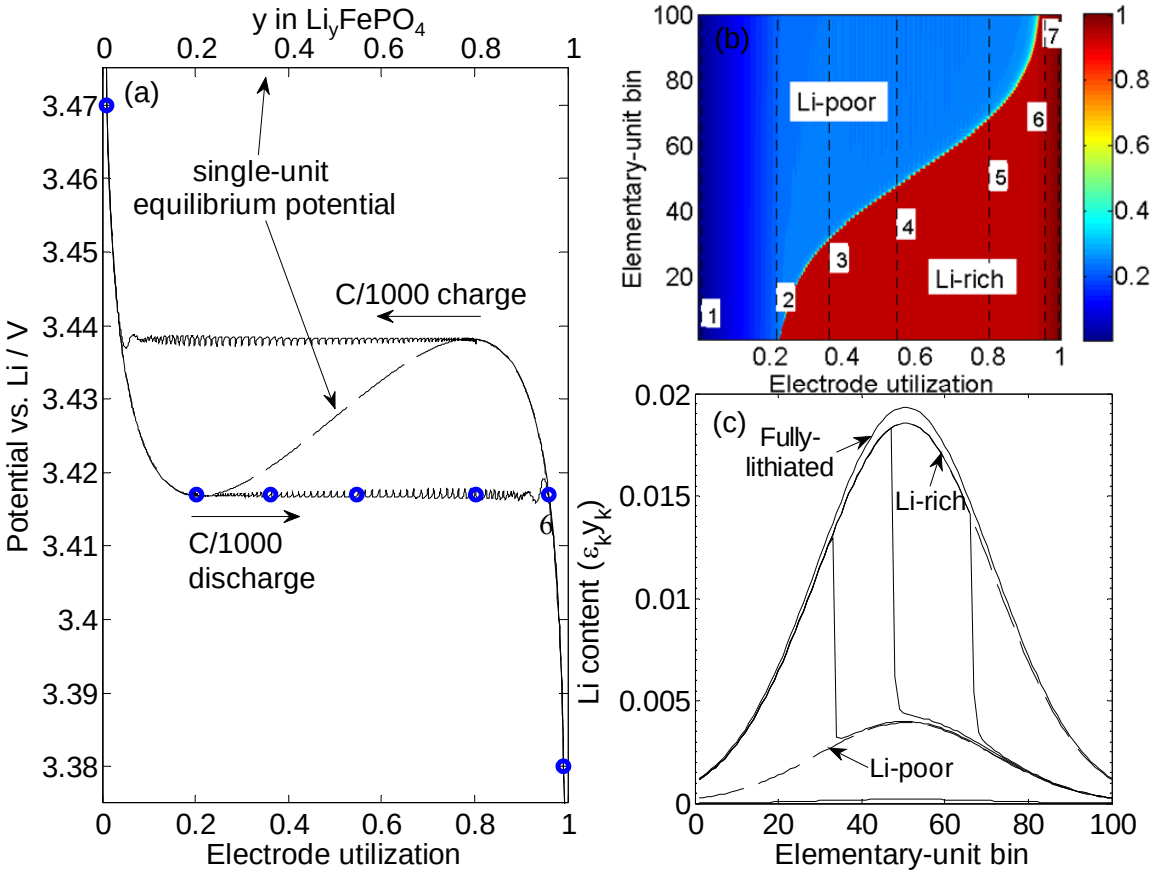

Figure 4-2. (a) Voltage profile of the many-unit electrode undergoing slow galvanostatic charge/discharge (C/1000, quasi-static) compared with the single-unit equilibrium potential. (b) Bin utilization versus electrode utilization during C/1000 discharge. Numbers 1 to 7 correspond to the blue points indicated in (a). (c) Lithium content of each bin at different times during C/1000 discharge.

Intuitively, a purely parallel lithiation mechanism would be ideal and lead to the most efficient electrode operation. Such a condition would occur if the physico-chemical properties of the units as well as their ionic/electronic environment were perfectly uniform throughout the electrode. However, this is seldom the case in an actual many-unit ensemble and the limitations associated with sequential lithiation described above are unavoidable. In the model presented here, the intra-unit

limitations are intentionally disregarded and the ohmic resistance distribution determines the sloping behavior and end-capacity of the potential-capacity curves. It implies that any improvement of the resistance distribution (i.e., broadness and mean value) that shifts the lithiation mechanism toward parallel dynamics will enhance the electrochemical performance of the LFP electrode. A similar statement can be made for other distributed properties in an actual electrode such as unit size, single-unit equilibrium potential and/or ionic/electronic resistances across the electrode.

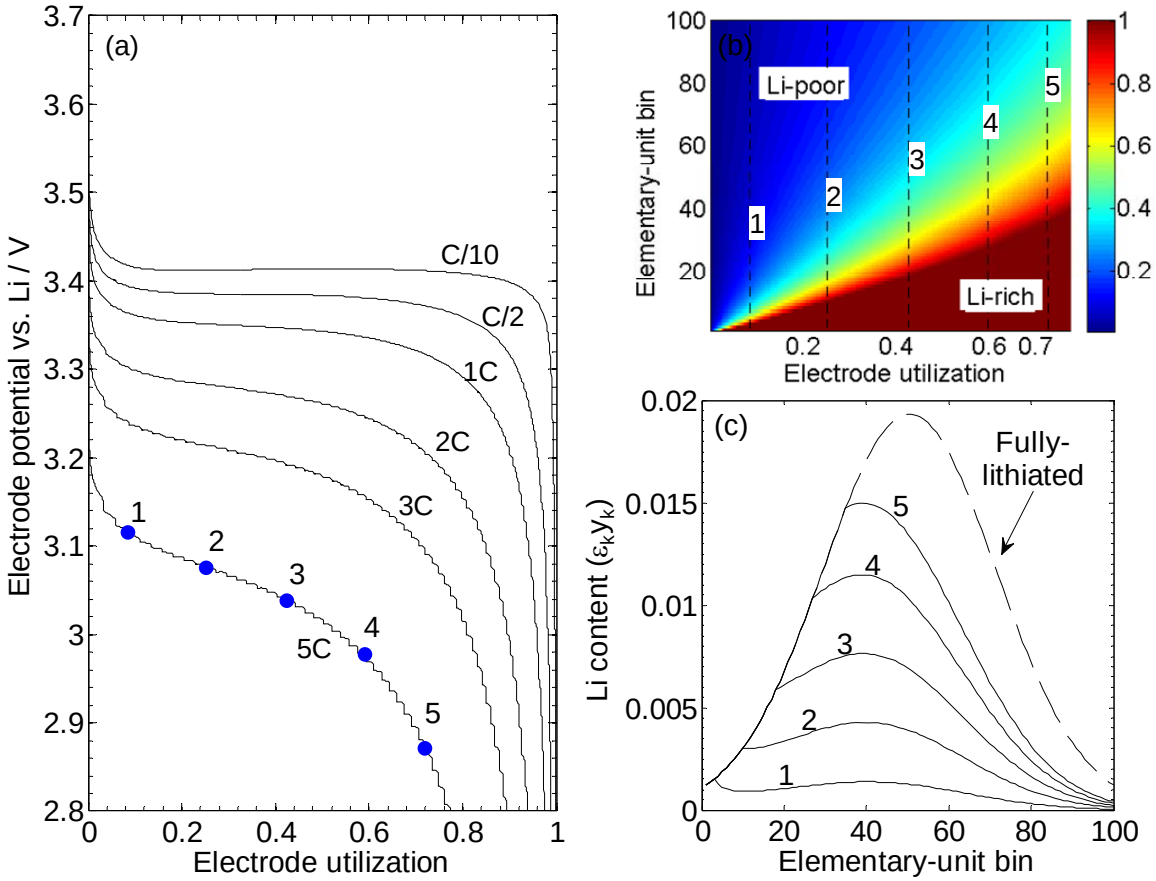

Figure 4-3. (a) Galvanostatic discharge curves at different C-rates. (b) Bin utilization versus electrode utilization during discharge at 5C. (c) Li content of units in each bin at different times during discharge at 5C.

The memory effect in Li-ion batteries is defined as an abnormal potential overshoot observed in the charge-discharge cycle immediately following a partial charge-discharge cycle [17]. The

mesoscopic model presented here is used to predict the results obtained from a set of virtual experiments that mimic the actual experiments described in Ref. [17]. This experiment consists of a sequence of 3 stages: memory-writing, memory-release and regular cycles. The initial condition is set to $y_1 = y_2 = \ldots = y_N = 0.975$ (i.e., SOC = 2.5%) in the units so that the electrode is, in practice, fully discharged at the outset. Starting from this state, the electrode is first charged (at C/4, C/2 or 1C) to a certain state-of-charge (30%, 50% or 70%) whereupon it is allowed to rest for 1 hour. This is followed by a discharge step that brings the electrode back to the initial SOC (memory-writing cycle). After another rest period (1 minute, 10 minutes, or 1 hour), the electrode is fully charged (SOC = 100%) and then allowed to rest for 1 hour before being discharged to the initial SOC (memory-release cycle). The third cycle is a repetition of the second one as a control to confirm the observations (regular cycle). As shown in Figure 4-4a-c (compare with Figure 2 of Ref. [17]) the potential bump appearing during the memory-release cycle (red line) coincides with and tracks the depth of the memory-writing cycle (blue line), i.e., the electrode potential remembers the depth of the previous shallow cycle. Also, fully charging of the electrode erases the memory effect and the bump is no longer observed during the subsequent charge-discharge cycles (regular cycle, black line). The effects of the release cycle rate, rest time between the writing and release cycles and the repetition of multiple memory-writing cycles are presented in Figure 4-4d-f, respectively. The results show that the potential anomaly is amplified by increasing the applied current during the release cycle, which stems from the resistive nature of the units assumed in the model. For a writing cycle of 50% charge-50% discharge, the relaxation time inversely affects the memory effect, i.e., the potential bump diminishes and ultimately disappears as the relaxation time is increased. In addition, the memory effect is enhanced by repeating the same memory-writing cycle a number of times (Figure 4-4f).

The impact of the depth-of-discharge of the memory-writing cycle is shown in Figure 4-5a-c. The memory effect becomes more pronounced as the depth of discharge decreases and the writing cycle becomes more imbalanced. Moreover, the potential overshoot does not disappear after a long relaxation step succeeding the 50% charge-40% discharge cycle (Figure 4-5d), which contrasts with the balanced memory-writing cycle described earlier (Figure 4-4e). The simulation results for all of the above-mentioned operations agree qualitatively with the reported experimental results [17] in spite of the simplicity of the model, implying that the incorporation of the non-monotonic single-unit potential and the resistance distribution in the many-unit effects is responsible for these observed phenomena.

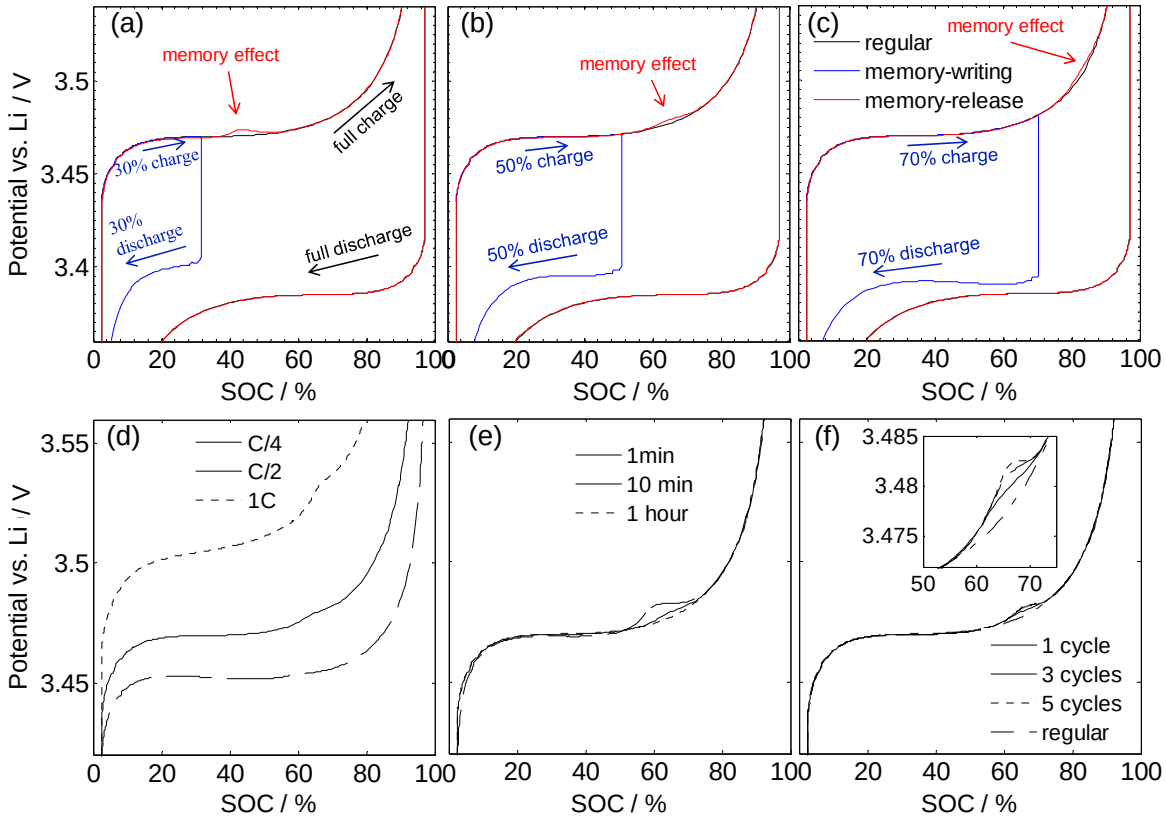

Figure 4-4. Memory effect upon (a) 30%, (b) 50% and (c) 70% partial charge-discharge memory-writing cycles, as indicated by the red arrow. Effects of (d) memory-release rate, (e) rest time between the memory-writing and memory-release cycles and (f) number of successive memory-writing cycles on the extent of the memory potential bump. The rate for both memory-writing and memory-release cycles is C/2 with 10 minutes of relaxation time between the writing and release cycles, unless otherwise stated. The memory-writing cycle is 50% deep unless otherwise stated.

In order to gain further insight into the above observations, unit utilizations are plotted in Figure 4-6 at the outset and end of the steps constituting the memory-writing cycle for the selected experiments. Theoretically, a fully-discharged electrode would consist of elementary units with Li concentration equal to 1; in practice, however, this is not the case and the end-capacity deviates from the theoretical value as the applied current increases (e.g., C/2, the experimental condition used by Sasaki et al. [17]). Therefore, the initial concentration of Li in the units is set to be below 1 and within the Li-rich solid-solution region according to the single-unit equilibrium function. This also guarantees zero inter-unit exchange of species and initial stability of the electrode. Although not

included here, simulations with zero initial state-of-charge did not generate any memory effect for a perfectly balanced memory-writing cycle. At the same time, the results in Figure 4-5 show that the memory effect becomes more pronounced as the memory-writing cycle becomes more imbalanced. Taken together, these findings indicate that a necessary condition for the memory effect to appear in an LFP electrode is the existence of a non-zero residual capacity at the onset of memory-release charging which may originate either from a non-zero initial SOC or from an imbalanced writing cycle. A memory effect should therefore not be observed in an electrode that has been preconditioned at extremely low currents (i.e., zero initial SOC) and has undergone an extremely slow memory-writing cycle (i.e., approaching a balanced cycle).

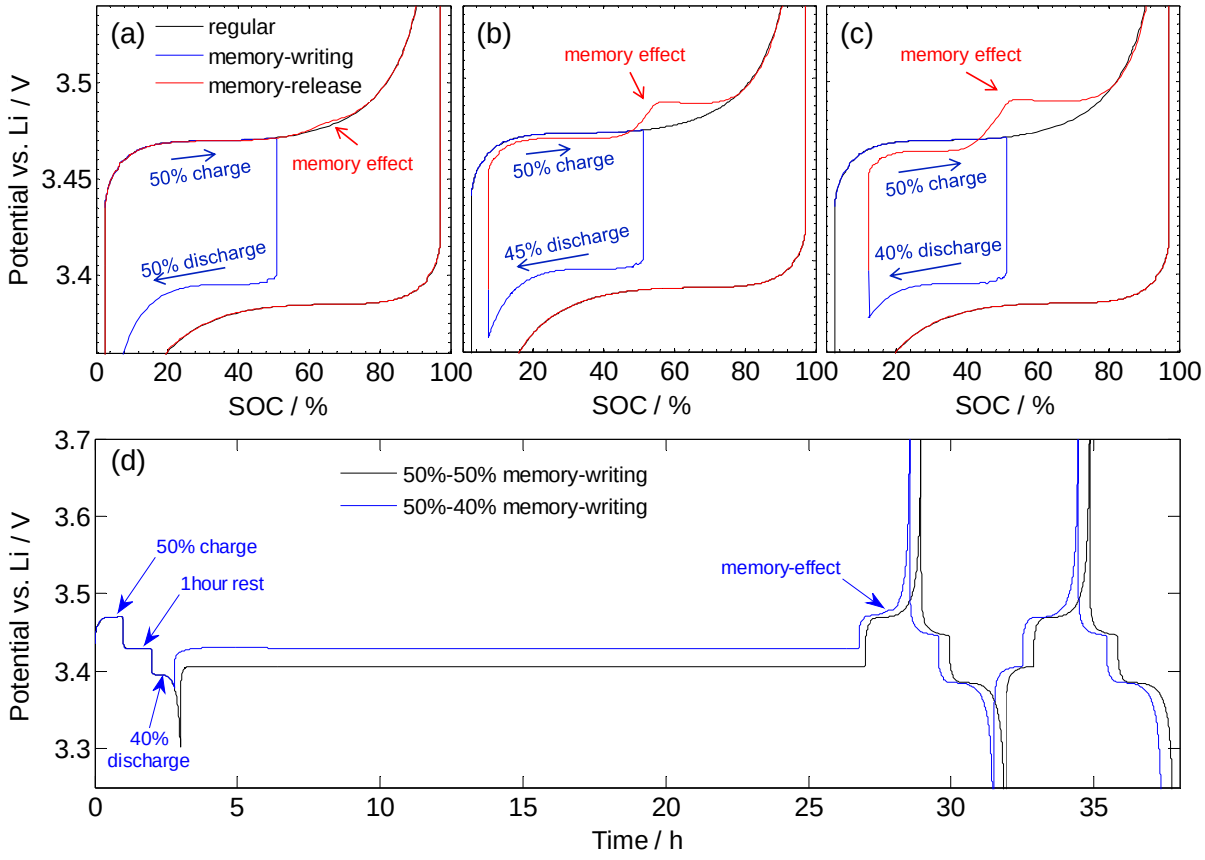

Figure 4-5. Memory effect during a charge following memory-writing cycles with 50% depth of charge and (a) 50%, (b) 45% and (c) 40% depths of discharge. (d) Effect of long relaxation time (24 h) after shallow (blue) and deep (black) memory-writing discharges. The rate during both memory-writing and memory-release cycles is C/2 with 10 minutes of ret time between the writing and release cycles, unless otherwise stated.

In order to gain further insight into the above observations, unit utilizations are plotted in Figure 4-6 at the outset and end of the steps constituting the memory-writing cycle for the selected experiments. Theoretically, a fully-discharged electrode would consist of elementary units with Li concentration equal to 1; in practice, however, this is not the case and the end-capacity deviates from the theoretical value as the applied current increases (e.g., C/2, the experimental condition used by Sasaki et al. [17]). Therefore, the initial concentration of Li in the units is set to be below 1 and within the Li-rich solid-solution region according to the single-unit equilibrium function. This also guarantees zero inter-unit exchange of species and initial stability of the electrode. Although not included here, simulations with zero initial state-of-charge did not generate any memory effect for a perfectly balanced memory-writing cycle. At the same time, the results in Figure 4-5 show that the memory effect becomes more pronounced as the memory-writing cycle becomes more imbalanced. Taken together, these findings indicate that a necessary condition for the memory effect to appear in an LFP electrode is the existence of a non-zero residual capacity at the onset of memory-release charging which may originate either from a non-zero initial SOC or from an imbalanced writing cycle. A memory effect should therefore not be observed in an electrode that has been preconditioned at extremely low currents (i.e., zero initial SOC) and has undergone an extremely slow memory-writing cycle (i.e., approaching a balanced cycle).

The uniform Li content initially set for all units evolves during the memory-writing charge according to the resistivity of the units until the electrode reaches its assigned depth of charge (stage labeled A in Figure 4-6a-f). The next rest period leads to a redistribution of Li among the units which may or may not reach their most stable state depending on the relaxation time (stage B). The subsequent discharge transforms both stable delithiated (least-limiting trail) and the partially-delithiated (thermodynamically unstable) units to the Li-rich phase generating an unusual utilization profile even when the electrode reaches the same initial SOC (stage C). The initial residual capacity (i.e., Li deficiency $\Delta y_k = 0.025$, $k = 1, 2, \ldots, N$) is redistributed and localized as a depression in the profile over a certain fraction of units (bins 26 to 39, Stage C in Figure 4-6a-c) while other units are fully lithiated. Needless to say, a larger residual capacity leads to a wider and deeper depression in the bin utilization curves as shown in Figure 4-6e-f. Finally, the rest period preceding the memory-release cycle enables the units to relax to a more stable condition by exchanging their Li content with each other (stage D). The localized residual capacity at the outset of the memory-release cycle (i.e., stage D) is responsible for the occurrence of the memory effect. The memory effect is boosted by enlarging the accumulated residual capacity (Figure 4-5a-c) or diminished by easing the utilization non-

uniformity. Figure 4-6a-c show the distributions of bin utilization after 3 different rest periods (1 min, 10 min and 1 h, respectively) between the writing and release cycles corresponding to the results shown in Figure 4-4e. The utilization depression clearly diminishes by increasing the relaxation time from 1 min to 1 h in agreement with the disappearance of the memory potential-bump in Figure 4-4e.

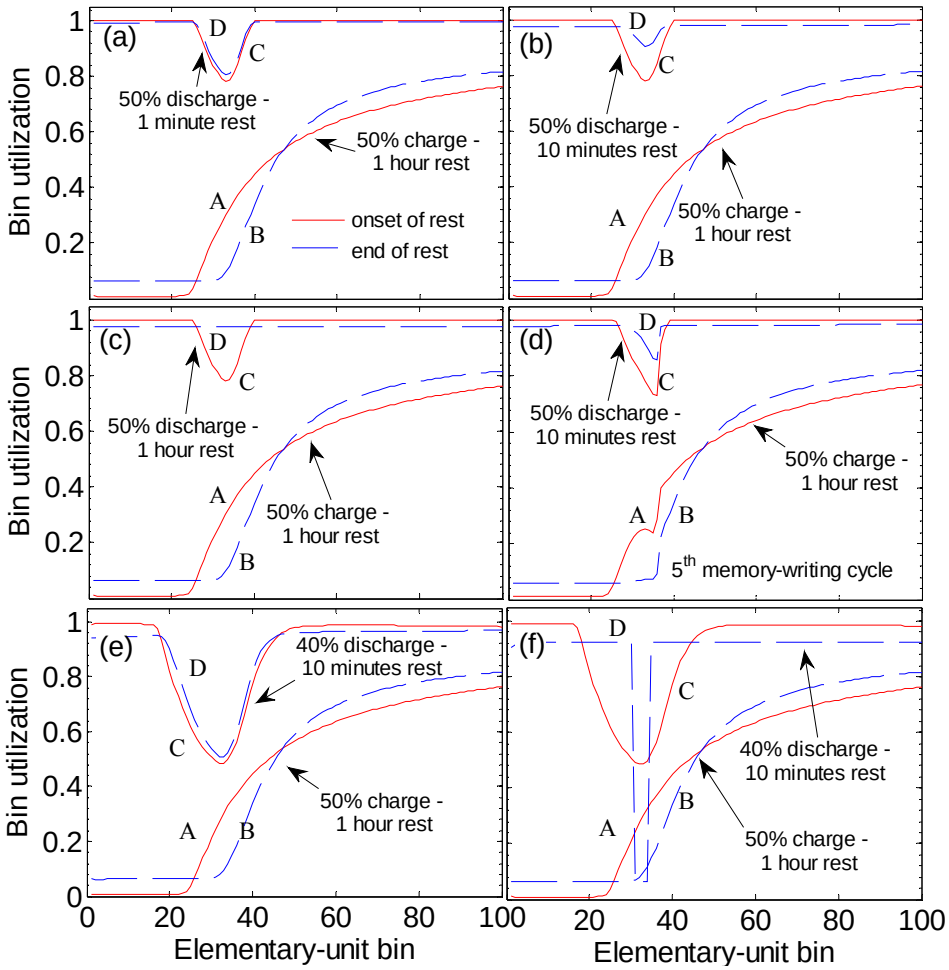

Figure 4-6. Utilization of elementary-unit bins at the outset and end of relaxations during the memory-writing cycle for the following 6 different sequences: (a) 50% charge, 1 h rest, 50% discharge, 1 min rest, (b) 50% charge, 1 h rest, 50% discharge, 10 min rest, (c) 50% charge,1 h rest, 50% discharge, 1 h rest, (d) 5 cycles of 50% charge, 1 h rest, 50% discharge, 10 min rest, (e) 50% charge, 1 h rest, 40% discharge, 10 min rest and (f) 50% charge, 1 h rest, 40% discharge, 24 h rest.

If the applied current is set to zero and Eq. (4-2) is substituted into Eq. (4-4), the following expression for the relaxing potential is obtained:

$$\Phi = \frac{\sum_{k=1}^{N} U_k(y_k)\frac{1}{R_k^{'}}}{\frac{1}{R_{eq}}}, \tag{4-6}$$

where $R_k^{'} = R_k / \varepsilon_k$ and $R_{eq} = \left(\sum_{k=1}^{N} 1/R_k^{'} \right)^{-1}$ are the resistance of each bin and the equivalent resistance of the electrode, respectively. Based on this expression, one concludes that, given a long enough rest period, the electrode potential Φ approaches a common single-unit equilibrium potential $\overline{U(y_k)}$ for all units which may or may not correspond to a common unit utilization. For an overall electrode utilization located within the sloping branches of the electrode potential profile, a common equilibrium potential is realized only when all units share an identical Li concentration (stage D in Figure 4-6c). However, if the electrode utilization is within the biphasic region, an adequate rest time causes the elementary units to segregate into two groups with an identical equilibrium potential but different Li concentrations, i.e., Li-rich and Li-poor phases. Our simulations show that the equilibrium potential of the electrode ensemble is bounded within the quasi-static potential hysteresis but is not unique for a given utilization depending on the history of the electrode. Accordingly, the exact concentrations of Li in the two phases vary slightly. On account of a non-uniform resistance, the previous history of the electrode dictates the configuration of the two phases among the units. For instance, less resistive units constitute the Li-poor phase and more resistive ones make up the Li-rich phase during a partial charge. On the other hand, after an imbalanced memory-writing cycle, the bin utilization depression grows into a gap where bins with intermediate resistivity exhibit little utilization (i.e., Li-poor phase) during the relaxation (stage D in Figure 4-6f). This explains why the memory effect is not removed in Figure 4-5d even after a long relaxation period. Moreover, the modification of the memory effect with repetition of the same memory-writing cycle (Figure 4-4f) originates from the utilization anomaly being reduced to the narrow range shown in Figure 4-6d.

In order to highlight the influence of the charge/discharge history on the electrode performance, a simple path-dependence simulation is performed in accordance with the previous experiments described in Ref. [59]. Starting from a fully discharged state, the electrode is charged for

12.5 hours at a current density corresponding to C/25 to raise its SOC to 50%. This is followed by a 2-hour rest period after which the electrode is charged (or discharged) at 1C to 4 V (2.8 V). The same procedure is repeated in the opposite direction starting from a fully charged state; the electrode is discharged to 50% SOC over 12.5 hours at C/25 and then rested for 2 hours after which 1C discharge (or charge) current is applied until a voltage 2.8 V (4 V) is attained. Both the electrode potential and capacity differ depending on the path taken to reach the end of the charge (or discharge). The simulation results presented in Figure 4-7 agree well with the trends observed experimentally and can be explained through the same reasoning discussed above for the memory effect simulations [13, 59].

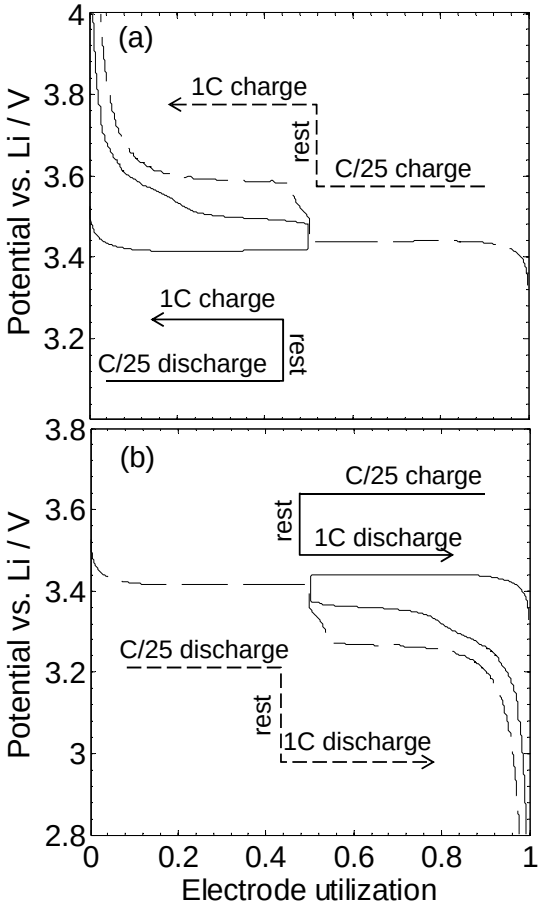

Figure 4-7. Path dependence during (a) fully charging of electrode at 1C after being brought to 50% SOC at C/25 via different paths (charging from 0% SOC (dashed line) and discharging from 100% SOC (solid line)) and 2-h rests and (b) discharge obtained by mirroring the operating conditions in (a).

An alternating sequence of constant-current and open-circuit steps constitutes the galvanostatic intermittent titration technique [156], which is a useful method regularly employed by battery researchers to estimate the chemical diffusion coefficient of guest species in insertion materials. One distinct feature of an LFP electrode, as suggested by Sasaki et al. [17], is the polarization overshoot of the applied GITT pulses compared to a continuous galvanostatic potential profile at the same current. In other words, the intermittent relaxations during the GITT pulses modify the system so as to impede the electrode response toward the subsequent pulse current. The simulations of approximate solid-solution models such as those developed in Chapter 3 have not been able to show this feature. Conventional bulk phase-change models may describe it by minimizing the two-phase interface and coherency strain energies during the rest period and re-triggering the nucleation and growth process during the subsequent current pulse. The many-unit approach, on the other hand, effectively captures the GITT polarization overshoot (Figure 4-8a) by allowing unstable activated units to reach their most energetically favorable configuration during intermittent rest periods, i.e., either Li-rich or Li-poor phase. Considering a GITT discharge process for instance, the absence of unstable partially-lithiated units in a relaxed partially discharged electrode (i.e., as opposed to an electrode at the same SOC under a continuous discharge operation) leads to a smaller number of available units (with high resistance) having to sustain the following pulse at the same current. Since this makes it more difficult for charge transfer to occur, the electrode reaches successively higher overpotentials during the subsequent pulses towards the end of the discharge.

The potentiostatic intermittent titration technique (PITT) is another electroanalytical method widely used for determining transport as well as thermodynamic properties of electrochemical materials [157]. A “staircase” voltage profile with a certain successive decrement (increment) between the upper (lower) and lower (upper) cut-off potentials is applied and the current decay with time is recorded for each potential step. Each individual titration is terminated when the absolute current reaches a preset minimum value. This technique is of interest for investigating phase-change materials since it helps reveal possible phase-transformation mechanisms from the observed transient current (e.g., KJMA analysis). More specifically, the bell-shaped current response of an LFP electrode over intermediate SOCs is commonly interpreted to arise from the nucleation and growth of the second phase [15, 98, 99, 148] in contrast with the Cottrell-type current response which is indicative of a diffusion-limited insertion process. However, as shown in Figure 4-8b, the proposed model is able to predict the appearance of a current hump in the chronoamperogram although it does not include the nucleation and growth of a second phase. Thus, an alternative explanation for the

current hump that emerges from our model is the non-equilibrium lithiation of single units and statistical distributions of physical properties that limit the charge transfer rate in a phase-change porous electrode rather than commonly accepted phase-change mechanisms such as nucleation and growth.

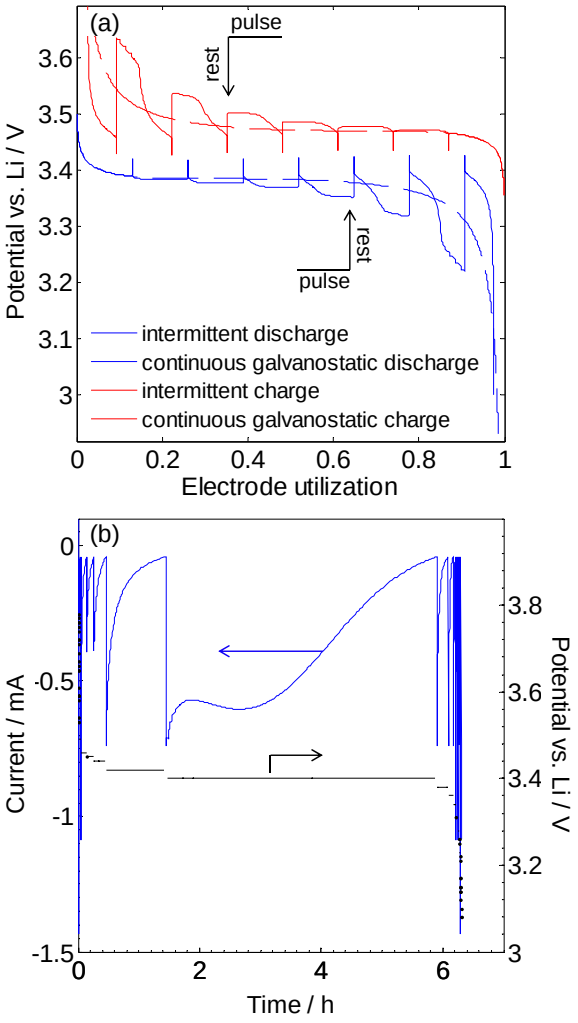

Figure 4-8. (a) GITT charge and discharge (solid line) simulated by applying C/2 pulses for 16 min followed by 2 h rest. The continuous galvanostatic charge and discharge curves at C/2 (dashed lines) are included for comparison. (b) PITT discharge simulated by applying the staircase potential profile with a 10 mV decrement from 3.8 to 3.0 V versus Li reference electrode. Each titration is terminated when the absolute current reaches C/50.

The analyses presented in this chapter help explain the experimental observations [73-76, 81, 158] of the collective lithiation of discrete units in a porous LFP electrode. The model presented here has been evaluated under various operating modes including continuous/intermittent partial/full galvanostatic and potentiostatic cycles. Overall, the results suggest that interactions among many interconnected insertion units (e.g., $LiFePO_4$) play a dominant role in the electrochemical performance of the phase-change electrode and should form the framework for a prospective comprehensive model. It is important to emphasize that the analysis in this chapter has been intended for demonstration purposes only. Complications at both unit (e.g., charge-transfer kinetics and solid-phase electronic/ionic transport within and at the surrounding of each unit) and electrode (e.g., porous-electrode effects) scales are acknowledged and should be included in such a comprehensive model for more quantitative simulations.

4.4 Conclusion

In this chapter, we have presented a simple mathematical model for the dynamics of phase-transforming porous electrodes applied to $LiFePO_4$. The model features a non-equilibrium solid-solution pathway for Li insertion/de-insertion into and a Gaussian distribution of resistances among channels/crystallites/nanoparticles constituting total active material loading in a porous electrode. It assumes rapid (but energetically expensive) transport of species inside each individual unit and an inherent distribution of physico-chemical properties of the material in an ensemble of many electronically and ionically wired units. With only these two factors involved, our model can simultaneously explain a number of unusual qualities associated with lithium iron phosphate electrochemical performance including the quasi-static potential hysteresis, high rate capability, cycle-path dependence, larger electrode polarization in GITT compared with that observed during a continuous cycling at the same current, bell-shaped current response in PITT and the most recently observed memory effect. The simplicity of the model, however, does not rule out the known complications at the unit and electrode levels but rather magnifies the significance of unit-to-unit interactions even at high currents and under combined operating modes which has been typically ignored in mathematical treatments of phase-change porous electrodes so far.

Chapter 5

Mesoscopic Modeling of $LiFePO_4$ Electrodes: Experimental Validation Under Continuous and Intermittent Operation Modes

The following chapter is based on the work to be submitted by M. Farkhondeh, M. Pritzker, M. Fowler and C. Delacourt, entitled:

"Mesoscopic Modeling of $LiFePO_4$ Electrodes: Experimental Validation under Continuous and Intermittent Operation Modes"

This thesis author's specific contribution to this paper was to design and conduct experiments, develop the model, conduct simulations, prepare all the graphics and results, prepare the manuscript with direction from the project advisors who were co-authors. All authors reviewed the manuscript.

5.1 Introduction

It has been discussed in the previous chapters that core-shell-type [57, 101] and non-ideal solid-solution [16, 100] models could be used to describe the juxtaposition of the two phases in a single particle observed during chemical lithiation/delithiation. However, in most cases they fail to provide an accurate physical picture of the process (i.e., filling of *b* channels in the *Pnma* space group of olivine crystal structure and the many-particle effects) [67, 68, 124]. Moreover, although frequently used in the literature to simulate the electrochemical performance of LFP electrodes, these models are either impractical or unable to predict the electrode performance beyond continuous galvanostatic operating conditions.

Inspired by Dreyer's many-particle model [14, 83], we have developed a simple mesoscopic model in Chapter 4 that disregards the choice of inter- versus intra-particle phase-transformation mechanisms. In addition to the potential plateau, quasi-static hysteresis, high rate capability and rate-dependent lithiation/delithiation dynamics of LFP electrodes, the model was able to qualitatively predict other peculiar behavior of LFP electrodes including cycle-path dependence [13, 59], mismatch of electrode polarization in GITT compared with continuous cycling at the same rate [16, 17], bell-shaped current response in PITT [15] and the memory effect [17].

In this chapter, the mesoscopic model developed in Chapter 4 is embedded into porous-electrode theory and is validated by comparing the simulation results to experimental discharge data under various continuous/intermittent operating conditions.

5.2 Experimental

The LFP electrode used in this study was fabricated from a commercial lithium-ion pouch cell (20 Ah nominal capacity) patterned for plug-in hybrid electric (PHEV) and electric (EV) vehicle applications. The pouch cell was first discharged at C/10 down to 2.0 V and held at that voltage until the current decayed to C/50.

The discharged cell was then dismantled in an argon-filled glove box (<1 ppm H_2O, <1 ppm O_2) and the double-side coated cathode sheets were recovered. In order to perform electrochemical experiments, the coating on one side of the electrode sheet was removed by gently rubbing it with a cotton-based wipe soaked in 1-methyl-2-pyrrolidone (NMP). The resulting one-side electrode sheet was subsequently rinsed with anhydrous dimethyl carbonate (DMC) in order to remove any remainder of the electrolyte salt in the porous electrode. Circular disks of LFP electrodes were then punched inside the glove box using a 10.5 mm diameter puncher.

Coin cells (CR2032) were assembled using the punched LFP electrodes as the working electrode, 12.7 mm lithium metal discs as the reference/counter electrode and Celgard 2500 polypropylene membrane as the separator between the working and reference/counter electrodes. A 1 mol L^{-1} solution of $LiPF_6$ in ethylene carbonate (EC) and dimethyl carbonate (1:1 vol.) was used as the electrolyte and added to the electrode and separator prior to sealing the cells. The assembled coin cells then underwent a series of continuous and intermittent galvanostatic charge/discharge experiments using a multi-channel potentiostat/galvanostat (VSP, Bio-Logic, France). The cells were maintained at 25°C in a temperature chamber (Cincinnati Sub-Zero MCB-1.2, USA) throughout the cycling experiments. Prior to the main experiments, the cells were first conditioned at 25°C using the following procedure. They were first charged at C/2 (1C rate is equivalent to 1.38 mA cm^{-2} of applied current) up to 4.2 V followed by a constant-voltage step until the current response decayed to C/50. After a resting period of 2 hours, the electrode was discharged at the same rate down to 2.5 V followed by another constant-voltage step at 2.5 V until the discharge current reached the same cut-off value of C/50. This conditioning procedure was repeated so that a total of 5 of these charge-discharge cycles between 2.5 V and 4.2 V were conducted prior to the main experiments.

Rate-capability tests were carried out according to the following charge and discharge sequence: i) galvanostatic charge at a specified C-rate until the electrode potential reached the upper cut-off value, ii) charge at constant voltage until the current reached C/50, iii) 2-hour relaxation period, iv) discharge at the same rate as that in step i) until the electrode potential reached the lower cut-off potential, v) discharge at constant-voltage until the current reached C/50, and vi) 2-hour relaxation period.

The galvanostatic intermittent titration technique was applied to the LFP electrode starting from a fully charged state. The GITT waveforms for each of these experiments consisted of a 2-min (or 6-min) galvanostatic discharge pulse at 1C followed by 2-hour (or 15-min) relaxation period applied repeatedly to the electrode until the lower cut-off potential was reached. Depending on the durations of the discharge pulse and the subsequent relaxation period, three different conditions were applied to an electrode. These three GITT experiments are referred to as "2min P-2h R", "2min P-15min R" and "6min P-2h R" throughout this chapter for brevity ("P" stands for current pulse and "R" stands for relaxation period).

The electrode thickness was measured using a P-6 Stylus Profiler (KLA-Tencor, USA). A four-probe setup (C4S 67/1, Cascade Microtech Inc., USA) and a precision multi-meter (Keithley 2440 5A, Tektronix, USA) were used to measure the effective electronic conductivity of the LFP electrodes delaminated from the aluminum substrate. Conductivity measurements of a 2-layer aluminum/porous electrode medium are prone to large error due to the significant difference between the conductivity of aluminum and the porous composite electrode and due to the presence of a non-zero contact resistance between these layers. Consequently, the aluminum current collector was de-bonded from the porous-electrode layer prior to the conductivity measurements by immersing the aluminum/electrode samples in a 1 $\mathrm{mol\ L^{-1}}$ aqueous solution of NaOH for a short period of time (1 to 3 minutes). The delaminated electrode was then rinsed with deionized water to remove the remainder of the solute and any the reaction products before being dried on a glass slide at room temperature. The conductivity measurements were conducted at 5 different currents within the range of 0.1 mA to 1 mA each replicated 4 times.

5.3 Model Development

In order to simulate the performance of an actual LFP electrode, the previously proposed mesoscopic model is used to describe the many-unit interactions in the electrode. Model parameters including the

equilibrium potential and resistance distribution are different from those used in Chapter 4 as detailed later in this section. The model is embedded into porous-electrode theory to give a more realistic account of the electrode performance under various operating conditions.

The model assumes that the elementary lithiating/delithiating units exist in a non-equilibrium condition which, despite the biphasic nature of the material at equilibrium, accommodate a single solid-solution phase throughout the lithiation/delithiation process. As such, the model assumes that the chemical potential of Li in each unit is a non-monotonic function of composition. The elementary units in the model are meso-scale domains which are large enough to contain substantial number of reaction sites (i.e., vacancies and inserted species), but small enough so that no intra-unit phase separation occurs.

The proposed mesoscopic model is supported by the experimental observation of collective lithiation/delithiation of nano particles in an LFP electrode [11, 12, 74-76, 81, 82]; in this situation, LFP nano particles can be considered as the elementary units. Our mesoscopic physical representation is also in line with high-resolution transmission-electron-microscopy observations of chemically delithiated LFP particles where a large amount of microstructural defects partition the pristine particles (i.e., if not nano sized) into small meso-scale domains [77-80]. Maier et al. [77] hypothesized that mechanical damages associated with many electrochemical lithiation/delithiation cycles continually change the pristine microstructure by forming smaller, more mechanically stable active domains until an optimum microstructure is reached. In this case, the mechanically stable domains constitute a collection of interconnected elementary units as described above. In other words, the active material microstructure evolves to the most energetically favorable state, although never in perfect equilibrium, whereby the co-existence of Li-rich and Li-poor phases in each individual meso-scale domain is completely suppressed [77, 159, 160].

The model presented here assumes a mechanically stable, well-evolved microstructure. The evolution of electrode microstructure under cycling is beyond the scope of this thesis work and deserves separate comprehensive analysis.

A distribution of reaction resistance is assumed to exist among the LFP. This assumption is justified on the basis of the extremely low electronic conductivity ($10^{-7}\,\mathrm{S\,m^{-1}}$) that requires the application of conductive coatings onto the active particles, as well as the one-dimensional (i.e., [0 1 0] direction) ionic conductivity of the material.

The model ignores solid-state diffusion inside LFP units following recent observations of ultrafast chemical [154] and electrochemical [10, 153] delithiation/lithiation of LFP units which counter the common belief that intra-particle mass transport is a limiting factor for Li insertion/de-insertion into/from the units. With this view, the geometrical description of LFP units becomes irrelevant as far as the diffusion length is concerned.

The change of the dimensionless Li concentration y_k in the k^{th} elementary unit with time is related to the partial current i_k (in A mol^{-1}) of that unit according to:

$$i_k = -F\frac{dy_k}{dt} \tag{5-1}$$

where F is the Faraday constant and t is time. Ohm's law describes the local potential loss associated with the insertion/de-insertion of Li into/from each unit:

$$\eta_k = R_k i_k \tag{5-2}$$

where η_k is the insertion/de-insertion reaction overpotential and relates to the electric potential of electrode Φ_1 and electrolyte Φ_2 according to:

$$\eta_k = \Phi_1 - \Phi_2 - U_k \tag{5-3}$$

where U_k is the equilibrium potential of elementary unit k and is a non-monotonic function of y_k. In the simplest approximation, the regular solution model (one-parameter Margules model) may be used to describe the thermodynamic state of each unit [109]. However, this model turns out to be too simple to capture the actual single-unit thermodynamic behavior of elementary units, which is key for a realistic simulation of the charge/discharge dynamics of an LFP electrode. Alternatively, a modified two-parameter Margules model is assumed here, which gives a more sophisticated thermodynamic description of LFP units by permitting an asymmetric dependence of the excess free energy of the binary solution (i.e., solution of the inserted species and empty sites) on composition:

$$\begin{aligned} U_k = U^0 + \frac{RT}{F}\ln\left(\frac{1-y_k}{y_k}\right) \\ + \frac{RT}{F}\Big(A_1(2y_k-1) \\ + A_2\left(3y_k - \frac{3}{2}y_k^2 - 1\right) + B(2y_k-1)^C\Big) \end{aligned} \tag{5-4}$$

U^0 is the standard equilibrium potential R is the gas constant, T is temperature and A_1 and A_2 are the Margules parameters. The last term in Eq. (5-4) is inspired by the Redlich-Kister expansion [131] and is included in the model to capture non-idealities of the Li-poor and Li-rich solid-solution end-members (i.e., when $y_k \to 0$ or $y_k \to 1$). It assures a well-defined equilibrium potential of LFP within the potential window of ~ 2 V to ~ 4.5V vs. Li reference electrode. Setting $A_2 = 0$ and $B = 0$ gives the regular solution model (i.e., one-parameter Margules).

The elementary unit resistances are assumed to be described by a bimodal distribution composed of a mixture of two log-normal functions:

$$\varepsilon_k = \frac{fP_1(R_k) + (1-f)P_2(R_k)}{\sum_{k=1}^{N}\left(fP_1(R_k) + (1-f)P_2(R_k)\right)} \tag{5-5}$$

where ε_k is the volume fraction of elementary unit k with respect to the total active material volume fraction ($\sum_k \varepsilon_k = 1$). $P_m(R_k)$ is the probability density function of R_k ($R_k > 0$):

$$P_m(R_k) = \frac{1}{R_k \sigma_m \sqrt{2\pi}} \exp\left(-\frac{\ln R_k - \mu_m}{2\sigma_m^2}\right) \tag{5-6}$$

and f is the mixing parameter. μ_m and σ_m are the mean and standard deviation of the associated normal distribution (i.e., $\ln R_k$). Subscript m indicates the individual log-normal distributions. As will be discussed in section 5.4.3, we obtained better results when the elementary unit resistances were described in terms of a bimodal distribution than a unimodal distribution.

The governing equations at the electrode level and the associated boundary conditions are adapted from the well-developed porous-electrode theory [123] and summarized in Table 5-1. Note that electrolyte transport equations are derived from Stefan-Maxwell equations [107]. The solvent velocity is chosen as the reference and set to zero (i.e., no convection) for the sake of simplicity.

The system of the governing equations (Table 5-1) is numerically solved by means of the finite-element-based COMSOL Multiphysics simulation package. The dimensionless cathode and separator thickness are each discretized into 50 and 10 equal intervals, respectively. The total active material loading is discretized into 40 elementary-unit bins. For the GITT simulations, 100 unit bins are considered. The solver is supervised in MATLAB using COMSOL LiveLink™ for MATLAB.

Table 5-1. Summary of the governing equations and the corresponding boundary conditions used for Li/LFP half-cell simulations.

Governing equations at the unit level	
$i_k = -F\frac{dy_k}{dt}$	
$\eta_k = R_k i_k$	
$\eta_k = \Phi_1 - \Phi_2 - U_k$	
$U_k = U^0 + \frac{RT}{F}\ln\left(\frac{1-y_k}{y_k}\right) + \frac{RT}{F}\left(A_1(2y_k-1) + A_2\left(3y_k - \frac{3}{2}y_k^2 - 1\right) + B(2y_k-1)^C\right)$	
$\varepsilon_k = \frac{fP_1(R_k) + (1-f)P_2(R_k)}{\sum_{k=1}^{N}\left(fP_1(R_k) + (1-f)P_2(R_k)\right)}$	
$P_m(R_k) = \frac{1}{R_k\sigma_m\sqrt{2\pi}}\exp\left(-\frac{\ln R_k - \mu_m}{2\sigma_m^2}\right)$	
Governing equations at electrode level	
Cathode equations	**Boundary conditions**
$\nabla\cdot\mathbf{i}_2 = c_{\max}\varepsilon_t\sum_k \varepsilon_k i_k$	continuity at $x = l_{\text{sep}}$ and $\mathbf{i}_2\vert_{x=l_{\text{sep}}+l_{\text{cat}}} = 0$
$\mathbf{i}_2 = -\kappa_{\text{eff,cat}}\left(\nabla\Phi_2 - \frac{2RT(1-t_+^0)}{F}\alpha\nabla\ln c\right)$	
$\kappa_{\text{eff,cat}} = \xi_{\text{cat}}\varepsilon_{\text{cat}}^{\gamma_{\text{cat}}}\kappa$	
$\nabla\cdot(\mathbf{i}_1 + \mathbf{i}_2) = 0$	$\mathbf{i}_1\vert_{x=l_{\text{sep}}} = 0$ and $\mathbf{i}_1\vert_{x=l_{\text{sep}}+l_{\text{cat}}} = I$
$\mathbf{i}_1 = -\sigma_{\text{eff}}\nabla\Phi_1$	
$\varepsilon_{\text{cat}}\frac{\partial c}{\partial t} = \nabla\cdot\left(D_{\text{eff,cat}}\nabla c\right) - \frac{\mathbf{i}_2\cdot\nabla t_+^0}{F} + \frac{(1-t_+^0)}{F}c_{\max}\varepsilon_t\sum_k\varepsilon_k i_k$	continuity at $x = l_{\text{sep}}$ and $\nabla c\vert_{x=l_{\text{sep}}+l_{\text{cat}}} = 0$
$D_{\text{eff,cat}} = \xi_{\text{cat}}\varepsilon_{\text{cat}}^{\gamma_{\text{cat}}}D$	
Separator equations	**Boundary conditions**
$\nabla\cdot\mathbf{i}_2 = 0$	$\Phi_2\vert_{x=0} = 0$ and continuity at $x = l_{\text{sep}}$

$$\mathbf{i}_2 = -\kappa_{\text{eff,sep}}\left(\nabla\Phi_2 - \frac{2RT(1-t_+^0)}{F}\alpha\nabla\ln c\right)$$

$$\kappa_{\text{eff,sep}} = \xi_{\text{sep}}\varepsilon_{\text{sep}}^{\gamma_{\text{sep}}}\kappa$$

$$\varepsilon_{\text{sep}}\frac{\partial c}{\partial t} = \nabla\cdot\left(D_{\text{eff,sep}}\nabla c\right) - \frac{\mathbf{i}_2\cdot\nabla t_+^0}{F} \qquad \nabla c|_{x=0} = -\frac{I(1-t_+^0)}{FD_{\text{eff,sep}}}\ and\ \text{continuity at}\ x = l_{\text{sep}}$$

$$D_{\text{eff,sep}} = \xi_{\text{sep}}\varepsilon_{\text{sep}}^{\gamma_{\text{sep}}}D$$

Li foil counter electrode

$$I = F\varepsilon_{\text{sep}}k_{\text{Li}}^0 c^{1-\beta_{\text{Li}}}\left[\exp\left(\frac{(1-\beta_{\text{Li}})F}{RT}(\Phi_{\text{Li}}-\Phi_2)\right) - \exp\left(-\frac{\beta_{\text{Li}}F}{RT}(\Phi_{\text{Li}}-\Phi_2)\right)\right]$$

5.4 Results and Discussion

The model is used to analyze experimental data obtained during various continuous and intermittent galvanostatic discharges of a commercial LFP electrode. The model parameters listed in Table 5-2 have been measured, fitted, assumed or taken from the literature. The electrode capacity is estimated to be ~1.22 mAh by averaging the electrode capacity at the end of constant-current-constant-voltage charges at different rates from C/50 to 3C. Given the geometric area and thickness of the electrode, LFP density and assuming a nominal capacity of ~170 mAh g^{-1}, the total volume fraction of LFP is estimated to be ~ 0.39. Assuming ~10 vol.% of the electrode is filled with binder and conductive material in the LFP electrode [161], the porosity of the LFP electrode is then calculated to be ~ 0.51. The rate constant for the electrochemical reaction at the surface of the Li foil has been measured using Li/Li symmetric cells as reported in a previous study [162]. The transport and thermodynamic properties of the electrolyte including ionic conductivity, chemical diffusion coefficient, transference number and thermodynamic factor are taken from a separate study, presented in Chapter 6, where a novel four-electrode electrochemical cell [163] was used for the measurements [164]. The generalized Bruggeman formula corrects the bulk properties for tortuosity. The Bruggeman coefficient and exponent of the cathode are taken from Ref. [165] and those of the separator are set to values regularly used in the literature (i.e., $\xi_{\text{sep}} = 1$ and $\gamma_{\text{sep}} = 1.5$).

The effective electronic conductivity of the cathode is measured using the four-probe method (probe spacing of ~1.5 mm) to be $19.6 \pm 1.1\ \text{S m}^{-1}$ which indicates the existence of highly

conductive conduits across the electrode at the millimeter-scale but does not convey any information about the homogeneity of the percolation network at the scale of elementary units (meso-scale). Such a large effective conductivity would not cause significant ohmic loss during electrode operation if the percolation network were homogenous, as assumed in porous-electrode theory [100]. The resistance distribution in the proposed model accounts for the inhomogeneity of the percolation network at the meso-scale as discussed in section 5.4.2.

Table 5-2. List of model parameters used for simulations.

Parameter	Symbol	Value
Cathode thickness (μm)	l_{cat}	60^{m}
Separator thickness (μm)	l_{sep}	25 [166]
Cathode porosity	$\varepsilon_{\mathrm{cat}}$	0.51^{c}
Separator porosity	$\varepsilon_{\mathrm{sep}}$	0.55 [166]
Total active-material volume fraction	ε_t	0.39^{c}
Maximum solid-phase lithium concentration (mol m^{-3})	$c_{\max}$	22806^{a}
Li foil charge-transfer coefficient	β_{Li}	0.5^{a}
Standard equilibrium potential (V vs. Li)	U^0	3.423^{m}
First Margules parameter	A_1	1.15^{f}
Second Margules parameter	A_2	2.2^{f}
Coefficient of the high order term in Eq. (5-4)	B	40^{f}
Power of the high-order term in Eq. (5-4)	C	51^{f}
Mean of $\ln R_k$ for $m = 1$	μ_1	-6.54
Standard deviation of $\ln R_k$ for $m = 1$	σ_1	1.87
Mean of $\ln R_k$ for $m = 2$	μ_2	-2.24
Standard deviation of $\ln R_k$ for $m = 2$	σ_2	1.31
Mixing parameter for resistance distribution	f	0.8^{f}
Li foil reaction rate constant (mol$^{\beta_{\mathrm{Li}}}$ m^2 s^{-1})	k_{Li}^0	7×10^{-6} [162]
Initial electrolyte concentration (mol m^{-3})	c_{ini}	1000^{a}
Bulk chemical diffusion coefficient of electrolyte (m^2 s^{-1})	D	2.67×10^{-10} [164]
Li^+ transference number	t_+^0	0.425 [164]
Bulk ionic conductivity of electrolyte (S m^{-1})	κ	1.19 [164]

Thermodynamic factor of electrolyte	α	2.32 [164]
Effective electronic conductivity of cathode (S m^{-1})	σ_{eff}	19.6^{m}
Bruggeman exponent of cathode	γ_{cat}	1.53 [165]
Bruggeman coefficient of cathode	ξ_{cat}	0.55 [165]
Bruggeman exponent of separator	γ_{sep}	1.5^{a}
Bruggeman coefficient of separator	ξ_{sep}	1^{a}

[a]: assumed; [c]: calculated; [f]: fitted to the experimental data; [m]: measured.

The single-unit equilibrium potential (SEQ) and the resistance distribution (RD) are fitted by comparing the model with the experimental discharge data to be presented in the next sections. As will be shown, the resulting model parameters give satisfactory fits to all seven sets of continuous galvanostatic discharge and three sets of GITT potential-capacity and potential-time curves.

5.4.1 Single-Unit Equilibrium Potential

The single-unit equilibrium potential is a key model parameter which determines how each elementary unit interacts with others during electrode operation and especially during relaxation. It is a non-monotonic function of composition based on the assumption that an elementary unit is a single bi-stable phase. Despite its critical role, measurement of the SEQ has remained an unsolved problem to date. The SEQ determines the overall electrode potential during quasi-static operation (i.e., extremely low charge/discharge rates) where a thermodynamic potential hysteresis occurs but cannot be fully characterized by the quasi-static potential profile alone. Moreover, various factors, including particle size and shape (i.e., surface, interface and stress-strain energies), synthesis method, level of impurities and defects can influence the SEQ. These factors may lead to a non-uniform thermodynamic behavior among units making U_k even more intractable.

The regular solution model (or one-parameter Margules model) is usually assumed by researchers to represent the thermodynamic behavior of an elementary unit in an inter-connected many-unit ensemble. Featuring a single interaction parameter, the model assumes that the dissolved species (i.e., either Li atoms or vacancies) undergo symmetric pairwise interactions at all compositions so that the system excess free energy exhibits a symmetric dependence on composition. The two-parameter Margules model presents an extension to the regular solution model that can account for possible asymmetry in the composition dependence of the excess free energy of the solution [131]. It will be shown later that the choice of an asymmetric equilibrium potential leads to a better fit of the model to GITT data.

Despite its relative complexity, the two-parameter Margules model does not give a good match to the low-concentration and high-concentration branches of the quasi-static electrode potential. Therefore, a high-order Redlich-Kister-like term is added to the two-parameter Margules model which expands the upper and lower bounds of the equilibrium potential as the Li stoichiometry in LFP approaches zero and unity, respectively. As such, the single-unit equilibrium potential is well-defined within the potential window of LFP implied by the overall electrode potential. The resulting equation (Eq. (5-4)) is represented in Figure 5-1 for different values of the interaction parameters yielding a symmetric (red) or an asymmetric (gray) equilibrium potential curve. The interaction parameters A_1 and A_2 as well as the standard equilibrium potential U^0 were obtained by comparing the prediction of the model with the experimental quasi-static galvanostatic charge/discharge and GITT data (as discussed later). The asymmetric equilibrium potential used in this study is consistent with the asymmetric solid-solution ranges estimated by Kobayashi et al. [167] using GITT (12 min pulses at C/20 followed by 24 h rest) and show a greater Li solubility on the Li-rich branch.

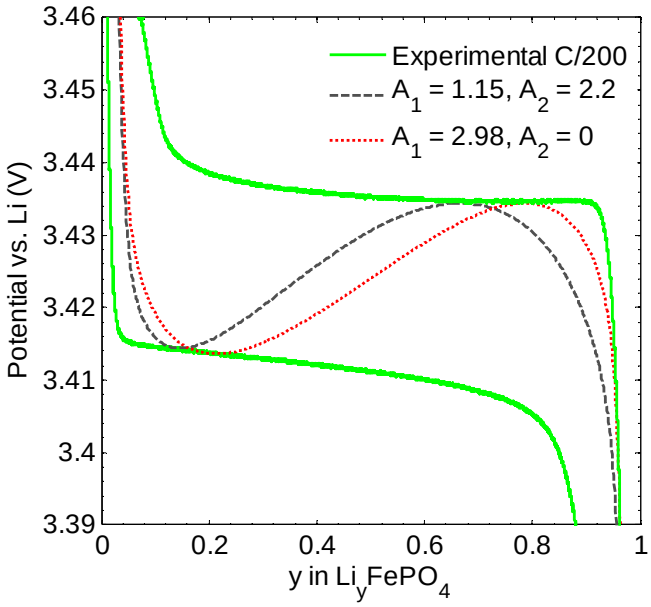

Figure 5-1. Comparison of single-unit equilibrium potential as a function of composition obtained using Eq. (5-4) with the experimental quasi-static electrode potential measured at a current of C/200. The asymmetric SEQ (black curve) is used for the simulations.

The parameters of the high-order term (i.e., B and C) are adjusted tentatively so as to increase the upper potential bound to ~ 4.5 V as $y_k \to 0$ and decrease the lower bound to ~ 2 V as $y_k \to 1$, but not alter the shape of the curve in the mid-stoichiometry range.

It should be emphasized that the potential does not level off to a perfectly flat plateau at intermediate stoichiometries in the experimental quasi-static curve (green) in Figure 5-1. It may actually stem from non-uniformities in the thermodynamic properties among the units (e.g., due to their size and shape) which end up affecting the numerical values of the model parameters such as A_1, A_2 and U^0. These effects, however, do not significantly affect the analysis presented here and are ignored for simplicity.

5.4.2 Elementary-Unit Resistance Distribution

LFP is an electronic insulator and can conduct Li ions in the [0 1 0] direction only. Consequently, it is commonly coated with carbon to improve the supply of electrons to the surface of the active material [50]. Non-carbonaceous iron-rich secondary phases (e.g., iron phosphide and iron phosphocarbide) formed *in-situ* by carbothermal synthesis of LFP also have been found to serve as efficient electronic conduits residing at the grain boundaries at the nano scale [51]. At the same time, *in-situ* formation of fast ion-conducting phases on the surface of crystallites was shown to dramatically improve the electrochemical performance of LFP. For example, this electrode could achieve 80% of its theoretical capacity at an applied current as high as 50C [10]. This improvement in electrode performance is explained by an increase in Li diffusion across the crystallite surface towards the (0 1 0) facet where the Li can be inserted. Moreover, it may be more realistic to consider the effect of the unit size in terms of the characteristic distance for surface diffusion rather than bulk diffusion in contrast with the common belief that bulk Li diffusion is limiting. Unit size also affects polarization associated with the charge-transfer reaction kinetics at the surface of active material. The solid/electrolyte interphase (SEI) layer on the surface of the active material may also affect (increase) resistance at the surface of LFP units. As a result, both ionic and electronic limitations of LFP at the unit level could be diminished by the presence of nano-scale auxiliary phases distributed onto lithiating/delithiating LFP units and by reducing the unit size itself.

At the electrode level, on the other hand, it is very difficult to achieve a homogeneous dispersion of conductive filler across the electrode [168]; the resulting non-uniform electronic percolation network has been shown to significantly degrade the rate performance of the electrode [161]. This could occur regardless of a possibly large effective conductivity of the composite electrode which is a macroscopic property that cannot reflect these non-homogeneities. The same is true for the electrolyte-filled network of pores which is responsible for the supply of Li to the surface of LFP [169, 170]. Porous-electrode theory is required to describe the essential features of solid-phase

and electrolyte-phase transport limitations. It is based on the superposition of the two phases and volume-averaging of the model quantities (i.e., physical properties and field variables). As a result, the theory is not able to resolve microstructural non-uniformities.

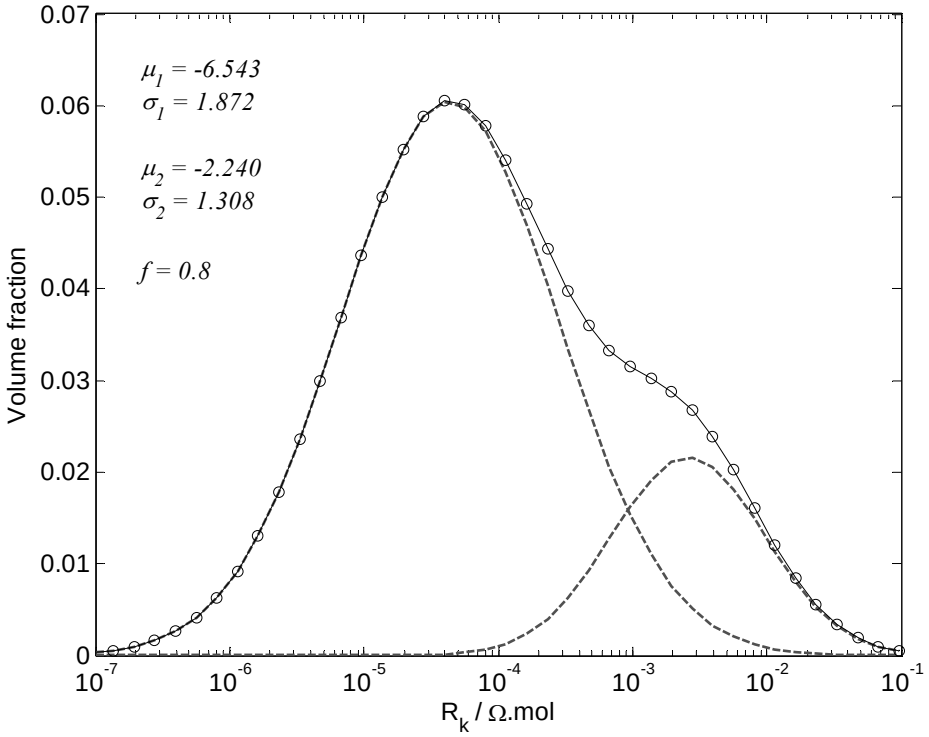

Figure 5-2. Bimodal resistance distribution used in the model.

An explicit accounting of non-uniformities of all of the physico-chemical properties as well as electronic/ionic environment of elementary LFP units, as described above, requires accurate knowledge of the electrode microstructure at high chemical and spatial resolution, which is difficult to obtain and is usually unavailable. Instead, the resistance distribution used in this model is meant to account for these effects, which greatly simplifies the model and reduces computation cost. The connection between lithiating/delithiating units in the electrode and their electronic/ionic environment can span from perfectly wired to completely detached. As such, the resistance of each unit may be very small (i.e., perfectly wired) or extremely large (i.e., completely isolated); it lumps effective resistances of different natures, which justifies the assumption of an extremely broad or even a bimodal log-normal resistance distribution.

5.4.3 Continuous Galvanostatic Discharge

The RD parameters have been obtained by comparing the experimental and model-computed data for the continuous galvanostatic discharge at C/10 and 2C. The fitted RD is plotted in Figure 5-2. Once this RD is obtained, its robustness has been assessed by using it to compute galvanostatic discharge curves at other applied currents from C/50 to 3C without any further adjustment of the parameters and then compare it to the corresponding experimental data. As shown in Figure 5-3, the agreement between the model predictions and measured data is very good over this wide range of currents. The effectiveness of the resistance distribution is evident in two ways: it allows the model to match the slanted behavior of the potential-capacity curves at intermediate potentials (Figure 5-3a) and predict the electrode utilization at the end of discharge at the various rates (Figure 5-3b).

It should be noted that the fitted bimodal RD may not be the only distribution that could work since other combinations of the distribution parameters could equally likely enable the model to satisfactorily fit the experimental data. Inclusion of more experimental data when fitting the model (i.e., more than C/10 and 2C) could not eliminate the extra degrees of freedom. This problem may not exist if a unimodal distribution with only two adjustable parameters could be used. Indeed, we tested a unimodal lognormal distribution but found that it could not satisfactorily fit the experimental data, i.e., although the slanted behavior at the mid-stoichiometry range could be fitted, it failed to capture the end-of-discharge capacities. Simulation results were made worse when the resistance was assumed to be purely due to charge-transfer reaction and its distribution was taken to correlate with a lognormal unit-size distribution (not shown here). In summary, the problem is over-constrained in the case of a unimodal lognormal distribution, but under-constrained in the case of a bimodal lognormal distribution. This could mean that either the model is too simple (e.g., neglecting microstructure) or a certain distribution other than lognormal can accurately represent the lumped resistances and fit the experimental data. Investigation of these two scenarios is beyond the scope of this work but is an important step to obtain a more accurate model.

Limitations at the end of discharge are usually attributed to solid-state diffusion. Previous model-experiment analysis of a commercial LFP electrode in Chapter 3 considered diffusion to be the determining factor at the end of discharge [100]; it yielded estimates for diffusivity on the order of $10^{-19}\,\mathrm{m^2\,s^{-1}}$. However, recent observations of fast chemical delithiation of sub-micron LFP particles suggest that solid-state diffusivities should be in the range of $\sim 10^{-13}$ to $10^{-15}\,\mathrm{m^2\,s^{-1}}$ [154] which are orders of magnitude greater than the earlier estimates and are in better harmony with

earlier first-principles calculations ($\sim 10^{-12}$ m^2 s^{-1}) [69, 155]. Ultrafast charge/discharge of optimized LFP electrodes also has confirmed fast Li mobility in the bulk of LFP [10, 153].

In order to assess a diffusion-limited scenario, the mesoscopic model was further elaborated to account for the intra-unit diffusion along with a unimodal lognormal RD. It turns out again that a very small diffusion coefficient in the order of 10^{-19} m^{2}s^{-1} (assuming spherical units with 80 nm radius) is required in order for solid-state transport limitations to become significant (simulation results not shown). Under this condition, solid-state diffusion limitations heavily suppress the unit-unit interactions induced by the non-monotonic SEQ which is at odds with experimental evidence of sequential or mixed sequential-parallel lithiation/delithiation of elementary units reported in the recent literature [11, 12, 74-76, 81, 82]. Accordingly, we decided to ignore intra-unit mass transport and apply the model presented in section 5.3 that includes a resistance distribution only. Further discussion of a diffusion-controlled scenario will be presented in a future work.

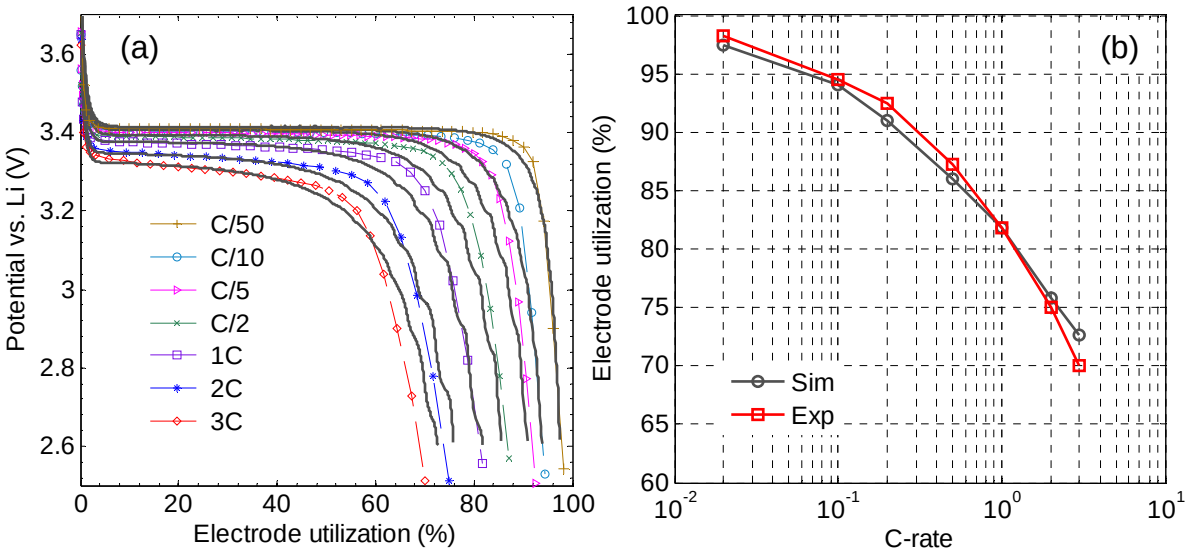

Figure 5-3. (a) Comparison of experimental galvanostatic discharge curves (markers) with the corresponding model-fitted curves (solid lines) at rates from C/50 to 3C. (b) Comparison of experimental and model-fitted end-of-discharge capacities at different C-rates. Model parameters are listed in Table 5-2.

The electrode polarization during discharge at 3C is broken down into its constituents and compared with the simulated quasi-static discharge (C/200, no RD included) in Figure 5-4. Based on the curve obtained by the model assuming zero resistances for the units (i.e., porous-electrode effects

only), it is evident that electrolyte transport limitations contribute significantly to the overall polarization of the electrode but does not limit the capacity at the end of discharge even at 3C. Inclusion of a unimodal RD (i.e., $f = 1$) in the model increases the potential loss but still overpredicts the end-of-discharge capacity. Only when a bimodal distribution is used to describe the unit resistance (i.e., with mixing parameter $f = 0.8$) is the model able to closely fit all of the experimental data including the end-capacity (black solid curve, also see Figure 5-3). It is clear from this analysis that the use of a bimodal distribution is required to capture the end-of-discharge capacities of the LFP electrode studied here. Of course, the model is yet to be validated by analyzing performance of other LFP electrodes with different formulations.

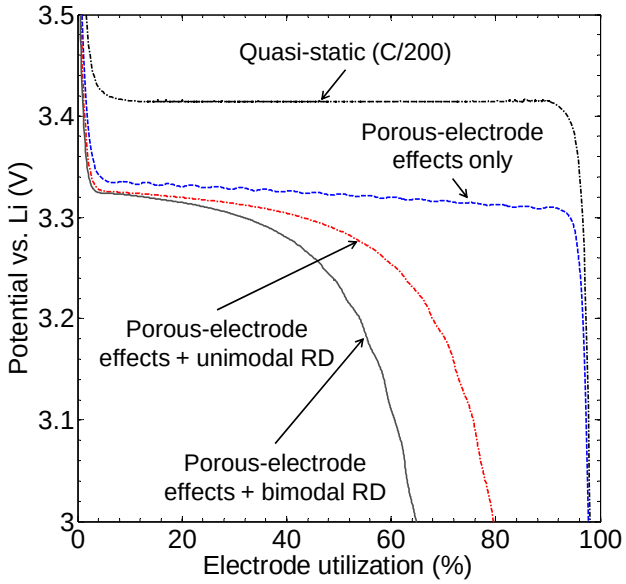

Figure 5-4. Contribution of different limiting phenomena to the overall potential drop at 3C compared with the simulated quasi-static electrode discharge profile at C/200 (RD not included). Model parameters are listed in Table 5-2.

The electrode dynamics during low-rate (C/10) and high-rate (3C) discharge are depicted in Figure 5-5 and Figure 5-6, respectively, in terms of a 3-dimensional plot relating the dimensionless Li concentration in the elementary units to the unit resistance and position within the electrode at three different depths of discharge (10%, 20% and 50%). The resistances are represented by intervals or bins in order from the least resistive ($\sim 10^{-7}$ Ω mol) to the most resistive ($\sim 10^{-1}$ Ω mol) one; color is coded from deep blue for fully delithiated to dark red for fully lithiated states. To gain a better

resolution in the results, simulations have been conducted by discretizing the electrode length into 50 segments.

As shown in Chapter 4, discharge can proceed with one unit being completely lithiated before the next unit reacts (i.e., unit-by-unit) or with more than one unit simultaneously undergoing lithiation (i.e., mixed sequential-parallel mechanism) depending on the applied current and depth of discharge. At the beginning of discharge, all units at a given location in the electrode lithiate simultaneously until they reach a stoichiometry corresponding to the lower spinodal limit of the SEQ where further insertion of Li pushes a small number of units (i.e., depending on their resistances) into the spinodal region. These "activated" units are in an unstable state and experience increasingly large driving forces (i.e., large η_k due the non-monotonic shape of U_k) which rapidly moves them to a stable state on the Li-rich branch of the SEQ. Since all units are electronically and ionically connected, they experience the same electric potential both in the solid Φ_1 and liquid Φ_2 phases at any position across the electrode.

As shown in Figure 5-5 and discussed previously in Chapter 4, elementary units mostly accommodate two states of lithiation at C/10; they are either in the Li-rich or Li-poor phase and only a few are active and undergoing lithiation at any instance during electrode discharge. The active units form a lithiation front that starts with units experiencing the smallest overpotential and propagates towards units with progressively larger overpotentials. The lithiation front separates Li-rich units from Li-poor ones resembling a diffuse boundary between the two phases. The width of the diffuse boundary is determined by the number of active units. Lithiation begins with the least resistive units located close to the separator (diagonal contour curves in Figure 5-5a) and continues to become more dispersed across the electrode (Figure 5-5b) until it finally spreads almost uniformly throughout the electrode but still confined to certain elementary units according their resistances (contour curves nearly perpendicular to the "elementary-unit bin" axis in Figure 5-5c). In other words, the lithiation front fades out at the electrode level when the variation of resistances among elementary units at any location within the electrode is greater than the variation of their ionic/electronic environment across the electrode.

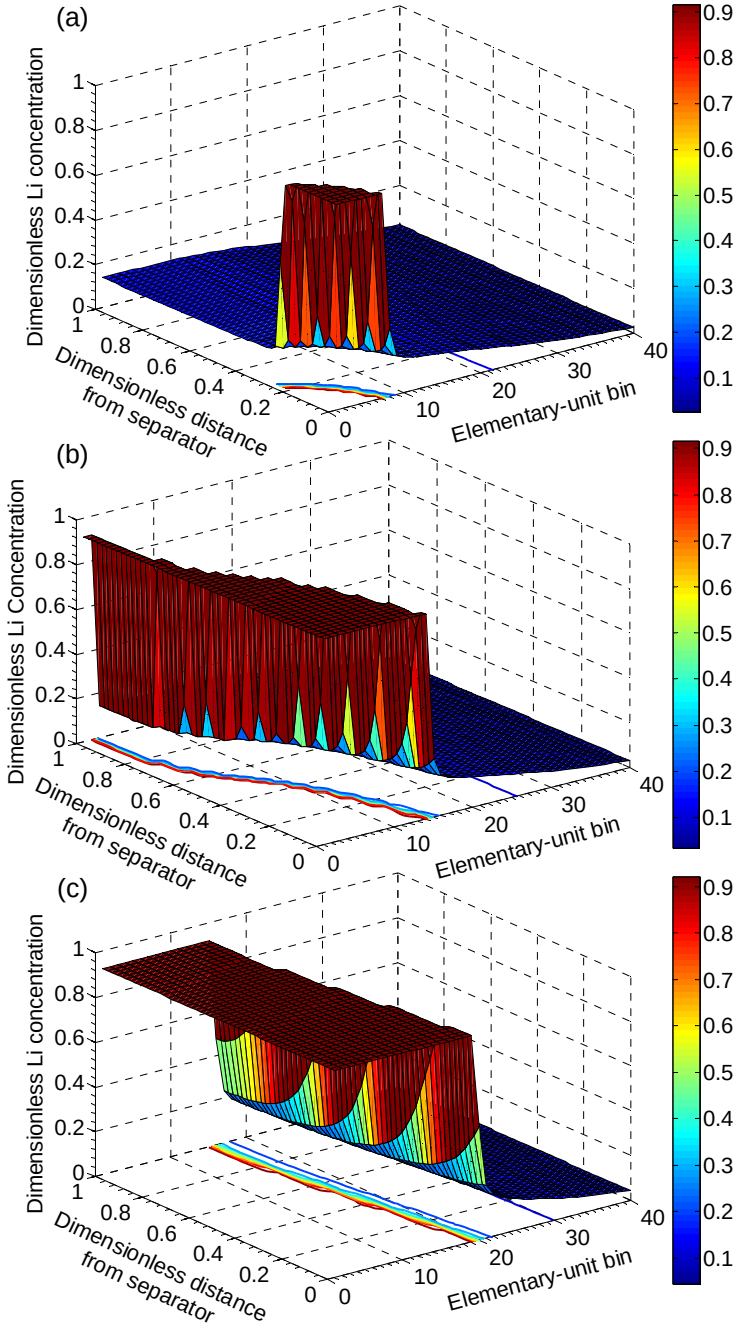

Figure 5-5. The relation between degree of lithiation, location within electrode and unit resistance at (a) 10%, (b) 20% and (c) 50% depths of discharge during C/10 discharge computed according to model.

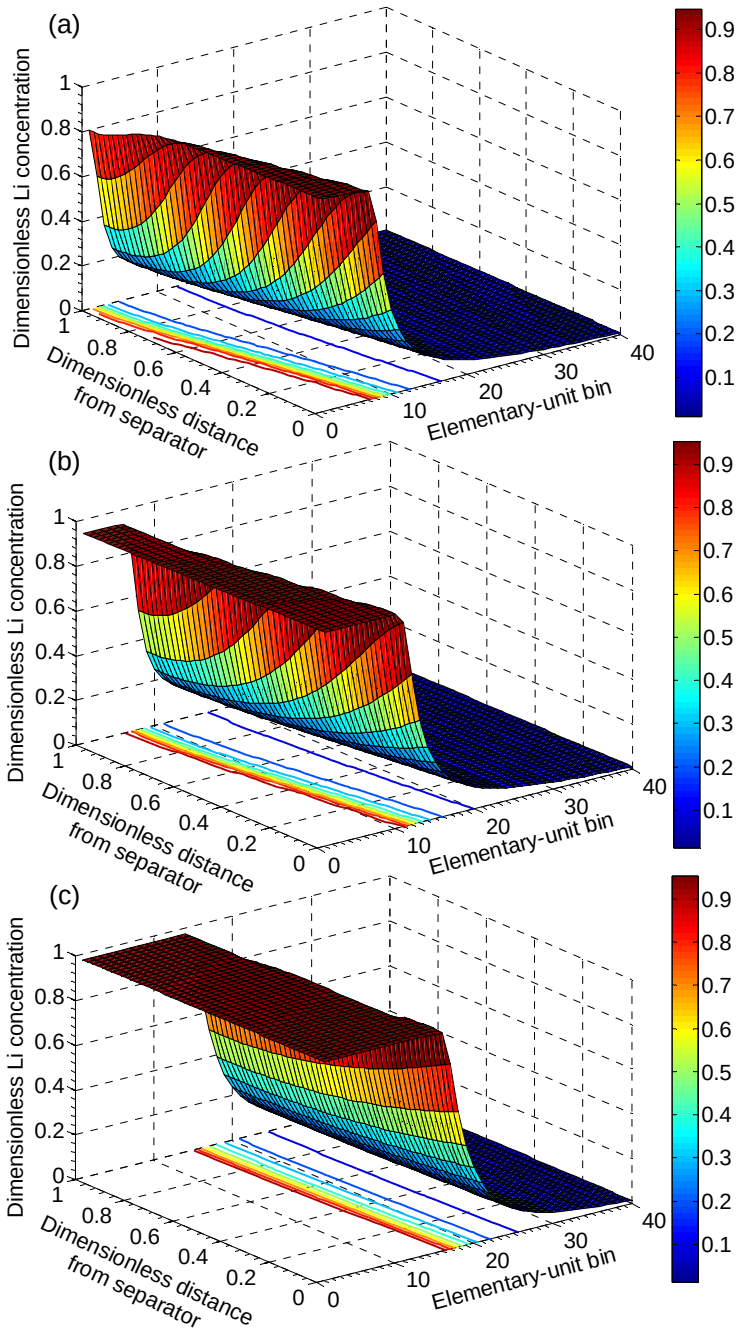

Figure 5-6. The relation between degree of lithiation, location within electrode and unit resistance at (a) 10%, (b) 20% and (c) 50% depths of discharge during 3C discharge computed according to model.

The variation of Φ_1 and Φ_2 across the electrode thickness is caused by electronic and ionic transport losses in the solid and liquid phases, respectively. However, the large effective electronic

conductivity measured for the electrode assures a uniform Φ_1 and leaves the electrolyte transport alone responsible for non-homogeneous lithiation across the electrode, at least during the first half of the process. According to conventional views, lithiation non-uniformities across the electrode are expected to be negligible at low rates as a result of negligible porous-electrode effects [139]. The counter results shown in Figure 5-5, however, rely on the very foundation of the model: lithiation proceeds unit by unit at low rates and follows a sequence determined by the variation in polarization among units, even though minuscule. As such, depending on the electrode design (i.e., unit-level versus electrode-level losses), porous-electrode effects may not be ignored for the simulation of LFP and other similar phase-change electrodes at low rates.

Since lithiation proceeds towards more resistive units, the polarization to lithiate a given number of units would be expected to grow as discharge continues. On the other hand, an increase in the electrode polarization provides enough driving force to activate additional units which counterbalances the excess polarization. As a result, the diffuse interface between Li-rich and Li-poor phases becomes wider as discharge advances (i.e., increase in the dispersion of contour curves in Figure 5-5a-c) indicating a larger number of active units are simultaneously becoming involved in the lithiation process.

The model also predicts segregation of elementary units into three groups of Li-poor, lithiating (active) and Li-rich units at relatively high rates as shown for example in Figure 5-6 for the electrode discharged at 3C. Nonetheless, the number of active units increases as the applied current increases which is reflected in a wider phase interface as well as a more uniform electrode-scale lithiation at different depths of discharge in Figure 5-6a-c compared to the same stages during C/10 discharge in Figure 5-5a-c. An increase in the applied current raises the overpotential of the active units which, in turn, increases the overall electrode polarization and, consequently, drives more units to participate in the lithiation process to an extent that is determined by their resistances. It explains the small variation in electrode potential at intermediate electrode utilization which becomes more accentuated as the applied current increases (Figure 5-3a).

This change in electrode dynamics whereby lithiation proceeds in a unit-by-unit sequence at low C-rates but by a mixed sequential-parallel order at high rates is the outcome of the interplay between the non-equilibrium single-phase lithiation of elementary units (i.e., non-monotonic SEQ, Figure 5-1) and the non-uniform resistance distribution among the units as obtained by fitting to the experimental data (Figure 5-2). The former has less influence at higher rates since the potential gap

between the upper and lower spinodal points (i.e., the driving force for unit-by-unit transformation) becomes negligible compared to the overall electrode polarization.

This dependence of lithiation mechanism on current is in agreement with observations from *in-situ* [11, 12, 81, 82] and ex-situ [74-76] phase mapping experiments where the population of particles with intermediate compositions (i.e., active particles) was observed to be directly proportional to the applied current. The improvement of lithiation dynamics at high currents and the non-equilibrium single-phase lithiation of each unit explain the excellent rate capability (end capacity as a function of applied current) of LFP electrodes. It is also consistent with the apparent dependence of particle size on applied current in Ref. [141] and in the diffusion-limited modeling study of Chapter 3 where a shift in the particle-size distribution toward smaller sizes (i.e., a shorter diffusion time) was required for the model to fit experimental end-capacities at higher rates.

5.4.4 Intermittent Galvanostatic Discharge

The galvanostatic intermittent titration technique is a common method to obtain dynamic and thermodynamic properties of insertion battery materials [156, 171]. More specifically, GITT can be used to estimate the chemical diffusion coefficient as a function of the concentration of inserted species in the host material by tracing the transient electrode potential during current pulses applied at various DoDs. It is, therefore, worth examining the electrode dynamics during GITT experiments using the proposed model where intra-unit diffusion limitations are completely ignored.

Three sets of experimental GITT data obtained from the same electrode were compared with the simulations conducted using the same set of parameters (including the SEQ and the bimodal RD) obtained previously by fitting the model to continuous galvanostatic discharge data at C/10 and 2C.

Figure 5-7 shows a comparison of the experimental and simulated responses to GITT experiments conducted according to the following waveforms: i) 2 min 1C pulses followed by 2 h relaxation periods (2min P-2h R, Figure 5-7a-b), ii) 2 min 1C pulses followed by 15 min relaxation periods (2min P-15min R, Figure 5-7c-d) and iii) 6 min 1C pulses followed by 2 h relaxation periods (6min P-2h R, Figure 5-7e-f). A fairly good match between the model and experiment is observed for all operating conditions during both the current pulse and relaxation periods. The model captures the characteristic shape of electrode response to the input current waveform. In the three cases, the amplitude of the potential response increases from pulse to pulse and a longer time is required for the electrode to relax when the current is switched off as the overall depth-of-discharge increases.

However, the model is not as accurate in capturing the instantaneous potential changes when current is initially switched on and the subsequent gradual potential evolution when current is flowing, although the agreement is very good over the majority of the relaxation steps (see insets in Figure 5-7). In the case of the 2min P-2h R experiment, the model slightly over-predicts the end-of-discharge capacity which coincides with the under-prediction of electrode potential during the last few (5 or 6) pulses (Figure 5-7a). Nonetheless, the characteristic shape of the potential response of the electrode to GITT pulses both under current and during relaxation is reproduced by the proposed model without including solid-state diffusion that has been commonly held responsible for the gradual evolution of electrode potential [171].

The instantaneous electrode polarization measured experimentally is nearly constant for all pulses throughout the 3 GITT experiments with a value of 14.1 ± 1.5 mV. The computed instantaneous polarizations are also nearly constant for all current pulses although they (39 ± 1.5 mV) are higher than the experimental value. Note that effects of electrochemical double-layer are significant at short times but are not accounted for in the model for the sake of simplicity. It turns out that the instantaneous polarizations depend not only on the resistance distribution but also on the SEQ; our simulations show that a thermodynamic model without a high-order term (i.e., the term $B(2y_k - 1)^C$ omitted in Eq. (5-4)) yields an instantaneous polarization that is not constant but varies with the DoD. With a constant instantaneous polarization throughout the experiment, the change in the gradual portion of the potential response from pulse to pulse can be attributed mostly to the fact that the electrode is becoming more completely discharged and available elementary units are becoming more resistive. Based on our model, this gradual evolution over the course of the pulse and relaxation periods is attributed to the collective dynamics of inter-unit transport which involves the resistance distribution as well as the equilibrium potential. Due to this dependence, the use of transient methods such as GITT should prove useful for estimating the non-monotonic SEQ which is crucial for modeling and quantitative assessment of LFP electrodes. For example, Figure 5-8 shows the effect of the SEQ on the computed electrode response to the 2 min pulse – 2 h relaxation GITT waveform. The two cases depicted correspond to the two non-monotonic SEQs shown in Figure 5-1 obtained from the modified Margules model (Eq. (5-4)) for an asymmetric dependence on lithium stoichiometry (i.e., $A_1 = 1.15, A_2 = 2.2$, as used in all simulations throughout this chapter) and a

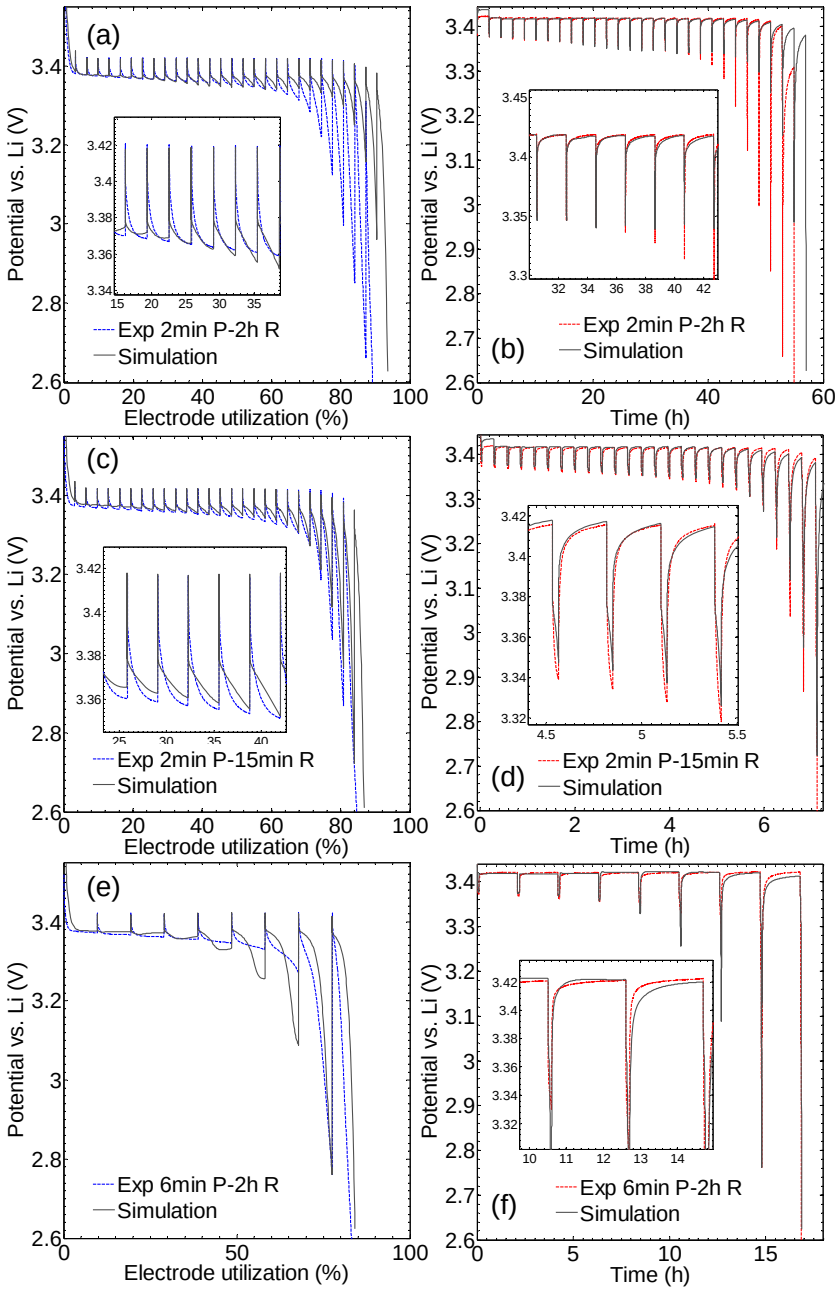

Figure 5-7. Comparison of experimental and simulated responses to the following GITT waveforms: (a), (b) 2 min pulse – 2 h relaxation; (c), (d) 2 min pulse – 15 min relaxation; and (e), (f) 6 min pulse – 2 h relaxation. In all cases, 1C current pulses are applied.

symmetric dependence (i.e., $A_1 = 2.98, A_2 = 0$, as an example of a modified regular solution). This comparison indicates that the slight asymmetry assumed in the SEQ evidently removes the anomaly

in the simulated GITT potential-capacity profile as compared to the experimental data. Accurate analysis of the SEQ is beyond the scope of this thesis and warrants further in-depth research.

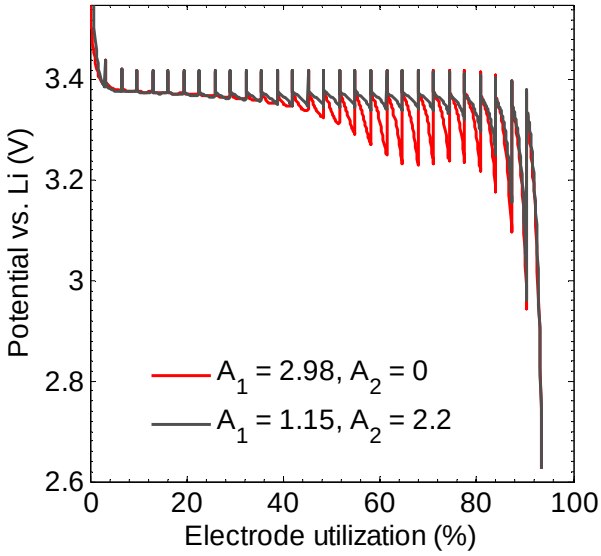

Figure 5-8. Comparison of simulated responses to a GITT 2min pulse - 2h relaxation waveform obtained using the symmetric (red) and asymmetric (gray) SEQ shown in Figure 5-1.

The GITT method is also frequently used by researchers to obtain the equilibrium potential of intercalation/insertion electrodes as a function of composition by recording the open-circuit potentials (OCP) at the end of each relaxation step [156, 171]. The measured OCPs of the electrode obtained during the three GITT experiments are compared with the corresponding simulated values and the simulated quasi-static (C/200) charge/discharge curves in Figure 5-9. The good agreement between the simulated and experimental OCPs further validates the proposed model. The SEQ is the main determining factor at low rates and under open-circuit conditions; the quasi-static potential hysteresis defines the bounds for the OCPs measured during GITT experiments having long relaxation times [109]. It can be seen in Figure 5-9a and c that, for the most part, a long enough relaxation step of 2 h ensures that the final OCPs fall well within the range of upper and lower quasi-static potentials, while the final OCPs obtained when only 15min relaxation is allowed end up much closer to the lower quasi-static potential bound (Figure 5-9b). It should be noted that the last few measured and simulated OCPs fall below this lower bound in all GITT experiments, indicating that inter-unit transport

limitations are still significant and longer relaxation periods are required for the electrode ensemble to reach equilibrium, according to our model.

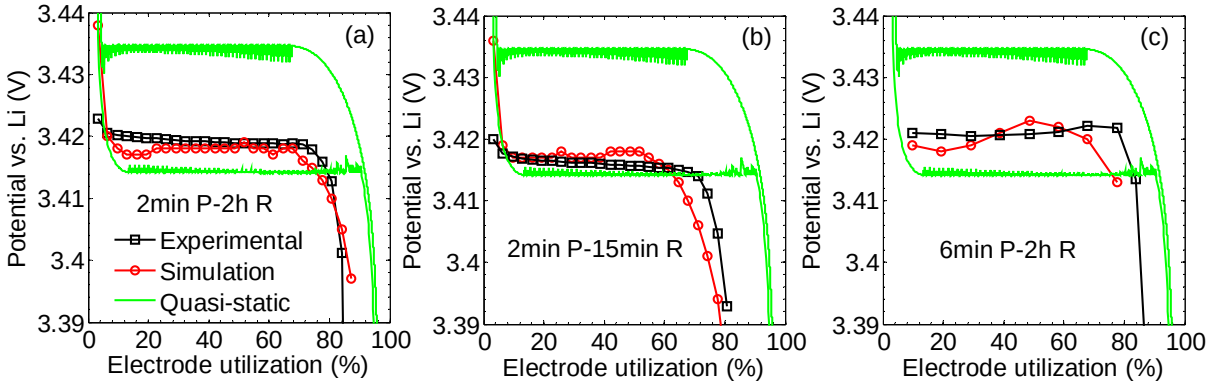

Figure 5-9. Comparison of the variation of experimental and simulated OCPs of the electrode with DoD obtained from the GITT waveforms: (a) 2 min pulse – 2 h relaxation, (b) 2 min pulse – 5 min relaxation and (c) 6 min pulse – 2 h relaxation. In all cases current pulses of 1C are applied. Resistances are set to zero in the quasi-static simulations.

The responses to the 2min P-2h R GITT waveform (originally shown in Figure 5-7a) and to the continuous galvanostatic discharge at 1C (originally shown in Figure 5-3a) are compared for both the experimental and simulated data in Figure 5-10a and b, respectively. It has been reported previously that the polarization of LFP electrodes during GITT pulses at certain current amplitude overshoots that of a continuous galvanostatic charge/discharge at the same current [16, 17, 109]. However, on the basis of the experimental results shown in Figure 5-10a, such a trend does not appear to be a general characteristic of LFP electrodes. The electrode potential during GITT closely matches (only slightly overshoots) the continuous discharge curve over the first ~70% of electrode utilization, but undershoots the response to the continuous discharge thereafter to the extent that it yields a greater end-of-discharge capacity (~88%) compared to that continuous discharge (~80%). Although not shown here, the capacity gain becomes smaller as the relaxation steps become shorter (i.e., ~84% in the case of 2min P-15min R GITT, Figure 5-7c and d) or the pulse duration becomes longer (i.e., ~84% in the case of 6min P-15min R GITT, Figure 5-7e and f). A similar trend is observed with the simulations. This variation in the performance of different LFP samples is attributed to both thermodynamic properties of the active material (e.g., unit size, level of defects and impurities) and dynamic properties of the electrode as a whole (e.g., electrode formulation and manufacturing, the

presence of secondary conductive phases). Based on conventional solid-state diffusion-limited models, one would attribute the larger capacity at the end of the GITT experiment than that of the continuous discharge to the reduction in the Li concentration gradient within the LFP units due to the intermittent relaxation steps. This would have the effect of delaying intra-particle diffusion limitations which dominate the electrode performance at high utilization. Using our model, however, we link the larger capacity at the end of GITT discharge to inter-unit phase separation resulting from the bi-stable nature of LFP and the non-uniform distribution of resistance among elementary units.

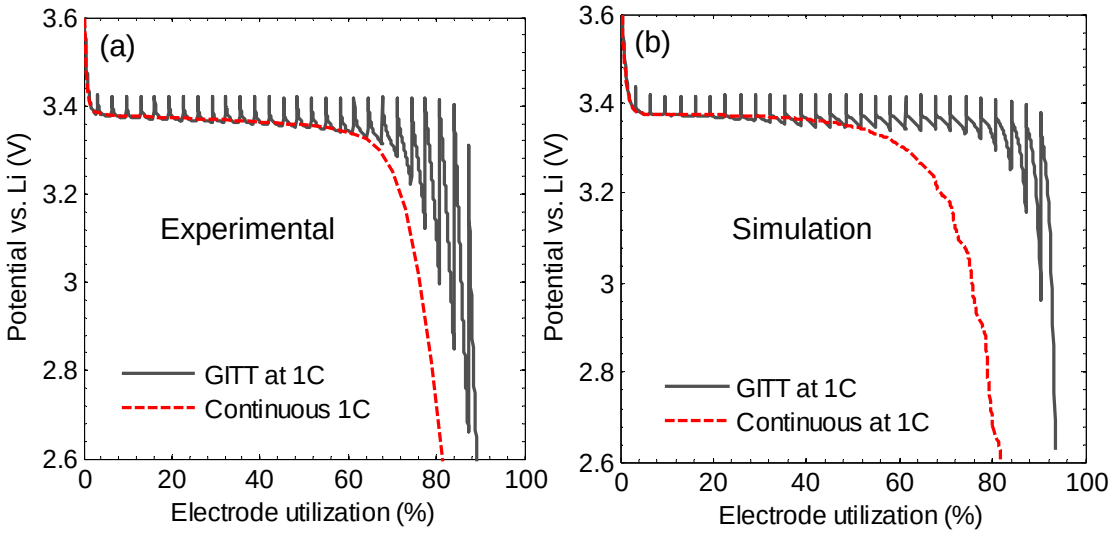

Figure 5-10. Comparison of responses of LFP electrode to 2 min pulse – 2 h relaxation GITT waveform and to continuous discharge obtained from (a) experiments and (b) simulations. In all cases, a current of 1C is applied.

In order to more closely follow the dynamics of electrode lithiation during GITT, the variation in utilizations are plotted depending on unit resistance and position across the electrode before and after the 2 h relaxation of 2nd and 4th pulses in Figure 5-11. Figure 5-12 presents utilizations as a function of unit resistance before and after the 2 h relaxation period of pulses 8, 12, 16, 20, 24 and 28. As evident in Figure 5-11, a diffuse interface exists between the Li-rich and Li-poor domains immediately after the current is interrupted, but becomes sharper by the end of the subsequent relaxation period (note that the width of the interface indicates the number of active units). This implies that the flow of current during the first few pulses converts some elementary units from Li-poor to Li-rich, whereas the subsequent relaxation step provides enough time for the unstable transforming units to settle into either the Li-rich or Li-poor phase depending on which is more

quickly accessible. The results in Figure 5-11 also show that the phase transformation across the electrode is non-uniform due to transport limitations within the electrolyte, as discussed before.

In contrast to the first few pulses, the separation between Li-rich and Li-poor becomes very sharp once pulses 8 through 20 are reached (Figure 5-12a-d) both before and after the relaxation steps. However, the transition becomes less sharp once again by the time that pulses 24 and 28 are applied (Figure 5-12e-f, note that the unit utilization over electrode-scale is nearly uniform and so not included in this figure). This behavior suggests that other pathways for the intermittent lithiation of the LFP electrode may exist depending on the overall DoD and under the specific operating conditions considered.

Despite the fact that each current pulse lithiates the electrode to the same extent throughout the experiment, the diffuse interface between Li-rich and Li-poor domains remains relatively narrow at the end of intermediate pulses 12 and 16 (Figure 5-12c-d) implying that the phase transformation does not occur during the pulse period. Instead, stable Li-rich units (i.e., $\mathrm{Li}_{1-\epsilon'}\mathrm{FePO}_4$, $\epsilon' \approx 0.1$) accommodate the entire incoming Li flux.

Each pulse begins with filling the solid-solution capacity available in the least-resistive Li-rich units. Since the incremental depth-of-discharge during each current pulse is smaller (~3.3% of total electrode capacity) than the available capacity in the Li-rich solid-solution end-member, electrode lithiation proceeds entirely via a stable solid-solution pathway during the closed-circuit portion of the intermediate pulses followed by a redistribution of Li between the Li-rich and Li-poor units during the subsequent open-circuit periods. The latter phenomenon is rather general and manifested in displacement of the phase boundary in Figure 5-12a-f during the relaxation periods.

The available Li-rich solid-solution capacity at any overall depth-of-discharge is calculated according to $\epsilon' X$ where X is the fraction of Li-rich phase and is related to the number of applied pulses N_p, the incremental depth-of-discharge $\Delta\mathrm{DoD}$ and solid-solution compositions ϵ and ϵ' according to $X = \frac{N_p \times \Delta\mathrm{DoD} - \epsilon}{1-\epsilon-\epsilon'}$ (the overall DoD is equal to $N_p \times \Delta\mathrm{DoD}$). It is assumed that the solid-solution compositions are uniform among units, invariable with time and equal to their equilibrium values (i.e., ϵ and $1-\epsilon'$ for Li-poor and Li-rich, respectively). The stable solid-solution lithiation pathway takes over the biphasic lithiation mechanism when the cumulated solid-solution capacity becomes in excess of the incremental depth-of-discharge (i.e., $\epsilon' X > \Delta\mathrm{DoD}$). Taking $\epsilon \cong \epsilon' \cong 0.1$ and $\Delta\mathrm{DoD} \cong 0.033$, electrode lithiation proceeds purely via the stable solid-solution path beyond the

11^{th} pulse (i.e,, $N_p > 11$) as a rough estimate. According to the model, a pure solid-solution mechanism is unbearable by the electrode for $\epsilon' < \Delta\text{DoD}$ which is incidentally the case for the 6min P-2h R GITT experiment.

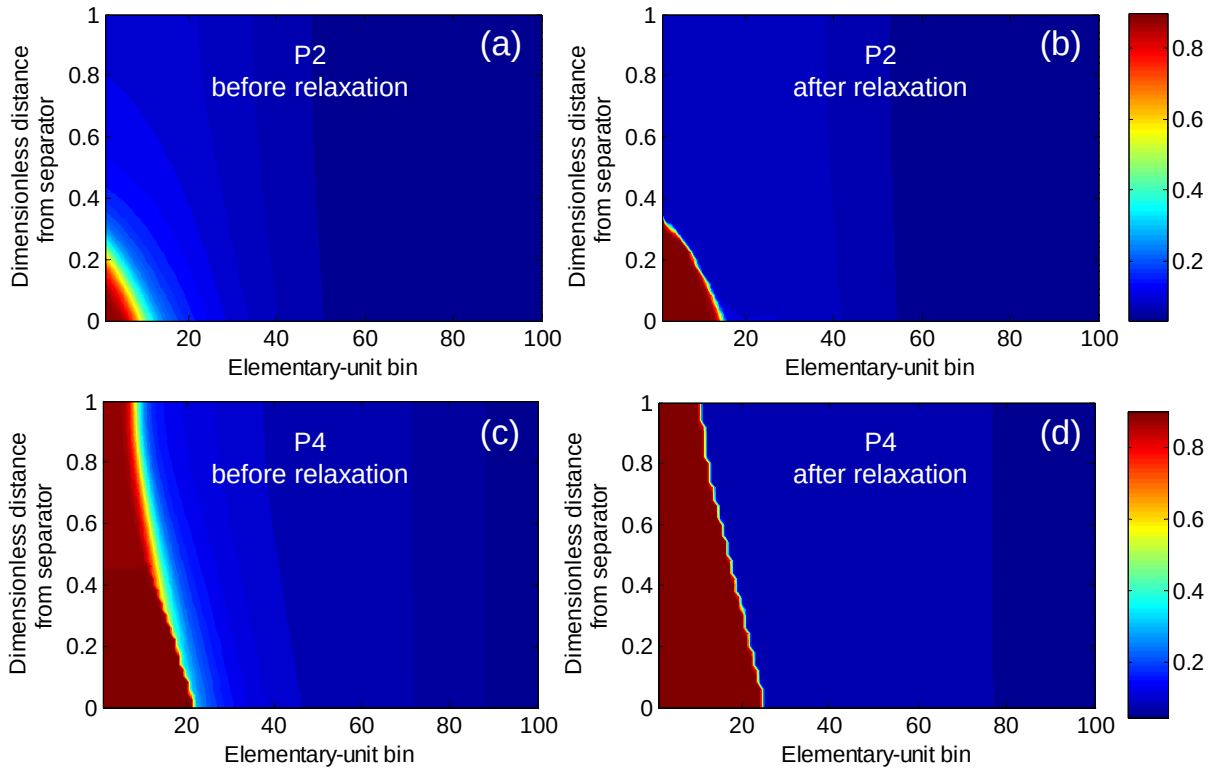

Figure 5-11. Variation of extent of lithiation in the LFP electrode depending on unit resistance and location before (a) and after (b) 2^{nd} pulse relaxation and before (c) and after (d) 4^{th} pulse relaxation of the 2min P – 2h R GITT waveform. Deep red denotes Li-rich and deep blue indicates Li-poor units.

The applied current is distributed among the already transformed Li-rich units in the stable solid-solution lithiation regime which is in clear contrast with the biphasic lithiation mechanism where the transforming units sustain most of the applied current.

During the last few pulses (e.g., 24^{th} and 28^{th} pulses, Figure 5-12e-f), however, the electrode experiences incomplete relaxation due to the progressively more sluggish inter-unit transport (i.e., due to higher resistances of the remaining units) towards the end of discharge, as mentioned before.

A transition lithiation stage may be regarded as mediating the above two pathways (e.g., 8th and 12th pulses shown Figure 5-12a-b) where the Li concentration in a number of Li-poor units also increases to and slightly above the lower spinodal composition during the current pulse in addition to Li uptake by the Li-rich units. These so-activated units are either converted completely to a stable Li-rich state or recoil to a stable Li-poor state during the relaxation period.

In summary, discharge of the LFP electrode during 2min P-2h R GITT occurs in three different stages:

i) closed-circuit biphasic lithiation and open-circuit phase transformation operative at the first few pulses (Figure 5-11),

ii) closed-circuit stable solid-solution lithiation (Li-poor and Li-rich) and open-circuit phase transformation in the middle pulses (Figure 5-12a-b),

iii) closed-circuit stable solid-solution lithiation (Li-rich) and open-circuit transformation in the later pulses (Figure 5-12c-f).

These different regimes manifest themselves in the potential-capacity curves shown in Figure 5-7 where the concavity of the potential response during pulses changes from upward at the beginning to downward at the end of GITT. The behavior at the beginning reflects the electrode potential determined mostly by units residing on the Li-poor branch of the SEQ (majority of LFP units are Li-poor at the first half of GITT) which is concave upward (Figure 5-1), while that at the end indicates the electrode potential controlled by units on the Li-rich branch of the SEQ (majority of LFP units are Li-rich at the second half of GITT) which is concave downward. Similar trend is observed in both experimental data and simulation results.

The lithiation mechanism during intermittent discharge appears to differ markedly from that during continuous discharge and depends on the overall depth-of-discharge of the electrode, GITT waveform (i.e., pulse step amplitude and duration as well as relaxation time) and, of course, the physico-chemical properties of LFP (i.e., RD and SEQ).

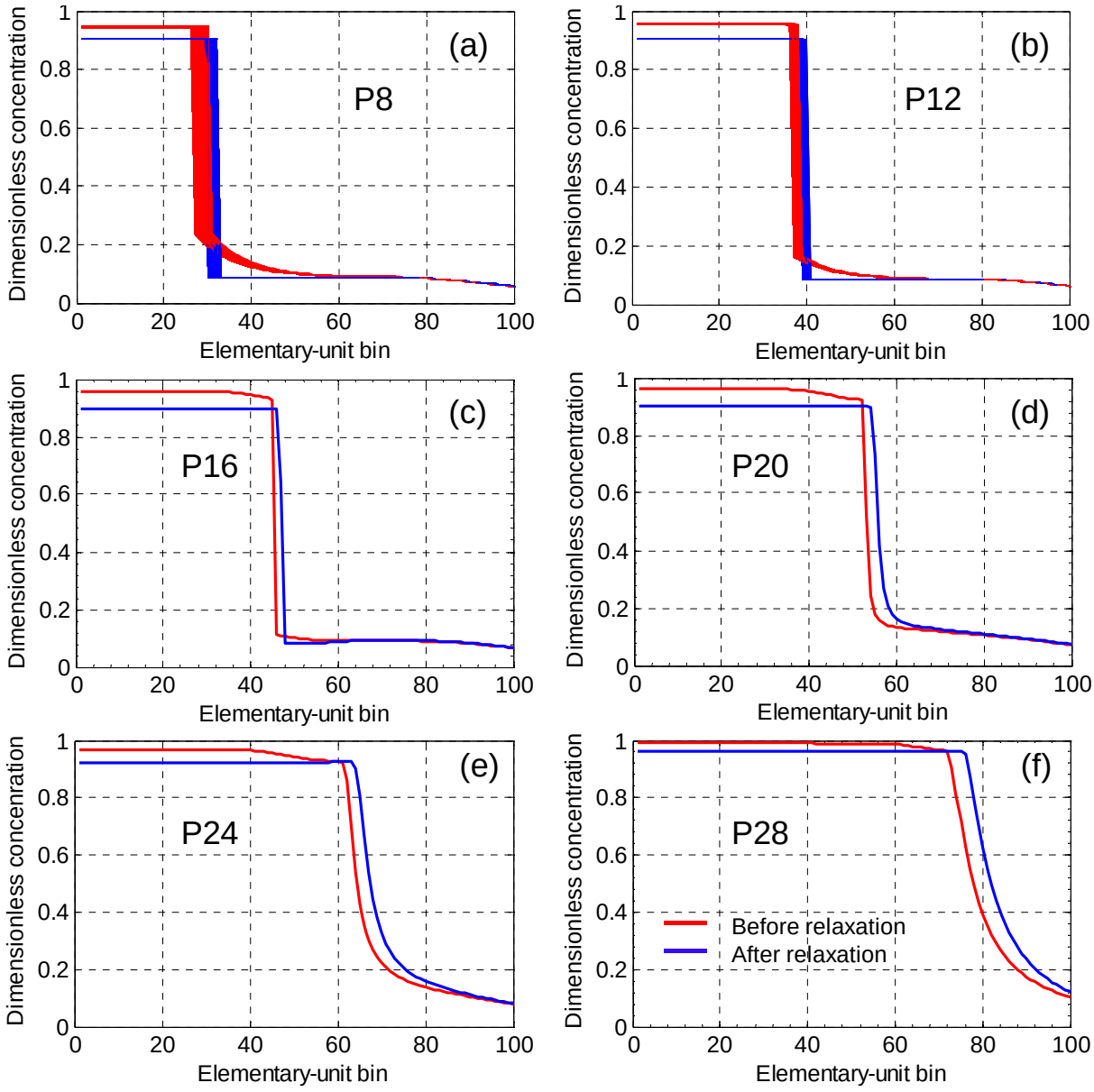

Figure 5-12. Variation of computed dimensionless lithium concentration with Elementary-unit resistance before (blue) and after (red) the relaxation following current pulse (a) 8, (b) 12, (c) 16, (d) 20, (e) 24 and (f) 28 of the 2min P – 2h R GITT waveform. The distribution of concentration with location is almost uniform and not shown.

5.5 Conclusion

In this study, the mesoscopic model previously developed in Chapter 4 for phase-change insertion electrodes was incorporated into porous-electrode theory and validated by comparing the simulation results with experimental data obtained during continuous and intermittent galvanostatic discharge of a commercial $LiFePO_4$ electrode at various operating conditions. The model features elementary mesoscopic units that undergo non-equilibrium Li insertion/extraction and extremely fast solid-state diffusion. An asymmetric solid-solution model describes the equilibrium potential of individual elementary units as a non-monotonic function of composition. A bimodal lognormal resistance distribution is assumed to account for disparity of insertion dynamics among elementary units.

The simulation results agree well with experimental data obtained from continuous discharge experiments over the range from low (C/50) to high (3C) applied currents. Both the loss in potential at intermittent utilization and end-of-discharge capacity are captured by the model.

GITT simulations under three different operating conditions compared well with experimental data confirming the fidelity of the proposed model. According to this model, the slow evolution of electrode polarization during each current pulse and the subsequent relaxation period in the GITT experiment are governed by the inter-unit rather than intra-unit Li transport in $LiFePO_4$ electrodes. The many-unit effects appear at relatively large time scales depending on the depth of discharge and should not be confused with solid-state diffusion. As such, GITT experiments that are typically used to determine diffusion coefficient of inserted species in solid-solution systems, may also be used to estimate the thermodynamic properties (i.e., single-unit equilibrium potential) as well as the dynamic properties (e.g., resistance distribution) of phase-change materials.

Further analysis of the GITT experiments suggests that the electrode discharge dynamics strongly depends on the operating conditions. The active phase-change lithiation mechanism during continuous discharge process is replaced by a stable solid-solution pathway during the closed-circuit portion of the GITT pulses and a passive phase transformation during subsequent open-circuit periods in a GITT experiment with small enough incremental DoD. Depending on the overall depth-of-discharge of the electrode and the incremental depth-of-discharge during each GITT pulse, the solid-solution capacity available in the Li-rich end-member may be able to accommodate the incoming Li entirely without the need to activate additional units. Instead, the redistribution of Li among units during relaxation equilibrates the solid-solution composition by transforming a few Li-poor units to Li-rich ones.

Chapter 6

Determination of the Transport Properties of Concentrated Binary Electrolytes Using a Four-Electrode Electrochemical Cell

The following chapter is a follow-up to the work previously published by M. Farkhondeh, M. Pritzker, M. Fowler and C. Delacourt in *J. Electrochem. Comm.* [163] entitled:

"Transport Property Measurement of Binary Electrolytes Using a Four-Electrode Electrochemical Cell"

and a separate manuscript to be submitted by the same authors entitled:

"Determination of the Transport Properties of Concentrated Binary Electrolytes Using a Four-Electrode Electrochemical Cell"

This thesis author's specific contribution to this paper was to design the electrochemical cell, design and conduct experiments, develop the model, conduct simulations and parameter estimation, prepare all the graphics and results, prepare the manuscript and reviewer edits with direction from the project advisors who were co-authors. All authors reviewed the manuscript.

6.1 Introduction

Further improvement of the power capability of advanced batteries requires optimization of their dynamic behavior including electrolyte mass transport among other things. Despite their rigor, state-of-the-art methods that estimate electrolyte transport properties are arduous, time-consuming and prone to error [31, 118].

Battery electrolytes are, in most cases, concentrated solutions containing at least one salt dissolved in one or more solvent [18] commonly assumed to be a binary electrolyte. Three independent properties (ionic conductivity, salt diffusion coefficient and cation transference number) must be determined as functions of concentration and temperature to fully characterize a concentrated binary electrolyte [107].

Measurement of the ionic conductivity is simple and usually conducted by means of a standard AC impedance method. On the other hand, measurement of the salt diffusion coefficient and cation transference number is very difficult and so has been limited to the most commonly used electrolytes [31-44]. As described in section 2.2, the restricted diffusion [112] and semi-infinite

diffusion methods are most commonly used to estimate the salt diffusion coefficient and cation (or anion) transference number. Because the solution is non-ideal, thermodynamic measurements usually conducted in concentration cells are required to accurately determine the transport properties [107]. The thermodynamic factor can be determined once the transference number is known [31, 118]. Thus, three separate sets of measurements obtained from the semi-infinite diffusion, restricted diffusion and concentration-cell experiments must be combined in order to obtain the salt diffusivity, transference number and thermodynamic factor at a given concentration.

Restricted diffusion and semi-infinite diffusion experiments are commonly carried out in symmetric two-electrode cells wherein the electrodes are located at the two ends confining the electrolyte. Current is applied to the electrodes for a certain period of time and voltage is recorded across the same electrode pair either immediately after the circuit is opened (semi-infinite diffusion) or while the concentration profile is relaxing (restricted diffusion). However, due to the complicated, not well-understood kinetics of the charge-transfer reaction at the surface of the electrodes, it is not possible to accurately relate the evolution of the closed-circuit cell voltage to the variations of the electrolyte concentration and potential across the cell. As a result, the two-electrode characterization methods fall short in retrieving useful closed-circuit data that might otherwise be used as a rich source of information regarding the dynamics of mass transport in the solution.

In this chapter, we present a novel electrochemical method that simultaneously estimates the transport properties of concentrated binary electrolytes. The method uses a four-electrode electrochemical cell and, unlike conventional methods, is able to make use of the data obtained from both the closed-circuit and open-circuit operation modes. Variations in the electric potential of the electrolyte are recorded across two reference electrodes (i.e., potential sensors) while a rectangular current pulse is applied to the working and counter electrodes. A thorough description of this cell design and new method is provided. A general mathematical model is presented which is applicable to a variety of electrolyte systems such as Li-, Na-, Zn- and Mg-based electrolytes. The model features a bipolar effect at the surface of the reference electrodes and takes into account charge-transfer induced (faradaic) convection in a 2-D axi-symmetric geometry. The methodology is further discussed by characterizing transport properties of 2 Li-based non-aqueous electrolytes and compared with conventional electrochemical routines for transport property estimation. Finally, a sensitivity analysis of the kinetic and design parameters is conducted.

6.2 Electrochemical Cell Design

The experimental setup involves a cylindrical electrochemical cell consisting of counter and working electrodes located at the two ends and two annular potential sensors (PS) placed midway between the counter (CE) and working (WE) electrodes. The cell is made cylindrical to reduce the dimensionality of the computational domain from 3-D to 2-D axi-symmetric. Figure 6-1 shows an exploded view of the cell. The cell consists of a 7-layer stack of rings—stainless steel connector, electrically wired PTFE spacer, PS,1, PTFE spacer, PS,2, electrically wired PTFE spacer and stainless steel connector. The potential sensors are wired to the stainless steel rings surrounding the WE and CE current collectors through the electrically wired PS-CE and PS-WE spacers. The hollow space within the ring stack is filled with a separator made from Whatman borosilicate glass microfiber filter (GF) grade D (7 layers). The separator helps to confine the solution within the working volume of the cell and to minimize convection that may otherwise happen due to external forces (e.g., vibrations) [39]. The inner diameter of each PS annulus is identical to the inner diameter of the PTFE spacers and the diameter of the WE and CE disks and of the separator. The spaces between PS,1 and WE and between PS,2 and CE are chosen to be identical and controlled by means of the electrically wired PTFE spacers [39].

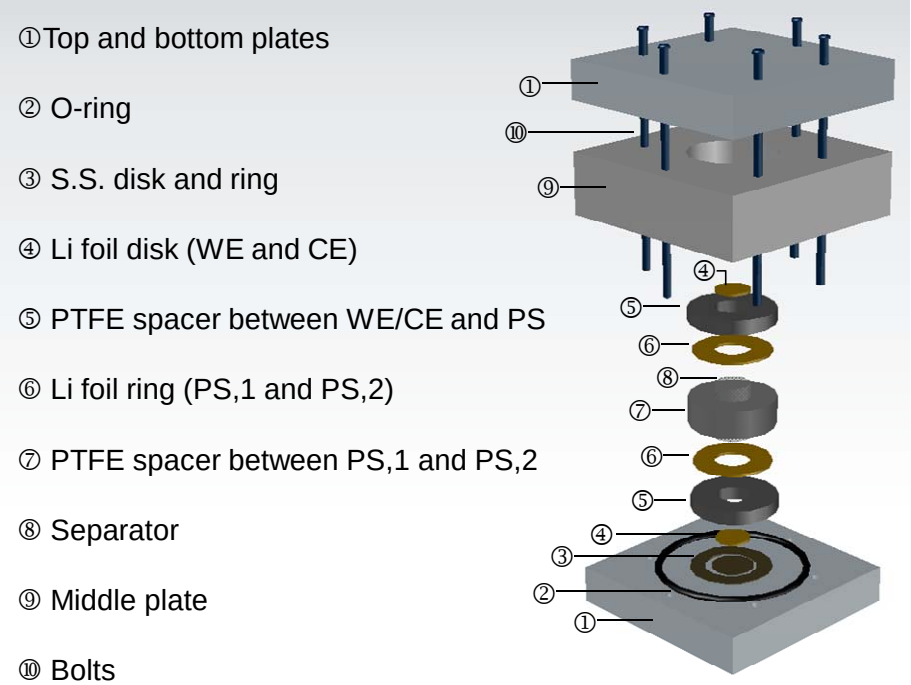

Figure 6-1. Exploded view of the four-electrode electrochemical cell.

Disks of 12.98 mm diameter are punched out of a 200 μm thick Li metal foil as the CE/WE. The PS annuli are prepared from the same Li foil. The thickness of the Li rings is measured to be 191 μm after the experiment is conducted. All of the non-metallic cell parts (i.e., spacers as well as the top, intermediate and bottom plates) are made of PTFE. In order that it can be used outside of the glove box, the cell is made air-tight by means of two EPDM rubber O-rings positioned in the top and bottom plates and held together using 6 bolts and nuts passing through the cell body.

6.3 Methodology

The proposed electrolyte characterization method consists of operating the cell galvanostatically by applying a rectangular current waveform to the WE and CE while the resulting variations in the electric potential of the electrolyte are recorded across the two potential sensors. The sensors are isolated from the WE and CE and are connected to an external circuit dedicated to potential measurement. No net current flows through the sensors except for the negligible current from the potentiometer. As such, the four-electrode cell provides direct access to the closed-circuit as well as open-circuit voltage in a manner not distorted by the main and side reaction kinetics or double-layer effects at the working and counter electrodes.

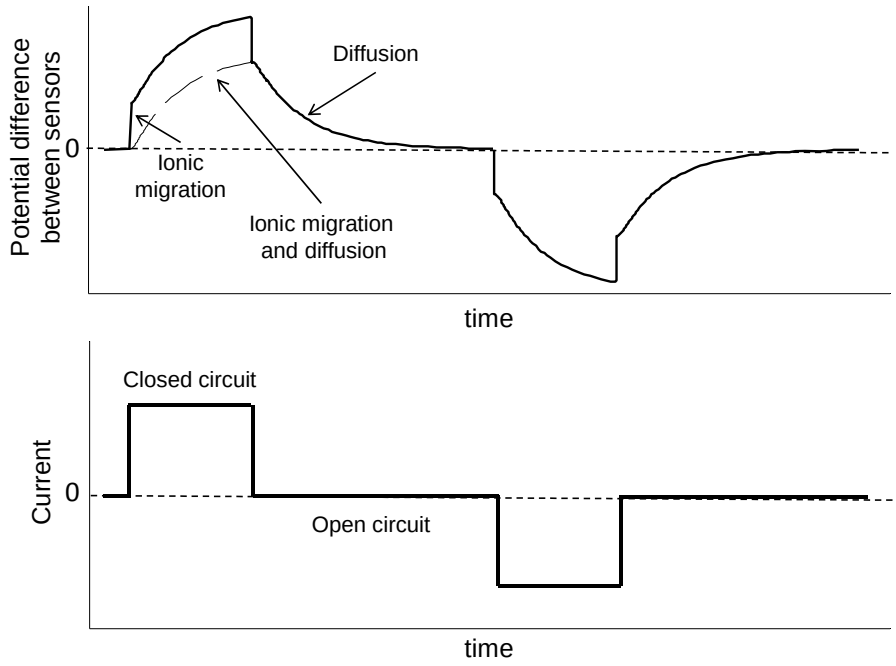

Figure 6-2. The potential difference between the two sensors (upper plot) in response a rectangular current waveform applied to the WE and CE (lower plot).

Figure 6-2 schematically reflects the voltage response of the four-electrode cell to a current waveform. Transport properties are estimated all at once by fitting a mathematical model to the potential difference between the two sensors during (closed-circuit) and after (open-circuit) the galvanostatic polarization. As shown in section 6.6, the recorded data exhibit unique features each of which can be unambiguously attributed to one of the three independent transport properties: i) instantaneous change of voltage at the outset and end of closed-circuit period is contributed solely by ionic migration (i.e., ionic conductivity of the electrolyte), ii) exponential decay of open-circuit data with time is controlled by diffusion (i.e., chemical diffusion coefficient) and iii) transient portion of closed-circuit data is attributed to both migration and diffusion (i.e., transference number).

6.4 Experimental

The cell is assembled entirely in an argon-filled glove box (<1 ppm H_2O, <1 ppm O_2). The outer cell compartments (top, intermediate and bottom plates, O-rings and bolts and nuts) are washed with acetone and rinsed with dimethyl carbonate (DMC). The inner parts are stored in DMC for 30 min to make sure any salt deposit is removed. All cell parts are stored under vacuum in the ante-chamber of the glove box overnight prior to the cell assembly to minimize any chance of contamination.

The separator is placed in the cell and gradually soaked with the electrolyte before the cell is tightened. Care is taken to avoid gas bubbles trapping in the GF pores. Prior to its use in the glove box, the GF is stored under vacuum for 24 hours at 90°C to assure that the level of moisture contamination and other adsorbed species is minimized. Borosilicate glass has a density of 2.500 g cm^{-3} measured using a He pycnometer (AccuPyc 1330, Micromeritics Instrument Corp., USA). The porosity (i.e., the presumed volume fraction of electrolyte) of the separator is calculated to be ~ 0.92, given the volume of the cell and the weight and density of the separator.

Two electrolyte solutions, a commercial 1 mol L^{-1} solution of $LiPF_6$ in a 1:1 vol. mixture of ethylene carbonate (EC) and diethyl carbonate (DEC) (Sigma Aldrich) and a 1 mol L^{-1} solution of $LiPF_6$ in 1:1 vol. mixture of EC and DMC (Sigma Aldrich), are chosen as model systems for this study. These two systems differ only in the solvents (i.e., DEC vs. DMC) but are expected to have significantly different transport properties.

The cell is operated galvanostatically inside a temperature chamber (Cincinnati Sub-Zero MCB-1.2, USA) at 25°C using a multi-channel potentiostat/galvanostat (VSP, Bio-Logic, France). Rectangular waveforms with the following steps are applied to the cell: i) constant current in the

positive direction (i.e., anodic at WE and cathodic at CE) for 8 hours, ii) a rest period (zero current) of 16 hours, iii) constant current in the negative direction (i.e., opposite to step i) for 8 hours and iv) rest period for 16 hours.

The cell is oriented vertically with the WE positioned at the bottom. Only the response to the first half of the waveform is measured during the experiments. In this configuration, the electrolyte at the bottom reaches a higher solute concentration than at the top during the first half of the waveform since the oxidation reaction tends to concentrate the solution while the reduction reaction tends to dilute it. In this way, buoyancy effects are minimized. The current amplitudes applied to the WE and CE during the on-periods of the waveform described above range from 0.15 mA (~0.113 mA cm^{-2}) to 0.375 mA (~0.282 mA cm^{-2}). These currents are large enough to generate sufficient concentration polarization (i.e., appreciable signal-to-noise ratio), while at the same time small enough not to cause excessively long relaxation times and violate the model assumptions (e.g., isothermal operation). The resolution of potential measurement is set to 5 μV at a full scale range (FSR) of 0.2 V. The measurement accuracy is 0.1% FSR [172], i.e., $\pm$ 0.2 mV. Prior to the application of the waveform above, the cell is conditioned by applying the same waveform twice. The conditioning is required to form a stable solid electrolyte interphase as well as to improve the uniformity of charge-transfer reaction at the surface of the WE and CE. Harsh conditions are avoided to minimize irreversible loss of solute and solvent due to SEI growth.

6.5 Theory

6.5.1 Governing Equations

The mathematical model developed in this section describes species transport in a binary electrolyte according to concentrated-solution theory. The model is made general enough so that it can be applied to a variety of electrolyte systems for which a similar four-electrode cell setup can be used. To have an accurate insight on the cell design, the model features bipolar effects [173] occurring at the surface of the reference electrodes which perturbs the concentration and electric potential of the electrolyte locally where the sensors are located. As such, the model is developed for the actual 2-D axi-symmetric geometry. The model also takes into account faradaic convection. It will be shown in section 6.6 that the bipolar effects are negligible in the proposed cell design and under operating conditions relevant to electrolyte characterization which simplifies the model significantly and reduces the dimensionality of the computational domain to 1-D.

In a binary electrolyte, salt A dissociates into its ionic constituents $M_i^{z_i}$ with charge numbers z_i in accordance with the stoichiometric coefficients ν_i in the salt molecule. In the case of a binary electrolyte [107]:

$$A \rightleftharpoons \nu_+ M_+^{z+} + \nu_- M_-^{z-} \tag{6-1}$$

where $i = +$ for the cation and $i = -$ for the anion. Thus, a binary electrolyte contains three species—cation, anion and solvent ($i = 0$). Conservation of mass for each species i in the electrolyte in the absence of homogeneous chemical reaction leads to:

$$\varepsilon \frac{\partial c_i}{\partial t} = -\nabla \cdot \mathbf{N}_i \tag{6-2}$$

where ε is the separator porosity (the electrolyte is contained within a porous separator), t is time, c_i is the molar concentration referred to the pore volume and $\mathbf{N}_i$ is the superficial molar flux density of species i in the solution referred to cross-section area of solid matrix and pore space [107].

It is more convenient to re-cast these conservation equations in terms of the ionic current density, mass-average velocity and solute concentration which are all measurable quantities. Faraday's law can be applied to relate the fluxes of the species present to the current density flowing through the electrolyte:

$$\mathbf{i} = F \sum_i z_i \mathbf{N}_i \tag{6-3}$$

where $\mathbf{i}$ is the ionic current density, F is the Faraday constant. Multiplying both sides of Eq. (6-2) by Fz_i and summing over all species leads to the charge conservation equation

$$\nabla \cdot \mathbf{i} = 0 \tag{6-4}$$

given the Guggenheim electroneutrality condition $\sum_i z_i c_i = 0$ [174]. Eq. (6-4) is the conservation law of a measurable quantity and is simple enough to replace one of the mass balance equations in Eq. (6-2).

Multiplying both sides of Eq. (6-2) by the molar weight M_i of species i and summing over all species yields:

$$\varepsilon \frac{\partial \rho}{\partial t} = -\nabla \cdot (\rho \mathbf{v}) \tag{6-5}$$

where $\rho = \sum_i M_i c_i$ is the density of the solution (in g m^{-3}) and $\mathbf{v}$ is the superficial mass-average velocity referred to the area of both solid matrix and pore and is defined as:

$$\mathbf{v} = \frac{1}{\rho} \sum_i M_i \mathbf{N}_i \tag{6-6}$$

Eq. (6-5) replaces another species mass conservation equation in Eq. (6-2).

In a concentrated solution, constitutive expressions for species flux densities are obtained from the Stefan-Maxwell equations which express a local equilibrium between the transport driving force and the friction forces exerted on one species by the others [107]:

$$\frac{c_i \nabla \mu_i}{RT} = \sum_{j=1}^{N} \frac{c_i c_j}{c_\mathrm{T} \varepsilon^\gamma \mathcal{D}_{ij}} (\mathbf{v}_j - \mathbf{v}_i) \tag{6-7}$$

Where μ_i is the electrochemical potential of species i, R is the universal gas constant, T is temperature, $c_\mathrm{T} = \sum_i c_i$ is the total concentration of the solution, $\mathbf{v}_i$ is the superficial velocity of species i referred to the cross-sectional area (i.e., $\mathbf{N}_i = c_i \mathbf{v}_i$) and $\mathcal{D}_{ij}$ is the diffusion coefficient related to interactions between species i and j. The coefficient ε^γ corrects the Stefan-Maxwell diffusion coefficients for both porosity and tortuosity where γ is the Bruggeman exponent [175].

Flux density expressions in terms of the thermodynamic driving force are obtained by inverting the Stefan-Maxwell expressions. To this end, a reference frame is required to which the diffusion velocities can be unambiguously referred [107, 176]. In other words, the number of independent velocity difference terms becomes one less than the number of species in the solution, in line with the Gibbs-Duhem requirement for the electrochemical potential. The volume-average velocity, molar-average velocity, solvent velocity or any other arbitrarily defined velocity can replace the mass-average velocity as a frame of reference for diffusion; any one is preferred over the others providing it is convenient in a given situation [107, 176]. According to De Groot [176], the arbitrariness of the reference velocity is implied by Prigogine's theorem stating that, under the condition of mechanical equilibrium and irrespective of external forces, the entropy production rate associated with diffusion is the same regardless of the choice of reference velocity. It can be safely assumed that the state of mechanical equilibrium is realized very quickly and long before chemical equilibrium is reached in an enclosed rigid vessel (e.g., a diffusion cell) containing a liquid [176]. Such a mechanical equilibrium requires that the acceleration term (i.e., substantial time derivative

$D\mathbf{v}/Dt$ of the mass-average velocity) in the conservation of momentum vanishes and the viscous dissipation term is negligible. As such, in the absence of external forces (e.g., gravity or other body forces), the pressure drop across the cell becomes negligible and greatly simplifies the Stefan-Maxwell flux expressions and the Gibbs-Duhem relation.

In the majority of pseudo-two-dimensional battery models [108], the solvent is chosen as the frame of reference and its velocity is set to zero which simplifies the model since it allows convection to be neglected [177]. Although the solvent velocity is chosen as the reference to simplify the flux expressions, it is not set to zero in order to improve accuracy. Instead, an expression is derived to relate the solvent velocity to the other field variables and thermodynamic properties.

After some algebraic manipulation of Eq. (6-7), the cation and anion flux densities can be related to the solvent velocity to yield [107] :

$$\mathbf{N}_+ = -\frac{\nu_+ \varepsilon^\gamma \mathcal{D} c_\mathrm{T}}{\nu RT c_0} c \nabla \mu_e + \frac{\mathbf{i} t_+^0}{z_+ F} + c_+ \mathbf{v}_0 \tag{6-8}$$

and

$$\mathbf{N}_- = -\frac{\nu_- \varepsilon^\gamma \mathcal{D} c_\mathrm{T}}{\nu RT c_0} c \nabla \mu_e + \frac{\mathbf{i}(1 - t_+^0)}{z_- F} + c_- \mathbf{v}_0 \tag{6-9}$$

where

$$\mu_e = \nu_+ \mu_+ + \nu_- \mu_- = \mu_e^\theta + \nu RT \ln(c f_\pm) \tag{6-10}$$

is the chemical potential of the neutral combination of ions in the solution with the concentration $c = c_+/\nu_+ = c_-/\nu_-$ and μ_e^θ is the chemical potential of the neutral species at a secondary reference state. The mean molar activity coefficient $f_\pm$ is defined by:

$$f_\pm = \left(f_+^{\nu_+} f_-^{\nu_-}\right)^{1/\nu} \tag{6-11}$$

In this expression, f_i is the molar activity coefficient and $\nu = \nu_+ + \nu_-$ is the total number of moles of ions produced by the dissolution of one mole of salt. The diffusion coefficient of the electrolyte $\mathcal{D}$ based on a thermodynamic driving force and the cation transference number t_+^0 with respect to the solvent velocity are measureable properties and related to the Stefan-Maxwell diffusion coefficients $\mathcal{D}_{ij}$ as follows [107]:

$$\mathcal{D} = \frac{\mathcal{D}_{0+}\mathcal{D}_{0-}(z_+ - z_-)}{z_+\mathcal{D}_{0+} - z_-\mathcal{D}_{0-}} \tag{6-12}$$

and

$$t_+^0 = \frac{z_+\mathcal{D}_{0+}}{z_+\mathcal{D}_{0+} - z_-\mathcal{D}_{0-}} \tag{6-13}$$

To obtain an estimate for the solvent concentration c_0 in the above equations, one needs an equation of state for the total solution concentration c_T in terms of the pressure, temperature and solute concentration. At constant temperature and pressure, c_T is related to the partial molar volumes $\bar{V}_i$ of the dissolved species and solvent according to the summability relation [178]:

$$\frac{1}{c_\mathrm{T}} = \sum_i y_i \bar{V}_i \tag{6-14}$$

where y_i is the mole fraction of species i in the solution. Multiplying Eq. (6-14) by c_T gives:

$$\sum_i c_i \bar{V}_i = 1 \tag{6-15}$$

The partial molar volume $\bar{V}_e$ of the electrolyte can be defined as [107]:

$$\bar{V}_e = \nu_+\bar{V}_+ + \nu_-\bar{V}_- \tag{6-16}$$

and used in Eq. (6-15) to give:

$$c_0 = \frac{1}{\bar{V}_0}(1 - c\bar{V}_e) \tag{6-17}$$

$\bar{V}_e$ and $\bar{V}_0$ are measurable quantities and can be estimated through measurement of the solution density ρ at various electrolyte concentrations at constant pressure and temperature [107]:

$$\bar{V}_e = \frac{M_e - \frac{d\rho}{dc}}{\rho - c\frac{d\rho}{dc}} \tag{6-18}$$

and

$$\bar{V}_0 = \frac{M_0}{\rho - c\frac{d\rho}{dc}} \tag{6-19}$$

Substitution of Eq. (6-8) into Eq. (6-2) and incorporation of Eq. (6-4) give:

$$\varepsilon \frac{\partial c}{\partial t} = \nabla \cdot \left(\frac{\varepsilon^{\gamma} \mathcal{D} c_{\mathrm{T}}}{\nu R T c_0} c \nabla \mu_e \right) - \frac{\mathbf{i} \cdot \nabla t_+^0}{\nu_+ z_+ F} - \nabla \cdot (c \mathbf{v}_0) \tag{6-20}$$

This equation replaces the third conservation equation in Eq (6-2). Now constitutive expressions for **i** and $\mathbf{v}_0$ must be derived.

Eq. (6-9) is incorporated into an expression for the ionic current density, which flows via ion migration (i.e., motion of charged species under an electric field) in addition to diffusion. To this end, a proper definition for the electric potential in the liquid phase must be provided. Such a definition must capture the effect of varying composition and is, therefore, different from the electrostatic potential defined strictly for media of uniform chemical composition [107]. The potential of a reference electrode that is reversible with respect to an ion in the solution perfectly suits situations where significant concentration gradients exist [107]. The gradient of such an electric potential is obtained in reference to the following general electrode reaction:

$$s_- \mathrm{M}_-^{z_-} + s_+ \mathrm{M}_+^{z_+} + s_0 \mathrm{M}_0^{z_0} \rightleftharpoons n \mathrm{e}^- \tag{6-21}$$

by imposing the condition of equilibrium on an imaginary reference electrode and differentiating the resulting equation with respect to spatial variables:

$$\nabla \Phi = -\frac{1}{nF} \sum_{\mathrm{i}} s_{\mathrm{i}} \nabla \mu_i \tag{6-22}$$

Φ is the electric potential of the solution so defined, n is the number of electrons involved in the electrode reaction and s_i is the stoichiometric coefficient of species i in the reaction (where $s_i < 0$ for a product generated in the oxidation direction). By combining Eqs. (6-7) , (6-8), (6-9), the Gibbs-Duhem relation, electroneutrality condition and reaction charge balance ($s_+ z_+ + s_- z_- = -n$), one obtains an expression for the ionic current density [107]:

$$\mathbf{i} = -\varepsilon^{\gamma} \kappa \nabla \Phi - \frac{\varepsilon^{\gamma} \kappa}{F} \left(\frac{s_+}{n \nu_+} + \frac{t_+^0}{z_+ \nu_+} - \frac{s_0 c}{n c_0} \right) \nabla \mu_e \tag{6-23}$$

where κ is the ionic conductivity of the solution:

$$\kappa = -\frac{c_{\mathrm{T}} z_+ z_- F^2}{RT} \left(\frac{1}{\mathcal{D}_{+-}} + \frac{c_0 (1 - t_+^0)}{c_+ \mathcal{D}_{0-}} \right)^{-1} \tag{6-24}$$

Again, ε^{γ} in Eq. (6-23) is the correction coefficient for the ionic conductivity that accounts for porosity and tortuosity of the medium.

The constitutive equation for $\mathbf{v}_0$ is obtained as follows. The gradient of the chemical potential is related to the concentration gradient in the above equations according to:

$$\frac{1}{\nu RT} c \nabla \mu_e = \alpha \nabla c \tag{6-25}$$

where $\alpha = (1 + d\ln f_{\pm}/d\ln c)$ is the thermodynamic factor on a molar basis at constant pressure and temperature. The thermodynamic factor reflects the deviation of the solution from ideal behavior. As such, thermodynamic measurements are required for accurate characterization of concentrated solutions. A combination of the thermodynamic factor and cation transference number is retrieved from the "concentration polarization" data measured by way of concentration-cell experiments. After substituting Eq. (6-25) into Eq. (6-23) and applying the condition of zero current in a standard concentration-cell experiment (i.e., $\mathbf{i} = \mathbf{0}$ in Eq. (6-23)), one obtains an expression for the concentration polarization $\Gamma(c)$:

$$\Gamma = \frac{d\Phi}{d\ln c}\Big|_{\mathbf{i}=\mathbf{0}} = -\frac{\nu RT}{F}\left(\frac{s_+}{n\nu_+} + \frac{t_+^0}{z_+\nu_+} - \frac{s_0 c}{n c_0}\right)\alpha \tag{6-26}$$

The flux expressions given by Eqs. (6-8) and (6-9) are written in terms of the solvent velocity, whereas the continuity equation given by Eq. (6-5) is based on the mass-average velocity. Substitution of Eqs. (6-8), (6-9) and $\mathbf{N}_0 = c_0\mathbf{v}_0$ into the definition of the mass-average velocity Eq. (6-6) yields an expression relating $\mathbf{v}_0$ to $\mathbf{v}$:

$$\mathbf{v}_0 = \mathbf{v} + \frac{1}{\rho}\left(\left(\frac{\varepsilon^{\gamma}\mathcal{D}c_{\mathrm{T}}}{\nu RT c_0} c \nabla \mu_e\right) M_e - \frac{\mathbf{i}}{\nu_+ z_+ F}\left(\nu_+ M_+ t_+^0 - \nu_- M_-(1 - t_+^0)\right)\right) \tag{6-27}$$

At this point, the system of equations consists of four unknown scalar variables (c, Φ and the two components $\mathbf{v}_r$ and $\mathbf{v}_z$ of the velocity vector), but only three independent equations, i.e., Eqs. (6-4), (6-5) and (6-20). Therefore, in order to close the system of equations for the 2-D geometry of the cell, the momentum transport equation must be implemented [177]. Inclusion of the momentum balance equations for the radial and axial directions (two additional independent equations) introduces a fifth scalar variable, pressure p. In this way, the number of unknowns matches the number of independent equations and the system of equations is closed. This is seemingly at odds with our prior assumption of constant pressure throughout the cell. Although pressure is calculated using the model, its variation is so small ($O(10^{-3}$ Pa)) that its inclusion in the Stefan-Maxwell equations, equation of state and the Gibbs-Duhem relation does not provide meaningful improvement

to the estimates of the transport parameters. Therefore, these equations are taken to follow the assumption of constant pressure to avoid unnecessary intricacy.

It should be noted that in a 1-D system where the use of the equation of motion is not required (i.e., one-dimensional velocity vector), the volume-average velocity is usually preferred over the mass-average velocity as it leads to a simpler continuity equation often with an analytic solution. The case of a 1-D model based on the volume-average velocity is described elsewhere [31, 107, 112].

As described in section 6.2, a porous separator is used to confine the electrolyte inside the working volume of the cell. Darcy's law [179] provides a constitutive relation for the mass-average velocity across a porous medium in terms of the pressure gradient:

$$\mathbf{v} = -\frac{\mathrm{K}}{\mu}\nabla p \tag{6-28}$$

where K denotes the permeability of the porous medium (assumed isotropic) and μ is the dynamic viscosity of the solution. Note that gravity effects are ignored in this equation. For the cell described in this study, the flow is not caused by a pressure difference but rather by the electrochemical reaction at the working and counter electrodes. ∇p can therefore be regarded as a charge-transfer-induced (or "faradaic") pressure gradient. Consider that free convection due to local density variations (buoyancy effect) and electro-osmotic effect across the porous silicate separator are neglected in order to further simplify the model.

6.5.2 Boundary Conditions

The boundary conditions are derived in accordance with the charge transfer reaction Eq. (6-21) occurring at the WE, CE and PS, assuming identical electrode chemistries, as well as the symmetry at the centerline of the cell. Of course, the charge-transfer reactions differ if WE, CE and PS are of different chemical natures (e.g., intercalation electrodes). The molar flux of species i at the WE/electrolyte interface at $z = 0$ and the CE/electrolyte at $z = L$ is related to the current density generated by the reaction assuming negligible charging of electric double layer:

$$\mathbf{N}_i \cdot \hat{\mathbf{z}} = -\frac{s_i}{nF}\mathbf{i} \cdot \hat{\mathbf{z}} \tag{6-29}$$

where $\hat{\mathbf{z}}$ is the axial unit vector in the cylindrical coordinates. If species *i* is the only reacting species, then $\mathbf{N}_{j\neq i}$ vanishes at the boundary for all other species. It should be noted that boundary displacement due to electrochemical reactions at the WE and CE (e.g., in the case of metallic

electrodes) and the associated convection are very small under the operating conditions relevant to electrolyte characterization experiments and are thus ignored in this derivation. In cases where the boundary displacement is significant, the associated mathematical complication could be avoided by referring the species velocities to either the WE or CE surface rather than to a stationary frame of reference. However, this approach is valid only for a two-electrode cell configuration and breaks down for a multi-electrode configuration where the cell dimensions change upon boundary displacement. Moreover, under the assumption of constant partial molar volumes $\bar{V}_e$ and $\bar{V}_0$, which has been shown to be valid for a wide range of liquid solutions [107, 176], changes of the total volume due to concentration gradient development/relaxation become zero. As a result, the height of the electrolytic solution remains fixed and identical to the cell length and the associated convective effects vanish.

The current density is controlled externally by a potentiostat/galvanostat at $z = L$:

$$I_{\text{app}} = -2\pi \int_0^{R_{\text{cell}}} I_{\text{CE}} r dr \tag{6-30}$$

where I_{app} is the applied current, positive when the WE electrode at $z = 0$ undergoes an oxidation reaction while the CE at $z = L$ experiences a reduction reaction (i.e., $I_{\text{CE}} < 0$). R_{cell} is the radius of the cell and I_{CE} is the current density due to the charge-transfer reaction rate at the CE according to the Butler-Volmer equation:

$$\begin{aligned} I_{\text{CE}} = {} & nF\varepsilon k_{\text{CE}}^0 c^{1-\beta_{\text{CE}}}(1 \\ & - c_{\text{CE}})^{1-\beta_{\text{CE}}} c_{\text{CE}}^{\beta_{\text{CE}}} \left[\exp\left(\frac{(1-\beta_{\text{CE}})nF}{RT} (\Phi_{\text{CE}} - U_{\text{CE}} - \Phi) \right) \right. \\ & \left. - \exp\left(-\frac{\beta_{\text{CE}} nF}{RT} (\Phi_{\text{CE}} - U_{\text{CE}} - \Phi) \right) \right] \end{aligned} \tag{6-31}$$

where k_{CE}^0 is the reaction rate constant, β_{CE} is the charge-transfer coefficient, U_{CE} is the equilibrium potential of CE and c_{CE} is the concentration of the reacting species in the counter electrode (e.g., an intercalation/insertion electrode). If the counter electrode is a pure metal and no intercalation reaction occurs, then c_{CE} is irrelevant. U_{CE} is zero if the counter electrode is identical to the imaginary reference electrode used to define the solution potential. Φ_{CE} is the electric potential of the counter electrode and is obtained using Eq. (6-31). Eq. (6-31) also represents the current density of the charge-transfer reaction at the working electrode (in this case, the subscript WE is used instead of

CE). Charge is conserved and the integral boundary condition at $z = L$ guarantees that the total current entering/leaving the working electrode at $z = 0$ is equal to I_{app} as well. As the second boundary condition, it is convenient to set the working electrode potential to zero, i.e., $\Phi_{\text{WE}} = 0$, and to calculate the solution potential adjacent to the WE from the Butler-Volmer equation. It is justified by the fact that the electric potential of the electrode should remain uniform due to its high electronic conductivity. Multiplying Eq. (6-29) by M_i and adding over all species and dividing by ρ yields the boundary condition for velocity at $z = L$:

$$\mathbf{v} \cdot \hat{\mathbf{z}} = -\frac{\sum_i s_i M_i}{\rho n F} \mathbf{i} \cdot \hat{\mathbf{z}} \tag{6-32}$$

The pressure at $z = 0$ is arbitrarily set to zero as the second boundary condition for the equation of momentum conservation. From axial symmetry, the radial components of the species flux densities, mass-averaged velocity and the current density are zero at the centerline of the cell:

$$\begin{aligned} \mathbf{N}_i \cdot \hat{\mathbf{r}} &= 0 \; at \; r = 0 \\ \mathbf{v} \cdot \hat{\mathbf{r}} &= 0 \; at \; r = 0 \\ \mathbf{i} \cdot \hat{\mathbf{r}} &= 0 \; at \; r = 0 \end{aligned} \tag{6-33}$$

where $\hat{\mathbf{r}}$ is the radial unit vector.

6.5.3 Potential Sensors

As described in the previous subsection, the potential difference between two infinitesimal reversible electrodes can describe the electrical state of the solution. Since a real reference electrode has a finite length, some ambiguities regarding the spatial resolution of the measured solution potential may exist. Since each potential sensor is not connected to a sink/source of current, the overall charge transferred across the entire sensor/electrolyte interface is zero. In the case of a metallic (i.e., good electronic conductor) electrode, a "bipolar effect" takes place whereby anodic and cathodic reactions occur simultaneously at different locations over its surface depending on the electrolyte potential profile [173]. Each potential sensor is assumed to have a uniform electric potential due to its high conductivity. The charge-transfer reaction that occurs locally at the sensor/electrolyte interface can also be described by the Butler-Volmer equation:

$$I_{\mathrm{PS},l} = nF\varepsilon k_{\mathrm{PS}}^{0} c^{1-\beta_{\mathrm{PS}}}(1 - c_{\mathrm{PS}})^{1-\beta_{\mathrm{PS}}} c_{\mathrm{PS}}^{\beta_{\mathrm{PS}}} \left[\exp\left(\frac{(1-\beta_{\mathrm{PS}})nF}{RT}\left(\Phi_{\mathrm{PS},l} - U_{\mathrm{PS}} - \Phi\right)\right) - \exp\left(-\frac{\beta_{\mathrm{PS}} nF}{RT}\left(\Phi_{\mathrm{PS},l} - U_{\mathrm{PS}} - \Phi\right)\right)\right] \tag{6-34}$$

where $I_{\mathrm{PS},l}$ is the charge transfer rate per unit area of the potential sensor l, k_{PS}^{0} is the kinetic rate constant, β_{PS} is the charge transfer coefficient and $\Phi_{\mathrm{PS},l}$ is the potential of the electrode. Note that the PS are chosen to be chemically and geometrically identical. U_{PS} is the electrode equilibrium potential versus the imaginary reference electrode used to define the solution potential and is zero if the solution potential is defined based on the same electrodes as actually used as the potential sensors. c_{PS} is the concentration of the reacting species in the potential sensor (e.g., an intercalation electrode) and is irrelevant in Eq. (6-34) if a pure metal is used as the potential sensor.

The condition of zero net charge transfer at the electrode/electrolyte interface requires the following constraint to hold:

$$\int_{A_{\mathrm{PS}}} I_{\mathrm{PS},l}\, dS = 0 \tag{6-35}$$

where A_{PS} is the area of the sensor/electrolyte interface over which the charge-transfer reaction occurs. For an annular electrode, $dS = 2\pi R_{\mathrm{cell}} dz$. An immediate implication of this constraint is that the local charge-transfer reaction must change direction from cathodic to anodic at some locus $z_{\mathrm{eq},l}$ connecting the cathodic and the anodic poles of the potential sensor. At this location, the polarization is zero (i.e., $\Phi_{\mathrm{PS},l} - \Phi = 0$ given $U_{\mathrm{PS}} = 0$) and the electrode potential becomes equal to the electric potential of the adjacent solution. Since the electrode is conductive, its electric potential $\Phi_{\mathrm{PS},l}$ is spatially uniform and is equal to the solution potential at $z_{\mathrm{eq},l}$. As a result, the potential difference $\Phi_{\mathrm{PS},2} - \Phi_{\mathrm{PS},1}$ unambiguously measures the difference in the solution potential at certain positions in the cell, i.e., at $z = z_{\mathrm{eq},2}$ and $z = z_{\mathrm{eq},1}$ at $r = R_{\mathrm{cell}}$.

$\Phi_{\mathrm{PS},l}$ and the corresponding equilibrium locus between the anodic and cathodic poles of each PS is found by solving Eq. (6-35) based on $I_{\mathrm{PS},l}$ being determined by equating Eq. (6-34) to the radial component of the ionic current density at the surface of PS,1. Current density is zero over inert interfaces in the cell. Thus the boundary condition for Eq. (6-4) at $r = R_{\mathrm{cell}}$ reads:

$$\mathbf{i}\cdot\hat{\mathbf{r}} = \begin{cases} -I_{\mathrm{PS},1}, & z \in [\lambda, \lambda+\delta\,] \\ -I_{\mathrm{PS},2}, & z \in [L-(\lambda+\delta), L-\lambda\,] \\ 0, & \text{otherwise} \end{cases} \tag{6-36}$$

where λ is the spacing between the PS and WE/CE and δ is the thickness of the PS. The negative sign signifies that $\mathbf{i}.\hat{\mathbf{r}}$ is positive on the cathodic pole where reduction occurs (i.e., $I_{\mathrm{PS},l} < 0$) and is negative on the anodic pole where oxidation occurs (i.e., $I_{\mathrm{PS},l} > 0$). Boundary conditions similar to Eq. (6-29) and Eq. (6-32) hold for $\mathbf{N}_i$ and $\mathbf{v}$, respectively, at $r = R_{\mathrm{cell}}$:

$$\mathbf{N}_i\cdot\hat{\mathbf{r}} = -\frac{s_i}{nF}\mathbf{i}\cdot\hat{\mathbf{r}} \tag{6-37}$$

$$\mathbf{v}\cdot\hat{\mathbf{r}} = -\frac{\sum_i s_i M_i}{\rho nF}\mathbf{i}\cdot\hat{\mathbf{r}} \tag{6-38}$$

Because of the bipolar effect, the potential sensors locally perturb the concentration and potential of the electrolyte which, in turn, affects the measured potential difference. The simple case of a solution exposed to a constant electric field with zero local perturbation is discussed in Appendix A.

Figure 6-3 shows the schematics of the computation domain with the governing equations and the associated boundary conditions listed.

The solute concentration is the only variable for which an initial value must be known to obtain a unique transient solution to the problem. Accordingly, the concentration is set to the nominal concentration of the as-received electrolyte, ignoring effects due to side reactions during the cell conditioning and temperature.

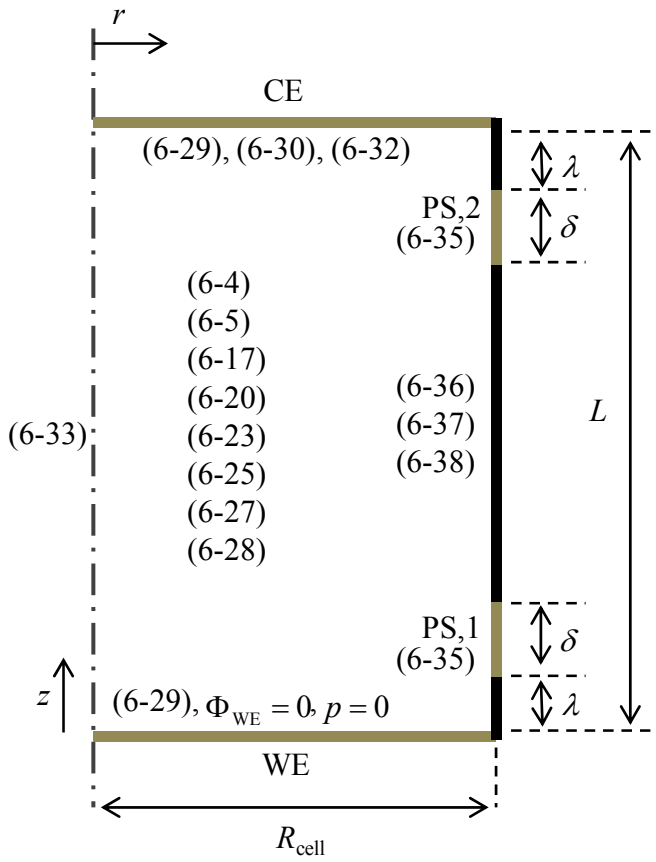

Figure 6-3. Schematic view of the computation domain and the list of governing equations and boundary conditions. The lengths are not to scale in drawing.

6.5.4 Solution Method

The coupled system of partial differential equations consisting of Eqs. (6-4), (6-5), (6-17), (6-20), (6-23), (6-25), (6-27) and (6-28) and the corresponding boundary conditions is numerically solved using the finite-element-based COMSOL Multiphysics simulation package. The 2-D axi-symmetric solution domain is discretized into unstructured triangular meshes controlled by specified distributions on the domain boundaries. The boundaries along the dimensionless cell radius are discretized into 20 elements distributed according to an arithmetic sequence with the smallest element adjacent to the cell wall being half the largest one at the symmetry axis $r = 0$. The domain boundary along the cell wall consists of five segments: two potential sensors and three inert walls. Along each potential sensor the boundary is uniformly divided into 40 elements. Such a high mesh density is used to assure accuracy as FEM is not a conservative numerical method in nature. The two shorter inert boundaries corresponding to the WE/CE-PS spacers are discretized into 10 elements shrinking

towards the outer edges of the PS with a largest to smallest ratio of 0.05 whereas the larger inert boundary corresponding to the spacer between the two PS is divided into 40 elements symmetrically distributed with a size ratio of 0.05 and the largest one located in the middle. Time stepping is performed using an adaptive backward difference scheme with a maximum order of 5. The resulting linear algebraic equations are solved in each time step using the multifrontal massively parallel sparse direct solver (MUMPS) algorithm embedded in COMSOL Multiphysics.

6.6 Results and Discussion

In order to demonstrate the effectiveness of the proposed cell design and the method for estimating the transport properties, it is applied to two non-aqueous electrolytic solutions—a 1 molar solution of $LiPF_6$ in a EC/DEC (1:1 vol.) mixed solvent and a 1 molar solution of the same salt in a EC/DMC (1:1 vol.) mixed solvent, as described in 'Experimental' and the results shown in Figure 6-4. General model parameters used for the simulations are listed in Table 6-1. The same set of thermodynamic data as reported in the literature for 1M $LiPF_6$ in 1:1 wt. EC/DEC is used to characterize both electrolytes (due to lack of thermodynamic data for the EC/DMC system) [43]. It is a reasonable assumption as the literature reports show that the thermodynamic factor values does not vary significantly for electrolytes of the same solute (i.e., $LiPF_6$) but different solvents (see figure 10 of Ref. [180]). The estimated transport properties for the two electrolytes are summarized in Table 6-2 and Table 6-3. The method used to obtain these values is discussed in detail in the following section. The estimated transport parameters compare favorably with those recently reported in the literature for the similar system of 1M $LiPF_6$ in 1:1 wt. EC/DEC ($\kappa = 0.79\ \mathrm{S\ m^{-1}}$, $\mathcal{D} = 1.377\ \mathrm{m^2\ s^{-1}}$ and $t_+^0 = 0.162$ at $c = 1\ \mathrm{mol\ L^{-1}}$ with faradaic convection included) [43].

Table 6-1. Model parameter used for the simulations at 25℃ .

Parameter	Symbol	Value
Cell length (m)	L	$4.747 \times 10^{-3\mathrm{m}}$
Cell radius (m)	R_{cell}	$6.49 \times 10^{-3\mathrm{m}}$
Porosity	ε	0.92^{c}
Bruggeman exponent	γ	3.44 [39]

Working electrode/potential sensor spacing (m)	λ	$7.56 \times 10^{-4\mathrm{m}}$
Potential sensor width (m)	δ	$1.91 \times 10^{-4\mathrm{m}}$
Number of species in the solution	N	3^{a}
Temperature (K)	T	298.15^{m}
Number of cations in one molecule of salt	ν_+	1^{a}
Number of anions in one molecule of salt	ν_-	1^{a}
Cation charge number	z_+	1^{a}
Anion charge number	z_-	-1^{a}
Stoichiometric coefficient of cation in reversible electrode reaction	s_+	-1^{a}
Stoichiometric coefficient of anion in reversible electrode reaction	s_-	0^{a}
Stoichiometric coefficient of solvent in reversible electrode reaction	s_0	0^{a}
Number of electron in charge-transfer reaction	n	1^{a}
Charge-transfer rate constant, $q = \mathrm{WE, CE, PS}$ ($\mathrm{mol}^{\beta_q}\ \mathrm{m}^{1-3\beta_q}\ \mathrm{s}^{-1}$)	k_q^0	7×10^{-6} [162]
Charge transfer coefficient, $q = \mathrm{WE, CE, PS}$	β_q	0.5^{a}
Potential sensor equilibrium potential vs. reference electrode used to define electrolyte potential, $q = \mathrm{WE, CE, PS}$ (V)	U_q	0^{a}
Molecular weight of Li^+ ($\mathrm{g\ mol}^{-1}$)	M_+	6.94^{a}
Molecular weight of PF_6^+ ($\mathrm{g\ mol}^{-1}$)	M_-	144.96^{a}
Molecular weight of EC/DEC solvent ($\mathrm{g\ mol}^{-1}$)	M_0	100.9^{a}
Partial molar volume of LiPF_6 in EC/DEC ($\mathrm{m}^3\ \mathrm{mol}^{-1}$)	$\bar{V}_e$	56.8×10^{-6} [43]
Partial molar volume of EC/DEC solvent	$\bar{V}_0$	90.8×10^{-6} [43]

(m^3 mol^{-1})		
Dynamic viscosity of 1 M $LiPF_6$ in EC/DEC (Pa.s)	μ	4.6×10^{-3} [43]
Permeability of separator (m^2)	K	3.96×10^{-12c}
Concentration polarization at $c = 1000$ mol m^{-3} (V)	Γ	0.0702 [43]

[m]: measured; [c]: calculated; [a]: assumed;

6.6.1 Parameter Estimation

The proposed parameter estimation method relies on numerically solving the mathematical model presented in the previous section and comparing the simulation results to the experimental data (i.e., $|\Phi_{PS,2} - \Phi_{PS,1}|$) obtained in the four-electrode cell in response to a single rectangular pulse wave. Three transport properties, namely, κ, $\mathcal{D}$ and t_+^0, are estimated for a concentrated binary electrolyte at any given concentration. Transport properties are estimated at the nominal concentration of the as-received electrolyte, i.e., at $c = 1$ mol L^{-1}, and are assumed to remain constant throughout the experiment for simplicity.

In previous methods, distinctive features in the electrode responses from various experiments are collected: i) intersection of the high-frequency data with the real-axis of a Nyquist plot in an AC impedance measurement to estimate the ionic conductivity, ii) decay in the OCV of a symmetric cell with time in the restricted diffusion experiment to determine the chemical diffusion coefficient [112] and iii) OCV measurement immediately after current interruption as a function of $It_i^{1/2}$ (t_i: interruption time) in a semi-infinite diffusion experiment to measure the transference number [31, 118].

Prior to be fitted by the model, both closed-circuit and open-circuit voltages across the potential sensors are assessed carefully for features that uniquely manifest the effect of each of the unknown parameters. It is to assure unique parameter estimates. Analogous to the semi-infinite diffusion method, the closed-circuit voltage (CCV) responses to three different applied currents are plotted as a function of $t^{1/2}$ in Figure 6-4b and e. The closed-circuit response demonstrates two distinct stages: i) the onset of the process where $|\Phi_{PS,2} - \Phi_{PS,1}|$ remains constant followed by ii) an increase in the potential difference that gradually levels near the end of the closed-circuit operation. It

should be noted that the attainment of steady-state is not necessary for the analysis according to our proposed method.

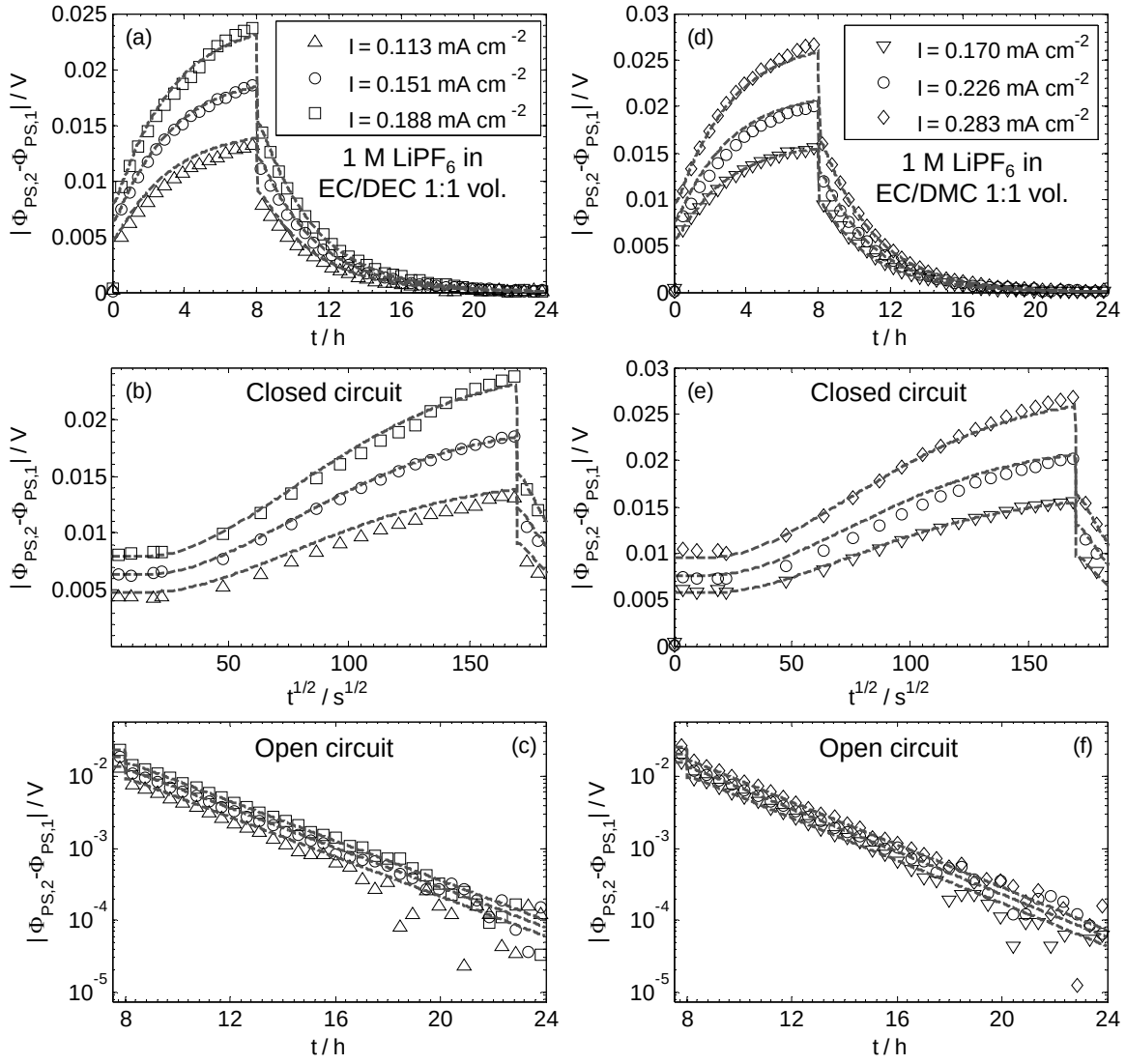

Figure 6-4. Potential versus (a, d) t and (b, e) $t^{1/2}$ during closed-circuit portion of galvanostatic pulse; (c, f) semi-logarithmic plot of potential versus t during open-circuit portion of a galvanostatic pulse. The markers indicate experimental data and the lines are data computed using the model. Plots in (a) to (c) correspond to 1 M $LiPF_6$ in EC/DEC and plots in (d) to (f) to 1 M $LiPF_6$ in EC/DMC.

In Figure 6-4c and f, the potential decay during the open-circuit portion of the galvanostatic pulse is plotted on a semi-logarithmic scale versus time. The experimental measurements take the form of a straight line in both electrolytes over the whole relaxation period.

The constant-voltage stage at the onset of CCV (Figure 6-4b and e) corresponds to a short time delay required for the concentration gradients generated at the working and counter electrodes to reach the potential sensors. In other words, the PS do not sense potential differences due to concentration variations in the cell so that the recorded voltage is determined principally by ion migration. After this period, the closed-circuit potential begins to increase as a result of the concentration gradient slowly propagating across the sensors and toward the center of the cell. The measured potential during this stage is affected by both migration and diffusion which cannot be directly separated. The exponential decay of the potential during the response to the open-circuit portion of the pulse is attributed solely to diffusion [112].

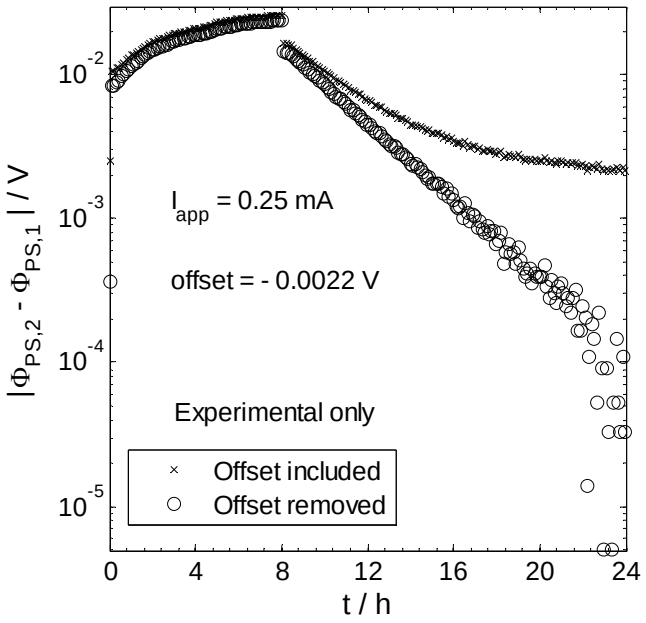

Figure 6-5. Semi-logarithmic plot of experimental potential differences for the $LiPF_6$/EC/DEC system obtained during the closed-circuit and open-circuit before (crosses) and after (circles) correction for the observed non-zero offset.

It is worthwhile to note that the linearity of data in the semi-logarithmic graph (i.e., characteristic of diffusive decay) is recovered by removing a non-zero offset from both the closed-circuit and open-circuit data (Figure 6-5). The voltage offset is an instrumental artifact which distorts

experimental data. The magnitude and sign of the voltage offset vary for each cycle and so each set of experimental data is corrected by the corresponding offset (e.g., -1.55 mV for cell polarization at $I_{\text{app}} = 0.15$ mA, -0.2 mV at $I_{\text{app}} = 0.2$ mA and -2.2 mV at $I_{\text{app}} = 0.25$ mA in the $LiPF_6$/EC/DEC system).

Parameter estimation is conducted in three steps. In the first step, the ionic conductivity is estimated by manually adjusting it so that the model fits the experimental data during the initial constant-voltage stage of the closed-circuit response which is affected only by ionic migration. In the second stage, the chemical diffusion coefficient (on molar scale)

$$D = \frac{c_{\text{T}}}{c_0}\alpha\mathcal{D} \tag{6-39}$$

is estimated from the open-circuit data by fitting the model to the slope of the straight line in the semi-logarithmic plot of voltage versus time (Figure 6-4c and f) in agreement with the restricted-diffusion method. The term α in Eq. (6-39) is related to the as-received concentration-cell data according to Eq. (6-26):

$$\alpha = \frac{F}{2RT(1-t_+^0)}\Gamma \tag{6-40}$$

With the ionic conductivity κ and chemical diffusion coefficient D already estimated in steps 1 and 2 and the concentration polarization Γ available from the concentration-cell experiment, the transference number t_+^0 is determined in the last step by fitting the model to the transient portion of the closed-circuit data which is affected by the three transport properties. In the case of a non-zero solvent velocity where convective transport is also operative, the chemical diffusion coefficient and transference number may have to be finely tuned simultaneously at the end of the fitting process. Finally, the thermodynamic factor α and thermodynamic diffusion coefficient $\mathcal{D}$ are calculated using Eqs. (6-39) and (6-40), respectively. It should be noted that solution density measurements (i.e., the partial molar volumes) are necessary for calculating the thermodynamic diffusion coefficient. If values of the partial molar volumes are unavailable, as in the case of the $LiPF_6$/EC/DMC system, the method directly reports the chemical diffusion coefficient, which is sufficient for most battery modeling applications. Moreover, it is not possible to account for faradaic convection if the partial molar volumes are not known. Figure 6-6 summarizes the parameter estimation scheme proposed in this research.

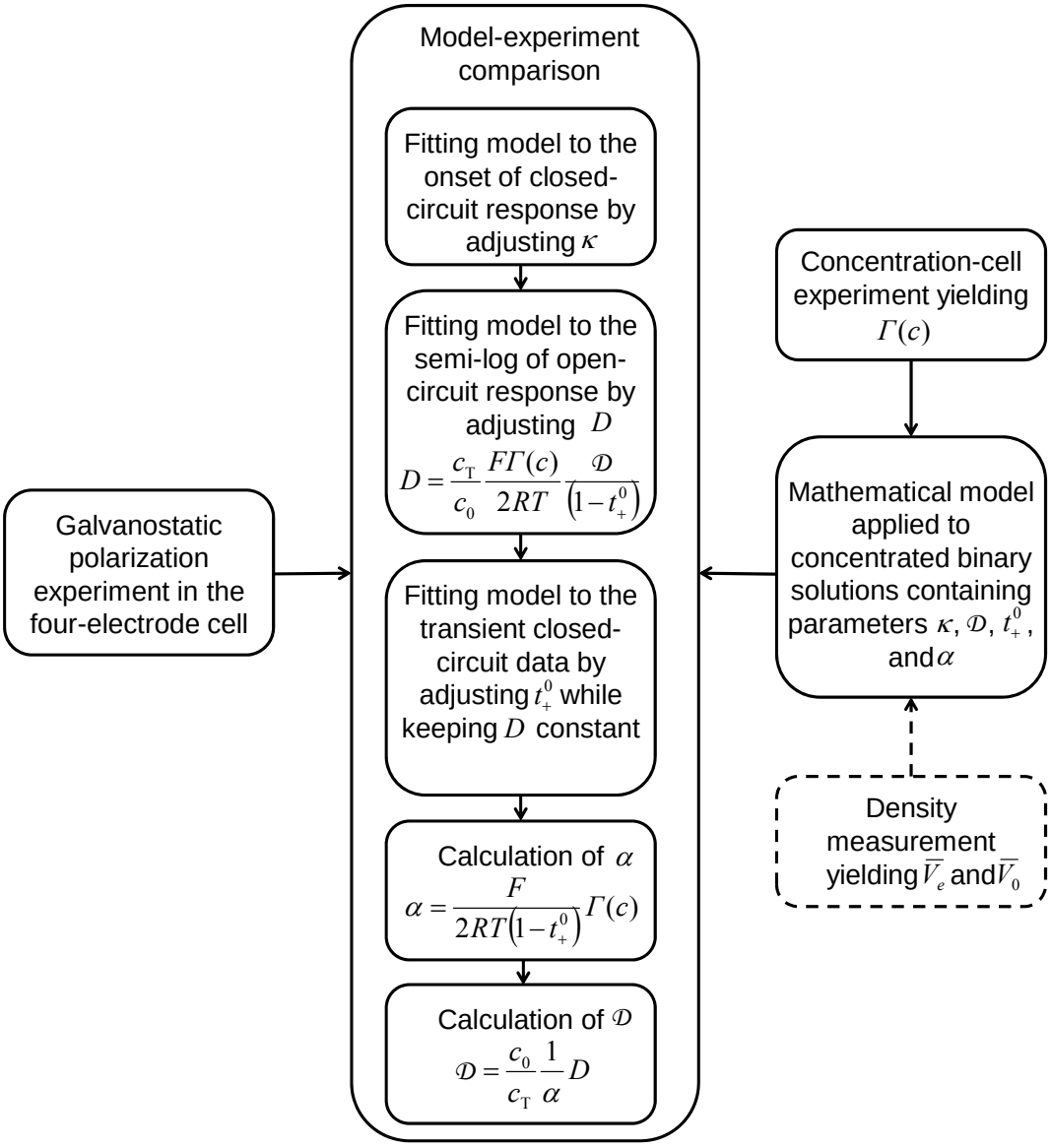

Figure 6-6. Flowchart of the methodology proposed in this study for the estimation of transport and thermodynamic properties of concentrated binary electrolytes.

The fitting process is carried out manually according to the above guidelines only for one galvanostatic pulse experiment ($0.151\ \text{mA cm}^{-2}$ and $0.226\ \text{mA cm}^{-2}$ for $LiPF_6$/EC/DEC and $LiPF_6$/EC/DMC, respectively) and the resulting parameter estimates are used to simulate the response of the cell at other applied currents to test the robustness of the method. The fitting procedure

described above is demonstrated by performing a sensitivity analysis on the transport properties of the $LiPF_6$/EC/DEC system as shown in Figure 6-7. The ionic conductivity shifts the CCV upward or downward (Figure 6-7a), chemical diffusion coefficient (i.e., $\mathcal{D}$ with constant t_+^0) affects the slope of semi-logarithmic OCV (Figure 6-7b) and the transference number modifies the transient portion of CCV while D (i.e., according to Eqs. (6-39) and (6-40)) is constant (Figure 6-7c and d).

Table 6-2. Transport properties estimated for a 1 M solution of $LiPF_6$ in EC/DEC (1:1 vol.) at 25°C. Concentration polarization data used here are taken from Ref [43] for a 1 M solution of $LiPF_6$ in EC/DEC (1:1 wt.).

Parameter	Symbol	$\mathbf{v}_0 \neq \mathbf{0}$	$\mathbf{v}_0 = \mathbf{0}$
Ionic conductivity (S m^{-1})	κ	0.95	0.95
Diffusion coefficient based on a thermodynamic driving force (m^2 s^{-1})	$\mathcal{D}$	1.24×10^{-10}	1.10×10^{-10}
Chemical diffusion coefficient (m^2 s^{-1})	D	2.6×10^{-10}	2.45×10^{-10}
Transference number with reference to solvent velocity	t_+^0	0.223	0.267
Thermodynamic factor	α	1.758	1.864

The model-predicted results compare very well with the experimental data at all applied currents for both electrolytes (Figure 6-4). Discrepancies between the simulation results and experimental data can be attributed to errors associated with the model assumptions, numerical solution or the experiment itself. The first type of error occurs when the model assumptions and the operating conditions are not in a perfect agreement (e.g., transport properties independent of concentration); the second can arise when the numerical solution is mesh or time-step dependent; The third source of error can be related to the accuracy of the potentiostat/galvanostat used to measure the potential (i.e., 0.1% of FSR equivalent to ± 0.2 mV), non-uniformity or localized nature of the charge-transfer reaction at the WE and CE surfaces and the measurement of cell dimensions, porosity and tortuosity. The use of a precision multimeter, modification of the WE and CE (e.g., using intercalation electrodes in place of metallic ones) and accurate measurement of cell dimensions and tortuosity, among others, are expected to minimize possible errors in parameter estimates. Estimation errors are best quantified when an appropriate numerical scheme is used for the fitting procedure.

Table 6-3. Transport and thermodynamic properties of 1 M $LiPF_6$ in EC/DMC (1:1 vol.) at 25°C. Concentration polarization data used here are taken from Ref. [43] for a 1 M solution of $LiPF_6$ in EC/DEC (1:1 wt.).

Parameter	Symbol	$\mathbf{v}_0 = \mathbf{0}$
Ionic conductivity (S m^{-1})	κ	1.19
Chemical diffusion coefficient (m^2 s^{-1})	D	2.66×10^{-10}
Transference number with reference to solvent velocity	t_+^0	0.425
Thermodynamic factor	α	2.32

Experimental errors and those associated with model assumptions also exist with the conventional parameter estimation methods. Combination of information from piecewise experiments each conducted under strict operating conditions to meet the model assumptions (which are difficult to realize in practice) and accompanied by an exceedingly simplified though analytically solvable model, increases the chance for large systematic errors to land in the parameter estimates. These systematic errors are further discussed later. Therefore, significant discrepancies exist among the transport property values reported in the literature for similar electrolytes [31-44].

The uniqueness of the fitted transport properties obtained using the proposed method can be further justified by resorting to discussions on the semi-infinite diffusion method. It will be shown that the closed-circuit portion of the galvanostatic pulse experiment replaces the semi-infinite diffusion experiments by producing a set of data orthogonal to those obtained from the open-circuit portion of the same experiment and those from the concentration-cell experiment.

The semi-infinite diffusion analysis involves the analytical solution of a simplified conservation of mass equation during galvanostatic polarizations at different combinations of pulse current and duration. It also requires linearization of the modified ohm's law in the absence of current in order to relate the voltage to the concentration at the two ends of a cell. As such, the cell voltage (i.e., $\Phi_{\mathrm{WE}} - \Phi_{\mathrm{CE}}$ in a two-electrode cell) measured immediately after the current interruption is reflective of the difference between the bulk concentration and that adjacent to the WE surface [31, 118]. Indeed, the closed-circuit voltage measured in the four-electrode cell is nothing but the

superposition of ohmic and concentration polarizations. Therefore, the CCV curve contains the same information as that generated by the semi-infinite diffusion experiment. Hence, CCV data can be used to estimate the transference number in the same way that semi-infinite diffusion data (i.e., potential differences versus $It_i^{1/2}$ where t_i is the interruption time) are used, given that the ionic conductivity is known.

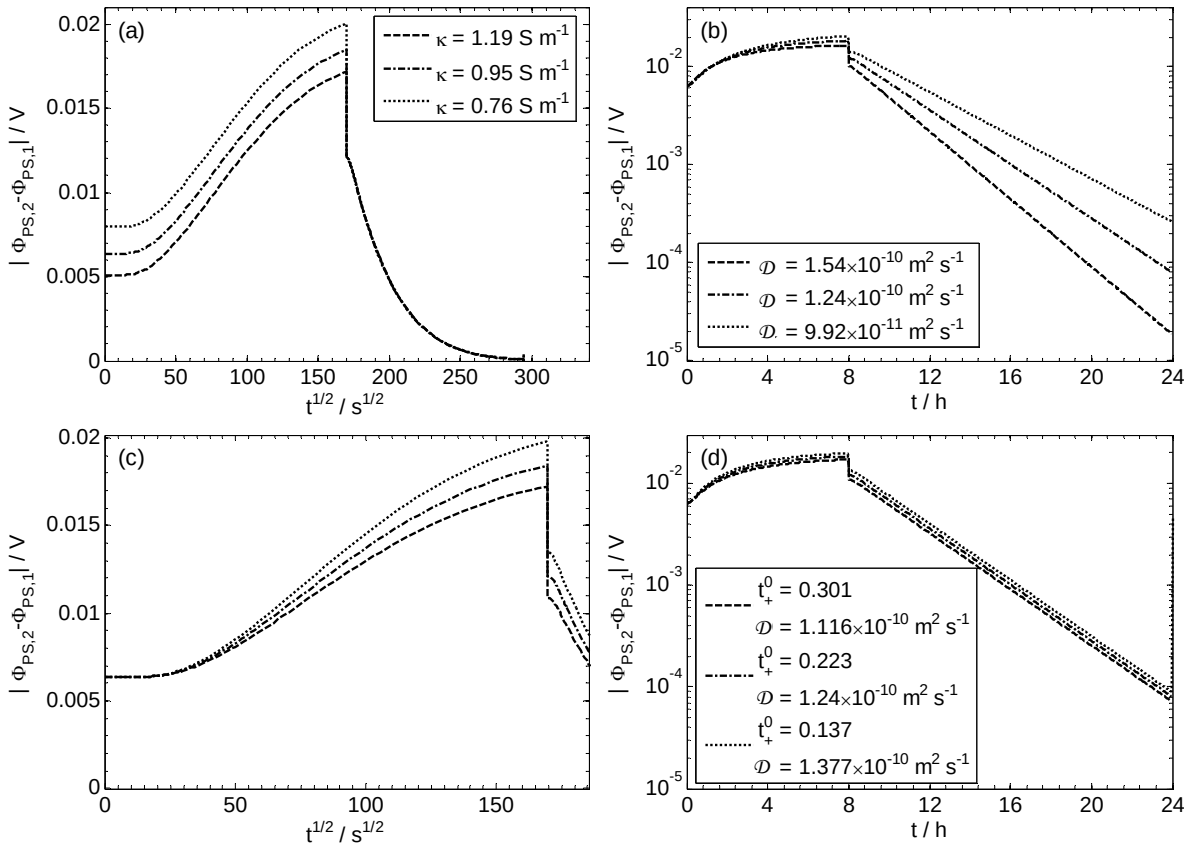

Figure 6-7. Sensitivity analysis of the model to (a) bulk ionic conductivity of the solution, (b) diffusion coefficient with respect to thermodynamic driving force, (c) and (d) transference number. (c) and (d) share the same legends that are shown in (d). Model parameters are given in Table 6-1 and Table 6-2 except those varied (see legend).

The actual voltage measured immediately after the current interruption in the semi-infinite diffusion method is prone to error due to double-layer relaxation and other effects at the electrode/electrolyte interface. Therefore, it is necessary to extrapolate experimental data recorded at $t > t_i$ to $t = t_i$ (i.e., linear with respect to the so-called "reduced time" $\tau = \sqrt{t}/(\sqrt{t} - \sqrt{t_i})$ where t_i

is the interruption time) to obtain a voltage value at the interruption time suitable for transference number estimation [118]. This linear extrapolation is allowed providing that the system perfectly satisfies the semi-infinite condition and that the concentration polarization Γ is constant (i.e., valid for sufficiently small concentration differences) [119]. The same assumptions underlie the linearity of potential versus $It_i^{1/2}$ as $It_i^{1/2}$ approaches zero. The slope of the potential-$It_i^{1/2}$ curve is at the heart of the semi-infinite diffusion method and any error in obtaining its value (i.e., whether it is generated at the voltage measurement step, extrapolation step or the linear regression step) will propagate into the final estimates of the transference number, diffusion coefficient (thermodynamic and chemical) and thermodynamic factor. The semi-infinite diffusion method is therefore limited to narrow experimental conditions of small $It_i^{1/2}$ to comply with the underlying semi-infinite condition and constant Γ. However, these conditions are difficult to meet in practice since large potential signals are required for the measurements not to be distorted by noise.

The new four-electrode method being proposed bypasses the need for semi-infinite diffusion experiments and the complications associated with parameter estimation described above by directly analyzing the closed-circuit data. In fact, a plot of the open-circuit potential after current interruption versus $It_i^{1/2}$ is not required to estimate the transference number. Instead, it is obtained by fitting the model to the closed-circuit voltage-time data. Measurement of CCV data at the potential sensors essentially obviates the need for any extrapolation required in the conventional semi-infinite diffusion method. Furthermore, continuous measurement of CCV data in the proposed method provides as many reliable data points as the potentiostat/galvanostat can record. The abundance of the reliable CCV data points as compared to the data points used in the conventional semi-infinite diffusion method (i.e., only a few) significantly reduces the error associated with curve fitting. Moreover, relaxation of the core assumptions of the semi-infinite diffusion experiment and numerical solution of the transport model make possible the analysis of data at larger t.

The condition of small $It_i^{1/2}$ in the conventional semi-infinite diffusion method is not only required to satisfy the semi-infinite diffusion condition but also to comply with the assumption that the variations of transport properties and thermodynamic factor with concentration are insignificant (i.e., constant solution properties at their bulk values). The same assumption is considered in the restricted diffusion method which is valid at sufficiently large times after the current interruption when the concentration profile levels off. The chemical diffusion coefficient so estimated corresponds

accurately to the bulk concentration and is so-called "differential" chemical diffusion coefficient [112].

In the case of our four-electrode method, the assumption of constant properties is not required. Numerical solution of the complete transport model permits concentration-dependent transport properties to be estimated if electrolyte samples at different concentrations are prepared and separately examined in the four-electrode cell. Such a comprehensive analysis is beyond the scope of this thesis and will be presented in a future publication. As such, the assumption of constant properties made here is merely for the sake of simplicity.

6.6.2 Convection

Faradaic convection (i.e., convective transport of species induced by charge-transfer reactions at the working and counter electrodes) is accounted for in the model by solving for the mass-average velocity. However, the diffusion of species is referred to the solvent velocity when inverting the force-explicit Stefan-Maxwell equations Eq. (6-7) into flux expressions Eqs. (6-8) and (6-9). This formulation resembles that used in most electrochemical battery models to describe the potential losses associated with species transport in the electrolyte [108]. Nonetheless, in almost all of these battery models, the solvent velocity is set to zero and faradaic convection is neglected to simplify the model. Despite their accuracy, the transport and thermodynamic properties determined with convection included are not compatible with an electrochemical battery model where convective mass transport is ignored.

Figure 6-8 shows simulated voltage responses to a galvanostatic pulse assuming the solvent velocity is zero (dashed lines) or allowed to be non-zero (dashed-dotted lines) using the same set of transport properties estimated for the $LiPF_6$/EC/DEC system for the case of $\mathbf{v_0} \neq \mathbf{0}$ (Table 6-2). Exclusion of the convective terms from the flux expressions causes an overestimation of the rate of relaxation of the concentration profile, i.e., leads to a steeper decay of voltage with time in Figure 6-8b. A decrease in $\mathcal{D}$ by ~ 11.1% and increase in t_+^0 by ~ 19.7% are required for the simulations conducted with $\mathbf{v_0} = \mathbf{0}$ to coincide with those obtained with $\mathbf{v_0} \neq \mathbf{0}$. Thus, neglect of faradaic convection leads to an overestimate of $\mathcal{D}$ and an underestimate of t_+^0. Such a significant discrepancy suggests that faradaic convection may not be negligible in electrolytic solutions regularly used in Li-ion batteries. Therefore, when using the parameter values given in Table 6-3, it is important that the electrochemical model in which these parameters are to be used be consistent with the model from

which they were obtained in the first place. The foundation of the conventional restricted and semi-infinite diffusion methods is critically discussed and revisited to include convection effects in Refs. [119] and [177].

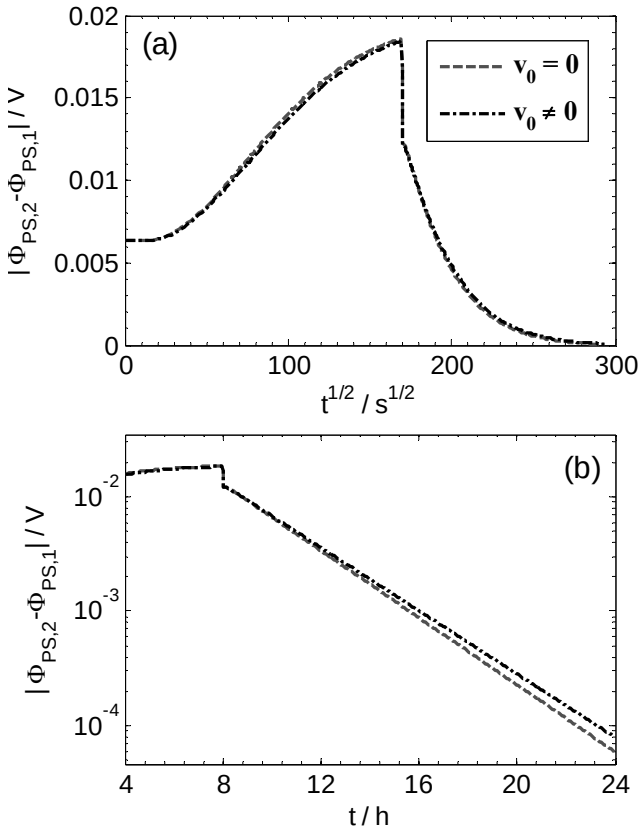

Figure 6-8. Simulation results for $LiPF_6$/EC/DEC at $I_{app} = 0.2$ mA excluding (dashed lines) or including (dashed-dotted lines) faradaic convection. (a) Potential difference between the two PS versus $t^{1/2}$ and (b) semi-logarithmic plot of potential difference versus time. The set of transport properties is estimated based on the model with $v_0 \neq 0$ (Table 6-2).

The system is assumed to exist in a state of mechanical equilibrium where only external forces can cause a pressure gradient in the solution. Neglecting the effect of gravity, the only body force is related to the resistive interaction between the liquid solution and the solid matrix in the porous separator. This resistive force is manifested in the permeability that appears in the Darcy's law implemented in the model [179]. The momentum equation is used here solely to close the system of equations in our 2-D model. It involves the calculation of pressure gradient which is commonly assumed not to affect mass transport even in concentrated solutions [107, 176]. However, it is of

value to estimate the extent of pressure variations within the cell during the galvanostatic polarization experiments conducted in this research. To this end, the permeability of the separator is determined using the modified Gebart relation, an empirical equation that has been shown to be accurate for highly porous binder-free fibrous media [181]:

$$\frac{\mathrm{K}}{r^2} = 0.491\left(\sqrt{\frac{1-0.0743}{1-\varepsilon}}-1\right)^{2.31} \tag{5-1}$$

where K is the permeability of the medium (assumed isotropic) and r is the fiber radius. The validity of using a scalar value for the permeability instead of a tensor for isotropic fibrous porous media was demonstrated in Ref. [181]. The fiber radius is estimated to be ~ 1 μm from a SEM micrograph of Whatman filter grade GF/C [182] (GF/C is less permeable than GF/D). With this value of r and the known porosity of the separator (Table 6-1), the permeability of the separator is calculated from the modified Gebart relation to be 3.96×10^{-12} m^2. The maximum pressure difference along the cell filled with the $LiPF_6$/EC/DEC solution at the applied current of $I_{\mathrm{app}} = 0.2$ mA is ~ 4.4×10^{-3} Pa (calculated from the simulation results) which is very small as expected and is unlikely to have a significant impact on the thermodynamics of the solution.

6.6.3 Bipolar Effect

A bipolar effect can take place when a local charge-transfer reactions occur on an isolated conductive object (i.e., not connected to a power supply) with a finite length in contact with an electrolytic solution that is exposed to an electric field. The potential sensors in the four-electrode cell act as "bipolar electrodes" on which reduction and oxidation reactions occur simultaneously at their cathodic and anodic poles, respectively, in such a way that the net faradaic current over the surface of the electrode is zero. The production and consumption of the reacting species perturb the concentration profile in vicinity of the sensors which may introduce a systematic error in the parameter estimation if not included in the model. Due to the small current applied, the bipolar effect is expected to be very small in the four-electrode cell; however its impact on the recorded potentials must be carefully investigated to gain insight about the cell design prior to considering possible simplifications.

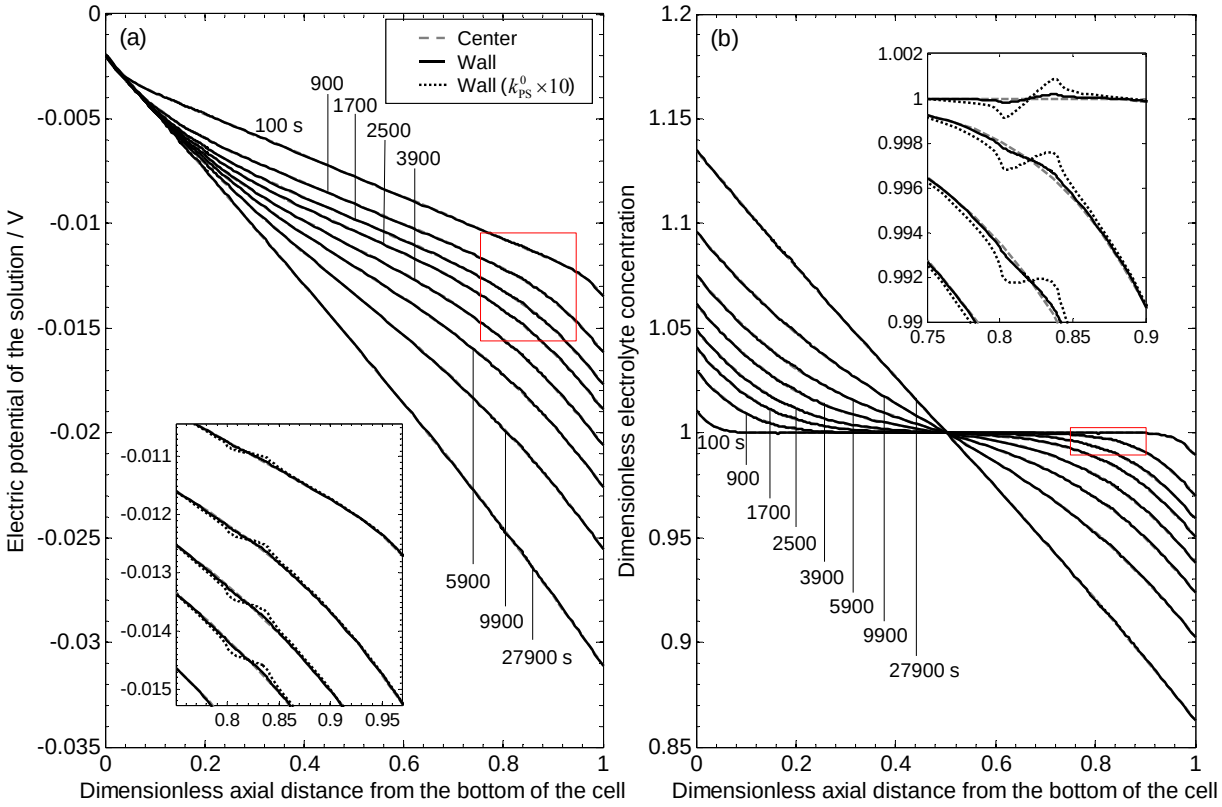

Figure 6-9. (a) Electric potential profile along the centerline (dashed lines) and at the wall (solid lines) of the cell as a function of dimensionless axial distance z/L from the WE and (b) dimensionless concentration c/c_{ini} profile at the center (dashed lines) and at the wall of the cell at $I_{\mathrm{app}} = 0.2$ mA for the $LiPF_6$/EC/DEC system. Insets: enlarged views of the regions of the curves within the red boxes; dotted lines are simulation results when $k^0_{\mathrm{PS}} = 7 \times 10^{-5}$ mol$^{0.5}$ m$^{-0.5}$ s^{-1}, i.e., ten times larger than its value used for the other two sets of simulations.

Figure 6-9 shows the simulated potential and Li concentration profiles in the axial direction along the centerline (dashed lines) and at the cell wall (solid lines) at different times. During the early stages of galvanostatic polarization ($t = 100$ s), semi-infinite diffusion conditions prevail and the Li concentration is uniform along the length of the cell except for the edges adjacent to the WE and CE. At the other end of the process, near-linear concentration potential profiles are attained as the system reaches steady-state (i.e., at $t = 27900$ s). The profiles along the cell wall perfectly match those at the centerline except for two narrow regions coinciding with the potential sensors. It can be seen in

the insets that the concentration and potential profiles adjacent to the sensors deviate from those at the center of the cell (i.e., away from electrodes) negatively on the left side (cathodic pole) and positively on the right side (anodic pole) of the electrode. The bipolar effect reduces the gradient of the solution electric potential across the electrode, i.e., smaller local field amplitude, and hence is self-damping. The potential measured by the sensor l and the equilibrium locus $z_{\mathrm{eq},l}$ coincides with the inflection point of the concentration and potential profiles (i.e., $\partial^2 c/\partial z^2 = 0$ and $\partial^2 \Phi/\partial z^2 = 0$, respectively) alongside the sensor where local reaction rate is zero, i.e., $\mathbf{i} \cdot \hat{\mathbf{r}} = 0$ at $r = R_{\mathrm{cell}}$ and $z = z_{\mathrm{eq},l}$.

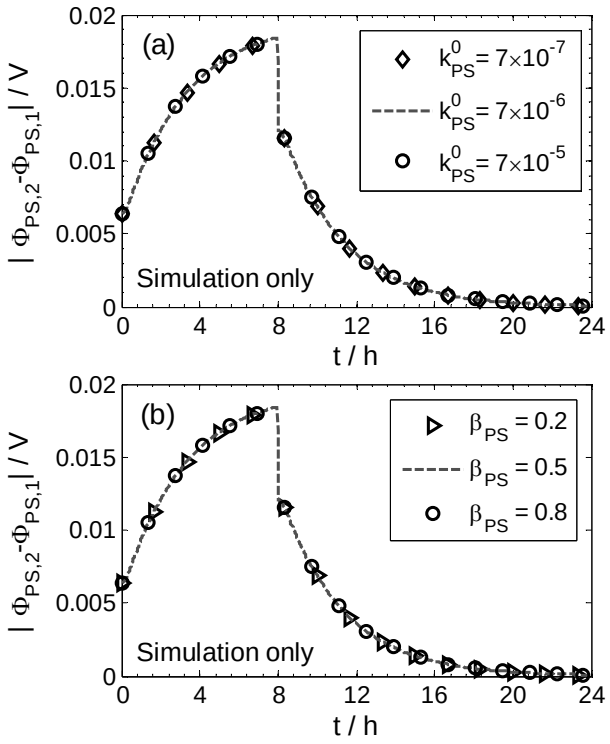

Figure 6-10. Model sensitivity to (a) reaction rate constant and (b) charge-transfer coefficient for $I_{\mathrm{app}} = 0.2$ mA applied to the $LiPF_6$/EC/DEC system. Model parameters are given in Table 6-1 and Table 6-2 except for those varied (see legends).

It is shown in Figure 6-9 that the bipolar electrochemical reactions at the potential sensors have negligible impact on the concentration and potential profiles for the two systems examined in this chapter. However, depending on the kinetic parameters (i.e., k^0_{PS} and β_{PS}) of the potential sensors and geometric design of the cell (i.e., sensor width δ and cell radius R_{cell}) the bipolar effect may influence the potential difference between the two PS. Sensitivity of the model to these parameters is

investigated by varying one parameter at a time while keeping the other parameters constant, as shown in Figure 6-10 and Figure 6-11.

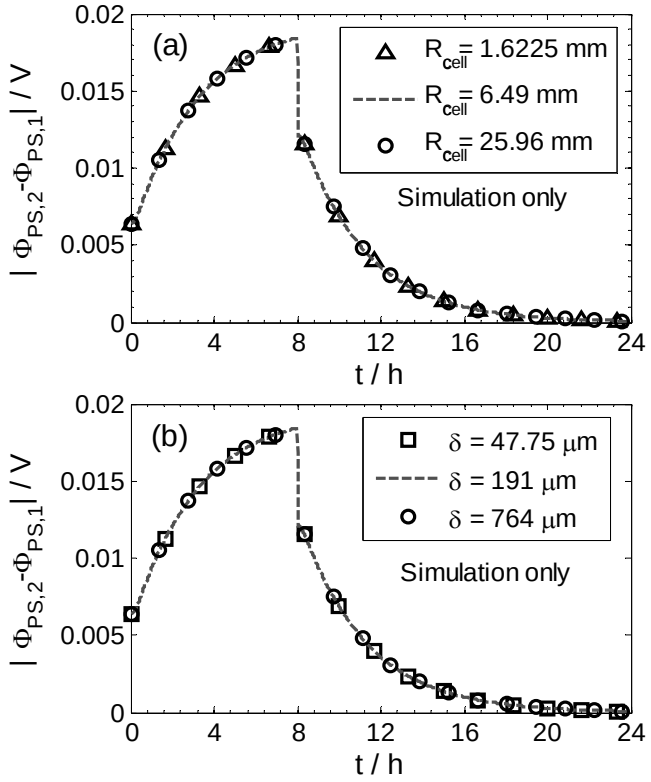

Figure 6-11. Effects of (a) cell radius and (b) potential sensor width on the potential difference between the two sensors for $I_{\mathrm{app}} = 0.2$ mA applied to the $LiPF_6$/EC/DEC system. Model parameters are given in Table 6-1 and Table 6-2 except for those varied (see legends).

As shown in Figure 6-10a, although the rate constant is varied by an order of magnitude, no visible change is seen in the simulated potential difference between the potential sensors. Although the bipolar effect is more pronounced for an electrode with a faster kinetics (dotted lines in Figure 6-9), it is insufficient to alter the measured voltage. Moreover, the equilibrium locus $z_{\mathrm{eq},l}$ is independent of the reaction rate constant according to Eq. (A-4) if local perturbations are ignored. Simulations also remained unchanged when the charge-transfer coefficient is varied. It is shown in Appendix A that the variation of β_{PS} does not lead to a significant displacement of the equilibrium locus even under a constant electric field four times as large as that at the centerline of the cell at $t = 8$ h. It implies that no alteration of the simulated voltages occurs upon changing the charge-

transfer coefficient. The same argument is valid if local perturbations of the electrolyte concentration profile are taken into account as they reduce the electric field locally. Further discussion on the effect of the charge-transfer coefficient is presented in Appendix A. In brief, the four-electrode measurements of the two electrolyte systems studied are insensitive to charge-transfer kinetics at the sensors.

The design parameters R_{cell} and δ are examined by increasing or reducing them by a factor of 4 relative to their values in the actual experimental setup. The results shown in Figure 6-11a and b again indicate that these changes have no significant effect on the voltage response. Altogether, under the operating condition of interest to electrolyte characterization studies (i.e., small applied current), local perturbations are not strong enough to cause the reaction kinetics to affect the measurements in a four-electrode cell with the design parameter values examined here.

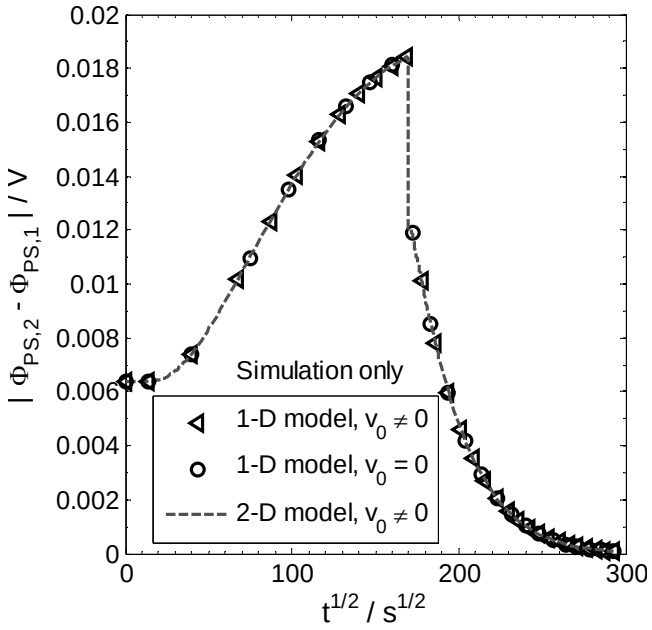

Figure 6-12. Comparison between the potential differences between the PS obtained using the 2-D (dashed line) and the 1-D models accounting for (triangles) and ignoring (circles) convective transport in the 1-D model ($I_{\text{app}} = 0.2$ mA applied to the $LiPF_6$/EC/DEC system).

Figure 6-12 shows a comparison between the simulations of the 2-D model and a 1-D version of the same model (i.e., bipolar effect is not accounted for) with convection included (triangles) and excluded but compensated for by using the corresponding values of $\mathcal{D}$ and t_+^0 in Table 6-2 (circles). It turns out that the results of the two models overlap almost perfectly under the operating conditions

and for the cell design of this study. Therefore, we conclude that the 2-D model presented here can be reduced to a 1-D model without an important loss of accuracy. A 1-D model is computationally less expensive and easier to implement than the 2-D model and can be more easily coupled with an appropriate optimization routine as a numerical fitting tool if a comprehensive analysis is to be performed at different concentrations and temperatures where manual fitting becomes cumbersome.

The positions of the PS determine the magnitude of the potential difference between them and the time when the effect of the concentration gradient begins to appear at the onset of the closed-circuit (Figure 6-13a) and when the open-circuit potential decay becomes a straight line on a semi-logarithmic plot (Figure 6-13b); the farther the PS are from each other (assuming constant spacing between the WE and CE), the larger the potential difference and so the more sensitive to the transport properties with the same cell length and under the same operating conditions.

A cell with a larger spacing between the PS provides as much useful data at a given applied current as one with a smaller spacing but operating at a larger current. However, the applied current is subject to more stringent constraints in this analysis in order to maintain the underlying assumptions including negligible heat of reaction at the electrodes and heat of mixing in the bulk (especially important at low-temperature measurements), negligible free convection due to temperature non-uniformity and negligible displacement of the WE/solution and CE/solution interface due to electro-plating/stripping. Moreover, a larger applied current during the closed-circuit portion of the pulse leads to a longer relaxation time when the current is switched off, making the system more susceptible to external vibrations. On the other hand, if the sensors are moved too close to the CE and WE, the constant voltage region at the onset of the closed-circuit phase shrinks and makes deciphering of ionic migration slightly more difficult although not impossible. The ionic conductivity could be sought by analyzing its contribution over the entire the CCV data. Nonetheless, the non-zero electrode width and technical barriers in the cell assembly itself limit the minimum spacing between the WE/CE surface and the potential measurement spot in the PS, i.e., $z_{\mathrm{eq},l}$. It should be noted that no theoretical constraint on the location of the PS exists since the model is solved numerically [112]. Altogether, the cell arrangement used in this research (i.e., cell length, sensor spacing and sensor width) and the operating condition (i.e., the applied current waveform) proved to be a reasonable trade-off between the quality of data and practical considerations of the method.

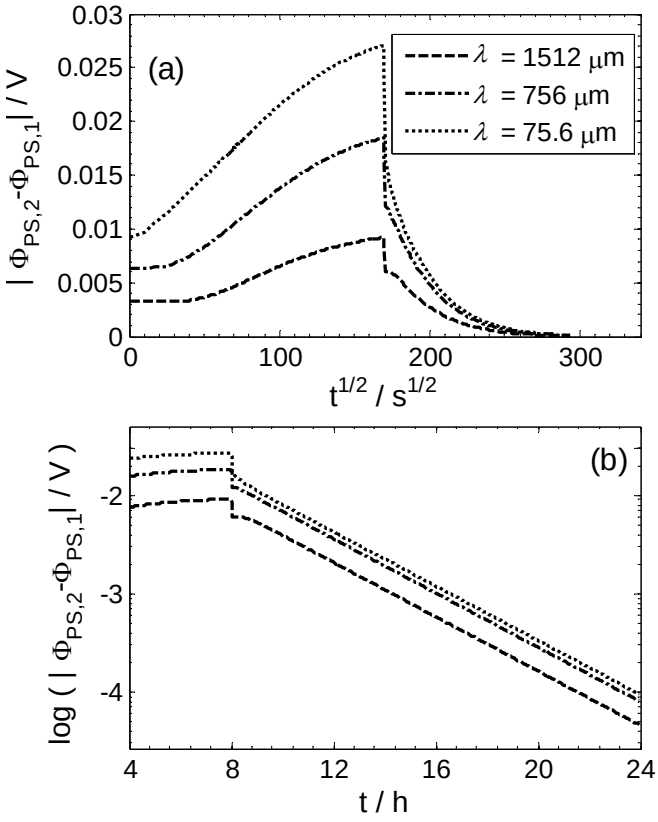

Figure 6-13. Simulated potential difference between the two PS in a cell with different spacing between WE/CE and the PS (I_{app} = 0.2 mA applied to the $LiPF_6$/EC/DEC system). Model parameters are given in Table 6-1 and Table 6-2 except for those varied (see legend).

6.7 Conclusion

In this chapter, the four-electrode-cell method for the characterization of concentrated binary electrolytes has been demonstrated and compared with the conventional electrochemical methods. The cornerstone principle of the method is the use of two reference electrodes (i.e., potential sensors) in an electrochemical cell in addition to the working and counter electrodes. Variations in the electric potential of the electrolyte are recorded across the two sensors while a rectangular current pulse is applied to the working and counter electrodes. As such, the four-electrode cell provides direct access to the closed-circuit as well as open-circuit voltage in a manner not distorted by the main and side reactions or double-layer effects at the working and counter electrodes. The recorded data exhibit unique features each of which can be unambiguously attributed to one of the three independent transport properties: i) constant voltage at the onset is contributed solely by ionic migration (i.e., ionic

conductivity of the electrolyte), ii) exponential decay of open-circuit data with time is controlled by diffusion (i.e., chemical diffusion coefficient) and iii) transient portion of closed-circuit data is attributed to both migration and diffusion (i.e., transference number).

A general 2-D axi-symmetric model based on concentrated-solution theory that takes into account the bipolar effect at the sensors located at the cell wall was developed. A single galvanostatic polarization pulse in combination with concentration-cell experiments was shown to be sufficient to uniquely estimate the transport properties and thermodynamic factor. The model was compared with experimental data via a manual parameter search routine in accordance with the orthogonal features of the data.

To investigate the effect of faradaic convection, the model was used to estimate transport properties with and without the convective term included in the flux expressions. The thermodynamic diffusion coefficient $\mathcal{D}$ and the transference number t_+^0 were estimated to markedly differ (i.e., by 11.2% and 19.7%, respectively) depending on whether or not the convection is included. Therefore, the inclusion of this effect is warranted when using these parameter estimates in an end-use electrochemical model to ensure that its assumptions are compatible with those of the parameter estimation method. Although neglected in the mass transport model, the pressure drop along the cell length was calculated according to the Darcy's law to be of the order of 10^{-3} Pa, which is small enough for the isobaric assumption to hold.

Sensitivity analysis of the reaction kinetics at the sensing electrodes and the geometric parameters of the cell suggest that the bipolar effect is not strong enough to interfere with the potential measurements under the operating conditions relevant to the electrolyte characterization experiments. It is further confirmed by comparing simulation results from a 1-D model with those obtained from the original 2-D model. The 1-D model is computationally inexpensive and can be coupled with an optimization routine to estimate concentration-dependent transport properties if experimental data at different concentrations are available.

The proposed technique benefits considerably from the ready measurement of closed-circuit data for estimation of the transference number. The abundance and direct acquisition of data points as compared with the conventional semi-infinite method promises a high level of accuracy and reliability of the estimated transference number.

The measurement of diffusion coefficient closely follows the restricted diffusion experiment. Nonetheless, the three transport properties are obtained simultaneously for the same sample and in the same electrochemical cell under less strict operating conditions. These factors eliminate uncertainties associated with combining data obtained from separate experiments, as done in the conventional methods.

The method was demonstrated by applying it to two Li-based liquid binary electrolytes but it is equally applicable to any other binary electrolytes dissolved in aqueous, non-aqueous or polymeric solvents.

Chapter 7
Conclusions and Recommendations

7.1 Conclusions and Contributions

In this thesis mathematical models are used as cheap and simple tools to investigate the electrochemical performance of LFP electrodes. The mesoscopic model developed in this work appears to overcome the shortcomings of conventional solid-solution-type or core-shell models and represents a major step towards a simple yet accurate mathematical description of phase-change electrodes. Analysis of electrode dynamics under various operating conditions provides new insights into complexities associated with the unit-to-unit interactions in a many-unit electrode ensemble and provides quantitative explanation for the peculiar behavior of the electrode.

In Chapter 3, Two distinct models, the variable solid-state diffusivity model and the resistive-reactant model, are used to study solid-state Li transport (bulk limitations) and electronic conductivity (surface limitations), respectively. The models are separately applied to fit the experimental galvanostatic discharge data obtained from a commercial LFP electrode. The particle-size distribution in the VSSD model and contact-resistance distribution in the RR model are obtained by fitting to a wide range of currents.

Full-range simulations confirm the effectiveness of the VSSD model as it accurately predicts the electrode potential loss over the entire SOC range. The concentration-dependent diffusion coefficient can be regarded as a lumped parameter that accounts for various phenomena including phase transformation in a real LFP electrode. However, a very small solid-state diffusion coefficient ($\sim 10^{-19}\ \mathrm{m^2\ s^{-1}}$) is required to fit the model to the experimental discharge data, which is contradictory to first principles calculations and recent experimental observations of fast lithiation/delithiation of this material. The particle-size distribution, on the other hand, turns out to play a pivotal role in the VSSD model; however, it appears to be rate-dependent, that is, the fitted PSD is shifted towards smaller particles in order to accurately predict the electrode performance during galvanostatic discharge at higher applied currents. In the resistive-reactant model, a set of contact resistances is responsible simultaneously for capturing both the slanted behavior of the potential-capacity curves (i.e., additional to porous-electrode effects) and the end-of-discharge capacities at different C-rates (i.e., in addition to diffusion limitations in the d_{50} particle). The model can explain the SOC-dependent part of the electrode potential loss attributed to bulk limitations in the

VSSD model. The best fitted CRD, despite being extremely broad (~ 1 to $\sim 10^2\ \Omega\ \mathrm{m}^2$), over-predicts the capacities at very low C-rates.

From a comparison of the RR and VSSD models, it appears that VSSD is a simpler model for use as a reliable semi-empirical platform for practical situations including performance analysis, thermal studies, and lifetime prediction of LFP-based commercial batteries.

In Chapter 4, a simple mathematical model for the dynamics of phase-transforming porous electrodes is presented and applied to $LiFePO_4$. In contrast to the first part of this research, the new model completely disregards solid-state diffusion limitations but, instead, features a non-equilibrium solid-solution pathway (i.e., non-monotonic equilibrium potential predicted by the regular solution model) for Li insertion/de-insertion into and a Gaussian distribution of resistances among many electronically and ionically wired meso-scale insertion domains constituting the porous electrode. The entire active material domain is discretized into elementary units representing these meso-scale domains with no consideration of any geometric detail. With only these two factors involved, the model can simultaneously explain a number of unusual qualities associated with lithium iron phosphate electrochemical performance including the quasi-static potential hysteresis, high rate capability, cycle-path dependence, mismatch of electrode polarization during GITT and during a continuous cycling at the same current, bell-shaped current response in PITT and the most recently observed memory effect.

Detailed analysis of the electrode dynamics suggests that a necessary condition for the memory effect to appear in an LFP electrode is the existence of a non-zero residual capacity at the onset of memory-release step which may originate either from a non-zero initial SOC or from an imbalanced writing cycle. A memory effect should not, therefore, be observed in an electrode that has been preconditioned at extremely low currents (i.e., zero initial SOC) and has undergone an extremely slow memory-writing cycle (i.e., approaching a balanced cycle).

In Chapter 5, the mesoscopic model developed before is incorporated into porous-electrode theory and validated by comparing the simulation results with experimental data obtained during continuous and intermittent galvanostatic discharge of a commercial $LiFePO_4$ electrode at various operating conditions. An asymmetric solid-solution model describes the thermodynamic state of individual elementary units as a non-monotonic equilibrium potential function of composition. A bimodal lognormal resistance distribution is assumed to account for disparity of insertion dynamics among elementary units.

Simulation results compare well with experimental data obtained from continuous (i.e., both low and high applied currents) and intermittent discharge experiments. According to the model, the many-unit effects appear at relatively large time scales depending on the depth of discharge and should not be confused with solid-state diffusion process. It is suggested that, proper GITT experiments may be used to estimate the non-equilibrium thermodynamic properties (i.e., single-unit equilibrium potential) of phase-change active materials of which no actual measurement has been reported to date.

Further analysis of the GITT experiments suggest that, depending on the overall depth-of-discharge of the electrode and the incremental depth-of-discharge (charge) of each GITT pulse, the solid-solution capacity available in the Li-rich (Li-poor) end-member may be able to accommodate entering (leaving) Li species entirely without the need for active (closed-circuit) phase transformation. Instead, redistribution of Li among units during relaxation equilibrates the solid-solution composition by transforming a few Li-poor (Li-rich) units to Li-rich (Li-poor) ones.

A realistic account of porous-electrode effects in the experimental validation of the mesoscopic LFP model requires accurate estimation of the transport properties of the electrolyte. In the last chapter, the development and evaluation of a novel four-electrode-cell method to determine the transport properties of concentrated binary electrolytes is presented and compared in detail with conventional semi-infinite and restricted diffusion methods. The cell consists of two reference electrodes in addition to the working and counter electrodes. The sensors measure the closed-circuit as well as open-circuit potential in response to an input current across the working and counter electrodes. An important advantage of this new method is that it requires only the application of a single galvanostatic polarization pulse and appropriate concentration-cell experiments. By fitting a suitable model to the data obtained from these experiments, the three independent transport properties of a concentrated binary electrolyte, namely, ionic conductivity κ, thermodynamic diffusion coefficient $\mathcal{D}$ and transference number t_+^0 can be determined. In particular, the measurement of the closed-circuit potential using this cell provides a simpler and essentially more accurate means to estimate the transference number than the conventional semi-infinite diffusion method.

A comprehensive 2-D axi-symmetric model based on concentrated-solution theory is developed to account for faradaic convection as well as the bipolar effect at the surface of the potential sensors. Sensitivity analysis of the kinetic properties of the potential sensors and the geometric parameters of the cell suggests that the bipolar effect has negligible impact on the potential

measurements under operating conditions relevant to these experiments. Consequently, a simpler 1-D model can be used in place of the 2-D model to estimate the transport properties without any loss in accuracy.

7.2 Recommendations

This thesis provides new insight into the modeling of phase-change active materials which are of special interest for use in high power Li-ion batteries. There are a number of recommendations that could be considered for future research.

7.2.1 Mesoscopic Modeling of $LiFePO_4$

The simplicity of the mesoscopic model developed in the research work does not rule out known complications at the unit and electrode levels which can significantly influence the unit-to-unit interactions.

Electrode level – At the electrode level, porous-electrode theory is used in this thesis to take into account the variation of ionic and electronic environment of insertion units across the electrode from separator to current collector. It is based on superposition of the two solid and liquid phases and volume-averaging of the model quantities (i.e., physical properties and field variables). As a result, the theory is not able to resolve microstructural non-uniformities (e.g., variation of active material loading, dispersion of conductive fillers and electrolyte-filled pores) whereas the inter-unit transport strongly depends on these inhomogeneities. An alternative approach would be to solve the charge and mass transport equations across reconstructed 3-D electrode microstructure (e.g., using X-ray computed tomography) in place of porous-electrode theory. Such a practice would also examine the validity of porous-electrode theory for phase-change electrodes where the effect of very large local reaction rates at the surface of active units may cause electrolyte depletion/accumulation and break down the averaging assumptions.

Unit level – A computed tomography of an LFP electrode could also be used to resolve the microstructure at the unit level i.e., where the auxiliary conducting phases connect units together, if the imaging resolution approaches to a few nanometers. However such high resolution imaging would be sophisticated and too costly for regular use. Instead, one could resort to finding a distribution that can faithfully represent the lumped resistances and fit the experimental data.

Experimental measurements – Experimental data used in this research were obtained using a two-electrode electrochemical setup. Use of a three-electrode configuration will help remove artifacts associated with the charge-transfer reactions at the metallic Li counter electrode which are not symmetric in nature during electrode charging (i.e., electro-plating) and discharging (i.e., electro-stripping).

The above improvements may also help explain the asymmetry in the electrode performance between charging and discharging both at low and high rates which is not explained in this thesis.

Parameter search – In this thesis work, the model is fitted to experimental data by manually adjusting parameters of the proposed resistance distribution and single-unit solid-solution model. As such, parameter search is limited to the cases where simple thermodynamic models and resistance distributions are assumed. The former yields the single-unit equilibrium potential, a critical property of phase-change insertion materials for which no estimation method has been suggested to date. More sophisticated thermodynamic models may be characterized by means of a numerical optimization procedure that fits the dynamic mesoscopic model to a large set of experimental data.

7.2.2 Four-Electrode-Cell Electrolyte Characterization

Cell design – In this research a cylindrical geometry is used to set up the four-electrode cell with annular potential sensors which simplify the computation domain by means of axial symmetry. However, it has been shown that potential sensors do not significantly influence the estimated transport and thermodynamic properties and a 1-D mathematical model can be used to back out these properties regardless of cell geometry (e.g., cylindrical or rectangular). A second prototype could, thus, be designed without regard to this dimensionality constraint while minimizing other sources of errors including the accurate length measurement or elimination of the porous separator.

Characterization – In this thesis the performance of the four-electrode-cell method is assessed by characterizing two different commercially available electrolytes at a given concentration. As a future work, concentration- and temperature-dependent transport properties could be estimated if electrolyte samples at different concentrations are prepared and separately examined in the four-electrode cell at different temperature.

REFERENCES

[1] Transport, Energy and CO_2. Technical report, International Energy Agency, 2010.

[2] World energy outlook 2015, executive summary. Technical report, International Energy Agency, 2015.

[3] J.-M. Tarascon and M. Armand. *Nature Mater.*, 414:19–30, 2001.

[4] Technology Roadmap, electric and plug-in hybrid electric vehicles. Technical report, International Energy Agency, 2011.

[5] M. S. Whittingham. *Chem. Rev.*, 104:4271–4301, 2004.

[6] A. K. Padhi, K. S. Nanjundaswamy, and J. B. Goodenough. *J. Electrochem. Soc.*, 144:1188–1194, 1997.

[7] K. Xu. *Encyclopedia of Electrochemical Power Sources*. Elsevier B.V., 2009.

[8] J. B. Goodenough, A. K. Padhi, K. S. Nanjundaswamy, and C. Masquelier. U.S. Pat. 5,910,382, 1999.

[9] A. Yamada, H. Koizumi, S-I. Nishimura, N. Sonoyama, R. Kanno, M. Yonemura, T. Nakamura, and Y. Kobayashi. *Nature Mater.*, 5:357–360, 2006.

[10] B. Kang and G. Ceder. *Nature*, 458:190–193, 2009.

[11] X. Zhang, M. van Hulzen, D. P. Singh, A. Brownrigg, J. P. Wright, N. H. van Dijk, and M. Wagemaker. *Nano Lett.*, 14:2279–2285, 2014.

[12] H. Liu, F. C. Strobridge, O. J. Borkiewicz, K. M. Wiaderek, K. W. Chapman, P. J. Chupas, and C. P. Grey. *Science*, 344:1252817, 2014.

[13] V. Srinivasan and J. Newman. *Electrochem. Solid State Lett.*, 9(3):A110–A114, 2006.

[14] W. Dreyer, J. Jamnik, C. Guhlke, R. Huth, J. Moskon, and M. Gaberscek. *Nature Mater.*, 9:448–453, 2010.

[15] G. Oyama, Y. Yamada, R. Natsui, S. Nishimura, and A. Yamada. *J. Phys. Chem. C*, 116:7306–7311, 2012.

[16] M. Farkhondeh and C. Delacourt. *J. Electrochem. Soc.*, 159(2):A177–A192, 2012.

[17] T. Sasaki, Y. Ukyo, and P. Novak. *Nature Mater.*, 12:569–575, 2013.

[18] K. Xu. *Chem. Rev.*, 104:4303–4418, 2004.

[19] M. Xu, D. G. Ivey, Z. Xie, and W. Qu. *J. Power Sources*, 283:358–371, 2015.

[20] D. Aurbach, Y. Talyosef, B. Markovsky, E. Markevich, E. Zinigrad, L. Asraf, J. S. Gnanaraj, and H-J Kim. *Electrochim. Acta*, 50:247–254, 2004.

[21] K. Xu. *Chem. Rev.*, 114:11503–11618, 2014.

[22] Y. Yamada and A. Yamada. *J. Electrochem. Soc.*, 162:A2406–A2423, 2015.

[23] A. C. Luntz and B. D. McCloskey. *J. Electrochem. Soc.*, 162:A2406–A2423, 2015.

[24] K. M. Abraham. *J. Electrochem. Soc.*, 162:A3021–A3031, 2015.

[25] M. Balaish, A. Kraytsberg, and Y. Ein-Eli. *Phys. Chem. Chem. Phys.*, 16:2801–2822, 2014.

[26] M. Barghamadi, A. S. Best, A. I. Bhatt, A. F. Hollenkamp, M. Musameh, R. J. Rees, and T. Ruther. *Energy Environ. Sci.*, 7:3902–3920, 2014.

[27] S. Zhang, K. Ueno, K. Dokko, and M. Watanabe. *Adv. Energy Mater.*, 5:1500117, 2015.

[28] E. M. Erikson, E. Markevich, G. Salitra, D. Sharon, D. Hirshberg, E. de la Llave, I. Shterenberg, A. Rozenman, and A. Frimer. *J. Electrochem. Soc.*, 162:A2424–A2438, 2015.

[29] A. Ponrouch, D. Monti, A. Boschin, B. Steen, P. Johansson, and M. R. Palacin. *J. Phys. Chem. A*, 3:22–42, 2015.

[30] R. Mohtadi and F. Mizuno. *Beilstein J. Nanotechnol.*, 5:1291–1311, 2014.

[31] Y. Ma, M. Doyle, T. F. Fuller, M. M. Doeff, L. C. De Jonghe, and J. Newman. *J. Electrochem. Soc.*, 142:1859–1868, 1995.

[32] M. M. Doeff, P. Georen, J. Qiao, J. Kerr, and L. C. De Jonghe. *J. Electrochem. Soc.*, 146:2024–2028, 1999.

[33] C. Capiglia, Y. Saito, H. Kageyama, P. Mustarelli, T. Iwamoto, T. Tabuchi, and H. Tukamoto. *J. Power Sources*, 81-82:859–862, 1999.

[34] C. Capiglia, Y. Saito, H. Yamamoto, H. Kageyama, and P. Mustarelli. *Electrochim. Acta*, 45:1341–1345, 2000.

[35] P. Georen and G. Lindberg. *Electrochim. Acta*, 47:577–587, 2001.

[36] P. Georen and G. Lindbergh. *Electrochim. Acta*, 49:3497–3505, 2004.

[37] L. O. Valoen and J. N. Reimers. *J. Electrochem. Soc.*, 152:A882–A891, 2005.

[38] S. Stewart and J. Newman. *J. Electrochem. Soc.*, 155:F13–F16, 2008.

[39] A. Nyman, M. Behm, and G. Lindbergh. *Electrochim. Acta*, 53:6356–6365, 2008.

[40] A. Nyman, M. Behm, and G. Lindbergh. *J. Electrochem. Soc.*, 158:A636–A643, 2011.

[41] M. Klett, M. Giesecke, A. Nyman, F. Hallberg, R. W. Lindstrom, G. Lindberg, and I. Furo. *J. Am. Chem. Soc.*, 134:14654–14657, 2012.

[42] A. K. Sethurajan, S. A. Krachkovskiy, I. C. Halaly, G. R. Goward, and B. Protas. *J. Phys. Chem. B*, 119:12238–12248, 2015.

[43] H. Lundgren, M. Behm, and G. Lindberg. *J. Electrochem. Soc.*, 162:A413–A420, 2015.

[44] H. Lundgren, J. Scheers, M. Behm, and G. Lindberg. *J. Electrochem. Soc.*, 162:A1334–A1340, 2015.

[45] A. S. Andersson, J. O. Thomas, B. Kalska, and L. Haggstrom. *Electrochem. Solid State Lett.*, 3:66–68, 2000.

[46] W. Porcher, P. Moreau, B. Lestriez, S. Jouanneau, and D. Guyomard. *J. Electrochem. Soc.*, 11:A4–A8, 2008.

[47] P. G. Bruce, B. Scrosati, and J.-M. Tarascon. *Angew. Chem. Int. Ed.*, 47:2930–2946, 2008.

[48] C. Delacourt, C. Wurm, L. Laffont, J.-B. Leriche, and C. Masquelier. *Solid State Ionics*, 177:333–341, 2006.

[49] N. Ravet, J. B. Goodenough, S. Besner, M. Simoneau, P. Hovington, and M. Armand. *196th Meeting of the Electrochemical Society*, Abstract # 127 Hawai, 1999.

[50] N. Ravet, Y. Chouinard, J. F. Magnan, S. Besner, M. Gauthier, and M. Armand. *J. Power Sources*, 97-98:503–507, 2001.

[51] P. Subramanya Herle, B. Ellis, N. Coombs, and L. F. Nazar. *Nature Mater.*, 3:147–152, 2004.

[52] S. Y. Chung, J. T. Bloking, and Y. M. Chiang. *Nature Mater.*, 1:123 –128, 2002.

[53] N. Ravet, A. Abouimrane, and M. Armand. *Nature Mater.*, 2:702, 2003.

[54] A. Yamada, S. C. Chung, and K. Hinokuma. *J. Electrochem. Soc.*, 148:A224–A229, 2001.

[55] C. Delacourt, P. Poizot, S. Levasseur, and C. Masquelier. *Electrochem. Solid State Lett.*, 9(7):A352–A355, 2006.

[56] A. Yamada, H. Koizumi, N. Sonoyama, and R. Kanno. *Electrochem. Solid State Lett.*, 8(8):A409–A413, 2005.

[57] V. Srinivasan and J. Newman. *J. Electrochem. Soc.*, 151(10):A1517–A1529, 2004.

[58] J. Dodd, R. Yazami, and B. Fultz. *Electrochem. Solid State Lett.*, 9:A151–A155, 2006.

[59] M. Safari and C. Delacourt. *J. Electrochem. Soc.*, 158(2):A63–A73, 2011.

[60] C. Delacourt, J. Rodríguez-Carvajal, B. Schmitt, J.-M. Tarascon, and C. Masquelier. *Solid State Science*, 7(12):1506–1516, 2005.

[61] C. Delacourt, P. Poizot, J.-M. Tarascon, and C. Masquelier. *Nature Mater.*, 4:254–260, 2005.

[62] R. Stevens, J. .R Dodd, M. G. Kresch, R. Yazami, B. Fultz, B. Ellis, and L. F. Nazar. *J. Phys. Chem. B*, 110:22732, 2006.

[63] F. Zhou, T. Maxisch, and G. Ceder. *Phys. Rev. Lett.*, 97:155704, 2006.

[64] M. Tang, W. C. Carter, and Y.-M. Chiang. *Annu. Rev. Mater. Res.*, 40:501–529, 2010.

[65] P. Gibot, M. Casas-Cabanas, L. Laffont, S. Levasseur, P. Carlach, S. Hamelet, J.-M. Tarascon, and C. Masquelier. *Nature Mater.*, 7:741–747, 2008.

[66] N. Meethong, H-Y. Shadow Huang, S. A. Speakman, W. Craig Carter, and Y-M. Chiang. *Electrochem. Solid State Lett.*, 10(5):A134–A138, 2007.

[67] G. Chen, X. Song, and T. J. Richardson. *Electrochem. Solid State Lett.*, 9(6):A295–A298, 2006.

[68] L. Laffont, C. Delacourt, P. Gibot, M. Yue Wu, P. Kooyman, C. Masquelier, and J.-M. Tarascon. *Chem. Mater.*, 18:5520–5529, 2006.

[69] D. Morgan, A. Van der Ven, and G. Ceder. *Electrochem. Solid State Lett.*, 7(2):A30–A32, 2004.

[70] C. Ouyang, S. Shi, Z. Wang, X. Huang, and L. Chen. *Phys. Rev. B*, 69:104303, 2004.

[71] G. Chen, X. Song, and T. J. Richardson. *J. Electrochem. Soc.*, 154:A627–A632, 2007.

[72] Y. Zhu, J. W. Wang, Y. Liu, X. Liu, A. Kushima, Y. Liu, Y. Xu, S. X. Mao, J. Li, C. Wang, and J. Y. Huang. *Adv. Mater.*, 25:5461–5466, 2013.

[73] C. Delmas, M. Maccario, L. Croguennec, F. Le Cras, and F. Weill. *Nature Mater.*, 7:665–671, 2008.

[74] G. Brunetti, D. Robert, P. Bayle-Guillemaud, J. L. Rouviere, E. F. Rauch, J. F. Martin, J. F. Colin, F. Bertin, and C. Cayron. *Chem. Mater.*, 23:4515–4524, 2011.

[75] W. C. Chueh, F. El Gabaly, J. D. Sugar, N. C. Bartelt, A. H. McDaniel, K. R. Fenton, K. R. Zavadil, T. Tyliszczak, W. Lai, and K. F. McCarty. *Nano Lett.*, 13:866–872, 2013.

[76] D. Robert, T. Douillard, A. Boulineau, G. Brunetti, P. Nowakowski, D. Venet, P. Bayle-Guillemaud, and C. Cayron. *ACS Nano*, 7:10887–10894, 2013.

[77] K. Weichert, W. Sigle, P A. van Aken, J. Jamnik, C. Zhu, R. Amin, T. Acarturk, U. Starke, and J. Maier. *J. Am. Chem. Soc.*, 134:2988–2992, 2012.

[78] Y. S. Yu, C. Kim, D. A. Shapiro, M. Farmand, D. Qian, T. Tyliszczak, A. L. D. Kilcoyne, R. Celestre, S. Marchesini, J. Joseph, P. Denes, T. Warwick, F. C. Strobridge, C. P. Grey, H. Padmore, Y. S. Meng, R. Kostecki, and J. Cabana. *Nano Lett.*, 134:4282–4288, 2015.

[79] D. A. Shapiro, Y. S. Yu, T. Tyliszczak, J. Cabana, R. Celestre, W. Chao, K. Kaznatcheev, A. L. D. Kilcoyne, F. Maia, S. Marchesini, Y. S. Meng, T. Warwick, L. L. Yang, and H. Padmore. *Nature Photon.*, 8:765–769, 2014.

[80] U. Boesenberg, F. Meirer, Y. Liu, A. K. Shukla, R. Dell'Anna, T. Tyliszczak, G. Chen, J. C. Andrews, T. J. Richardson, R. Kostecki, and J. Cabana. *Chem. Mater.*, 25:1664–1672, 2013.

[81] M. D. Levi, S. Sigalov, G. Salitra, P. Nayak, D. Aurbach, L. Daikhin, E. Perre, and V. Presser. *J. Phys. Chem. C*, 117:15505–15514, 2013.

[82] J. N. Weker, Y. Li, R. Shanmugam, W. Lai, and W. C. Chueh. *ChemElectroChem*, 2:1576–1581, 2015.

[83] W. Dreyer, C. Guhlke, and M. Herrmann. *Continuum Mech. Thermodyn.*, 23:211–231, 2011.

[84] Y. Li, J. N. Weker, W. E. Gent, D. N. Mueller, J. Lim, D. A. Cogswell, T. Tyliszczak, and W. C. Chueh. *Adv. Funct. Mater.*, 25:3677–3687, 2015.

[85] Y.-H. Kao, M. Tang, N. Meethong, J. Bai, W. C. Carter, and Y.-M. Chiang. *Chem. Mater.*, 22:5845–5855, 2010.

[86] D. Cogswell and M. Z. Bazant. *Nano Lett.*, 13:3036–3041, 2013.

[87] C. Wang, U. S. Kasavajjula, and P. E. Arce. *J. Phys. Chem. C*, 111:16656–16663, 2007.

[88] U. S. Kasavajjula, C. Wang, and P. E. Arce. *J. Electrochem. Soc.*, 155(11):A866–A874, 2008.

[89] S. Dargaville and T. W. Farrell. *J. Electrochem. Soc.*, 157(7):830–840, 2010.

[90] B. C. Han, A. Van der Ven, D. Morgan, and G. Ceder. *Electrochim. Acta*, 49:4691–4699, 2004.

[91] G. K. Singh, G. Ceder, and M. Z. Bazant. *Electrochim. Acta*, 53:7599–7613, 2008.

[92] K. E. Thomas-Alyea. *ECS Transactions*, 16(13):155–165, 2008.

[93] S. Dargaville and T. W. Farrell. *Electrochim. Acta*, 94:143–158, 2013.

[94] P. Bai, D. A. Cogswell, and M. Z. Bazant. *Nano Lett.*, 11:4890–4896, 2011.

[95] D. Cogswell and M. Z. Bazant. *ACS Nano*, 6:2215–2225, 2012.

[96] D. Burch and M. Z. Bazant. *Nano Letters*, 9(11):3795–3800, 2009.

[97] M. Tang, H.-Y. Huang, N. Meethong, Y.-H. Kao, W. C. Carter, and Y.-M. Chiang. *Chem. Mater.*, 21:1557–1571, 2009.

[98] J. L. Allen, T. R. Jow, and J. Wolfenstine. *J. Solid State Electrochem.*, 12:1031–1033, 2007.

[99] J. L. Allen, T. R. Jow, and J. Wolfenstine. *Chem. Mater.*, 19:2108–2111, 2008.

[100] M. Farkhondeh, M. Safari, M. Pritzker, M. Fowler, T. Han, J. Wang, and C. Delacourt. *J. Electrochem. Soc.*, 161:A201–A212, 2014.

[101] M. Safari, M. Farkhondeh, M. Pritzker, M. Fowler, T. Han, and S.-K. Chen. *Electrochim. Acta*, 115:352–357, 2014.

[102] I. V. Thorat, T. Joshi, K. Zaghib, J. N. Harb, and D. R. Wheeler. *J. Electrochem. Soc.*, 158:A1185–A1193, 2011.

[103] W. Dreyer, I. Muller, and P. Strehlow. *Q. J. Mech. Appl.*, 35:419, 1982.

[104] W. Kitsche, I. Muller, and P. Strehlow. *IMA*, 3:213, 1986.

[105] A. Z. Weber, M. M. Mench, J. P. Meyers, P. N. Ross, J. T. Gostick, and Q. Liu. *J. Appl. Electrochem.*, 41:1137–1164, 2011.

[106] L. Su, M. Ferrandon, J. Kowalski, and J. Vaughey. *J. Electrochem. Soc.*, 161:A1905–A1914, 2014.

[107] J. S. Newman and K. E. Thomas-Alyea. *Electrochemical Systems*. Wiley Interscience, 2004.

[108] M. Doyle, T. F. Fuller, and J. Newman. *J. Electrochem. Soc.*, 140(6):1526–1533, 1993.

[109] M. Farkhondeh, M. Pritzker, M. Fowler, M. Safari, and C. Delacourt. *Phys. Chem. Chem. Phys.*, 16:22555–22565, 2014.

[110] Z. Mao, M. Farkhondeh, M. Pritzker, M. Fowler, and Z. Chen. *J. Electrochem. Soc.*, 163:A458–A469, 2016.

[111] M. Mastali Majdabadi, S. Farhad, M. Farkhondeh, R. Fraser, and M. Fowler. *J. Power Sources*, 275:633–643, 2015.

[112] J. Newman and T. W. Chapman. *AIChE J.*, 19:343–348, 1973.

[113] S. D. Thompson and J. Newman. *J. Electrochem. Soc.*, 136:3362–3369, 2000.

[114] H. S. Harned and D. M. French. *Annals New York Acad. Sci.*, 46:267–285, 1945.

[115] J. O'M. Bockris and A. K. N. Reddy. *Modern Electrochemistry, Vol. 1: Ionics*. Springer US, 1998.

[116] D. A. MacInnes and L. G. Longsworth. *Chem. Rev.*, 11:171–230, 1932.

[117] C. M. Mason and E. F. Mellon. *J. Chem. Educ.*, 16:512–513, 1939.

[118] H. Hafezi and J. Newman. *J. Electrochem. Soc.*, 147:3036–3042, 2000.

[119] J. Liu and C. W. Monroe. *Electrochim. Acta*, 167:357–363, 2015.

[120] P. G. Bruce and C. A. Vincent. *J. Electroanal. Chem.*, 225:1–17, 1987.

[121] M. Doyle and J. Newman. *J. Electrochem. Soc.*, 142:3465–3468, 1995.

[122] N. Balsara and J. Newman. *J. Electrochem. Soc.*, 162:A2720–A2722, 1995.

[123] J. Newman and W. Tiedemann. *AIChE J.*, 21:25–41, 1975.

[124] S-I. Nishimura, G. Kobayashi, K. Ohoyama, R. Kanno, M. Yashima, and A. Yamada. *Nature Mater.*, 7:707–711, 2008.

[125] I. V. Thorat. Ph. D. Dissertation, Brigham Young University, 2009.

[126] B. Paxton and J. Newman. *J. Electrochem. Soc.*, 143:1287–1292, 1996.

[127] M. W. Verbrugge and B. J. Koch. *J. Electrochem. Soc.*, 143:600, 1996.

[128] Q. Zhang, Q. Z. Guo, and R. E. White. *J. Electrochem. Soc.*, 153:A301–A309, 2006.

[129] J. Christensen and J. Newman. *J. Solid State Electrochem.*, 10:293–319, 2006.

[130] C. Delacourt, M. Ati, and J.-M. Tarascon. *J. Electrochem. Soc.*, 158:A741, 2011.

[131] D. K. Karthikeyan, G. Sikha, and R. E. White. *J. Power Sources*, 185:1398–1407, 2008.

[132] C. M. Doyle. Ph. D. Dissertation, University of California Berkeley, 1995.

[133] R. Dominko, M. Gaberscek, J. Drofenik, M. Bele, S. Pejovnik, and J. Jamnik. *J. Power Sources*, 119-121:770 – 773, 2003.

[134] M. M. Doeff, Y. Hu, F. McLarnon, and R. Kostecki. *Electrochem. Solid State Lett.*, 6:A207–A209, 2003.

[135] Y. Zhu and C. Wang. *J. Power Sources*, 196:1442–1448, 2011.

[136] M. Doyle and Y. Fuentes. *J. Electrochem. Soc.*, 150:A706–A713, 2003.

[137] http://www.whatman.com/GlassMicrofiberBinderFree.aspx.

[138] M. Ender, A. Weber, and E. Ivers-Tiffee. *Electrochem. Comm.*, 34:130–133, 2013.

[139] S. Santhanagopalan, Q. Guo, P. Ramadass, and R. E. White. *J. Power Sources*, 156:620–628, 2006.

[140] J. Liu, M. Kunz, K. Chen, N. Tamura, and T. J. Richardson. *J. Phys. Chem. Lett.*, 1:2120–2123, 2010.

[141] C. Delacourt and M. Safari. *Electrochim. Acta*, 56:5222–5229, 2011.

[142] A. S. Andersson, B. Kalska, P. Eyob, D. Aernout, L. Haggstrom, and J. O. Thomas. *Solid State Ionics*, 140:63–70, 2001.

[143] J. Jamnik and J. Maier. *Phys. Chem. Chem. Phys.*, 5:5215–5220, 2003.

[144] M. Wagemaker, F. M. Mulder, and A. Van der Ven. *Adv. Mater.*, 21:2703–2709, 2009.

[145] M. Wagemaker, W. J. H. Borghols, and F. M. Mulder. *J. Am. Chem. Soc.*, 129:4323–4327, 2007.

[146] K. T. Lee, W. H. Kan, and L. F. Nazar. *J. Am. Chem. Soc.*, 131:6044–6045, 2009.

[147] A. Van der Ven and M. Wagemaker. *Electrochem. Comm.*, 11:881–884, 2009.

[148] R. Malik, A. Abdellahi, and G. Ceder. *J. Electrochem. Soc.*, 160:A3179–A3197, 2013.

[149] S. Dargaville and T. W. Farrell. *Electrochim. Acta*, 111:474–490, 2013.

[150] T. R. Ferguson and M. Z. Bazant. *J. Electrochem. Soc.*, 159:A1967–A1985, 2012.

[151] B. Orvananos, R. Malik, H. C. Yu, A. Abdellahi, C. P. Grey, G. Ceder, and K. Thornton. *Electrochim. Acta*, 137:245–257, 2014.

[152] R. C. smith. *Smart Material Systems: Model Development*. SIAM, Philadelphia, 2005.

[153] H. Munakata, B. Takemura, T. Saito, and K. Kanamura. *J. Power Sources*, 217:444–448, 2012.

[154] C. Kuss, D. Lepage, G. Liang, and S. B. Schougaard. *Chem. Sci.*, 4:4223–4227, 2013.

[155] M. Saiful Islam, D. J. Driscoll, C. A. J. Fisher, and P. R. Slater. *Chem. Mater.*, 17:5085–5092, 2005.

[156] W. Weppner and R. A. Huggins. *J. Electrochem. Soc.*, 124:1569–1578, 1977.

[157] A. H. Thompson. *J. Electrochem. Soc.*, 126:608–616, 1979.

[158] Y. Orikasa, T. Maeda, Y. Koyama, H. Murayama, K. Fukuda, H. Tanida, H. Arai, E. Matsubara, Y. Uchimoto, and Z. Ogumi. *J. Am. Chem. Soc.*, 135:5497–5500, 2013.

[159] L. Guo, Y. Zhang, J. Wang, L. Ma, S. Ma, Y. Zhang, E. Wang, Y. Bi, D. Wang, W. C. McKee, Y. Xu, J. Chen, Q. Zhang, C. Nan, L. Gu, P. G. Bruce, and Z. Peng. *Nat. Commun.*, 6:8898–8905, 2015.

[160] K. B. Gundrud, O. Nilsen, and H. Fjellvag. *J. Power Sources*, 306:454–458, 2016.

[161] Y. Li, S. Meyer, J. Lim, S. C. Lee, W. E. Gent, S. Marchesini, H. Krishnan, T. Tyliszczak, D. Shapiro, A. L. David Kilcoyne, and W. C. Chueh. *Adv. Mater.*, 27:6591–6597, 2015.

[162] M. Mastali Majdabadi, M. Farkhondeh, S. Farhad, R. A. Fraser and M. Fowler, Manuscript to be submitted.

[163] M. Farkhondeh, M. Pritzker, M. Fowler, and C. Delacourt. *Electrochem. Comm.*, 67:11–15, 2016.

[164] M. Farkhondeh, M. Pritzker, M. Fowler and C. Delacourt, Manuscript to be submitted.

[165] I. Thorat, D. Stephenson, N. Zacharias, K. Zaghib, J. Harb, and D. Wheeler. *J. Power Sources*, 188:592–600, 2009.

[166] Celgard LLC, Celgard 2500 Product Information.

[167] G. Kobayashi, S-I. Nishimura, M-S. Park, R. Kanno, M. Yashima, T. Ida, and A. Yamada. *Adv. Func. Mater.*, 19:395–403, 2009.

[168] J. Jamnik, R. Dominko, B. Erjavec, M. Remskar, A. Pintar, and M. Goberscek. *Adv. Mater.*, 21:A2715–2719, 2005.

[169] N. A. Siddique, A. Salehi, Z. Wei, D. Liu, S. D. Sajjad, and F. Liu. *ChemPhysChem*, 16:2383–2388, 2015.

[170] Z. Liu, T. W. Verhallen, D. P. Singh, H. Wang, M. Wagemaker, and S. Barnett. *J. Power Sources*, 324:358–367, 2015.

[171] M. Levi and D. Aurbach. *Characterization of Materials*. John Wiley and Sons, Inc., 2012.

[172] Bio-Logic potentiostat product manual.

[173] S. E. Fosdick, K. N. Knust, K. Scida, and R. M. Crooks. *Angew. Chem. Int. Ed.*, 52:10438–10456, 2013.

[174] E. A. Guggenheim. *Thermodynamics: An Advanced Treatment for Chemists and Physicists*. North Holland, 8th edition, 1986.

[175] R. E. De La Rue and C. W. Tobias. *J. Electrochem. Soc.*, 106:827–833, 1959.

[176] S. R. De Groot and P. Mazur. *Non-Equilibrium Thermodynamics*. Dover Publications, 2011.

[177] J. Liu and C. W. Monroe. *Electrochim. Acta*, 135:447–460, 2014.

[178] J. M. Smith, H. C. van Ness, and M. M. Abbott. *Introduction to Chemical Engineering Thermodynamics*. McGraw-Hills, 7th edition, 2005.

[179] S. Whitaker. *Transport in Porous Media*, 1:3–25, 1986.

[180] J. Landesfeind, A. Ehrl, M. Graf, W. A. Wall, and H. A. Gasteiger. *J. Electrochem. Soc.*, 163:A1254–A1264, 2016.

[181] A. Nabovati, E. W. Llewellin, and A. C. M. Sousa. *Compos. Manuf.*, 40:860–869, 2009.

[182] L. Grande, E. Paillard, G-T. Kim, S. Monaco, and S. Passerini. *Int. J. Mol. Sci.*, 15:8122–8137, 2014.

[183] A. Arora, J. C. T. Eijkel, W. E. Morf, and A. Manz. *Anal. Chem.*, 73:3282–3288, 2001.

Appendix A
Dependence of Potential Sensor Equilibrium Locus on Electrode Kinetic Properties

Assume that a known constant electric field is applied to the electrolyte along the z-direction and the resulting potential profile is not disturbed by the potential sensor, i.e., electric potential varies linearly along the potential sensor. Using Eqs. (6-34) and (6-35), one can obtain an analytical expression for the equilibrium locus $z_{\mathrm{eq},l}$ that separates the cathodic and anodic poles of the potential sensor [183]. Let $U_{\mathrm{PS}} = 0$ and the overpotential at the surface $\eta_{\mathrm{PS},l}(z) = \Phi_{\mathrm{PS},l}(z) - \Phi(\mathrm{z})$ be linear in z:

$$\eta_{\mathrm{PS},l}(z) = \eta_{\mathrm{PS},l}\left(z_{\mathrm{eq},l}\right) + \frac{d\eta_{\mathrm{PS},l}}{dz}\left(z - z_{\mathrm{eq},l}\right) \tag{A-1}$$

where $\eta_{\mathrm{PS},l}\left(z_{\mathrm{eq},l}\right) = 0$. Moreover, assuming a uni-potential metallic electrode (i.e., $d\Phi_{\mathrm{PS},l}/dz = 0$), the overpotential becomes:

$$\eta_{\mathrm{PS},l}(z) = -\frac{d\Phi}{dz}|_{z_{\mathrm{eq},l}}\left(z - z_{\mathrm{eq},l}\right) = E\left(z - z_{\mathrm{eq},l}\right) \tag{A-2}$$

where $E = -d\Phi/dz$ is the electric field uniform across the electrode width. On the other hand:

$$\int_a^b I_{\mathrm{PS},l}dz = \int_a^{z_{\mathrm{eq},l}} I_{\mathrm{PS},l}dz + \int_{z_{\mathrm{eq},l}}^b I_{\mathrm{PS},l}dz = 0 \tag{A-3}$$

where $a = \lambda$ and $b = \lambda + \delta$ for $l = 1$ and $a = L - (\lambda + \delta)$ and $b = L - \lambda$ for $l = 2$. By making use of Eqs. (A-2) and (6-34) and carrying out some manipulation, the integrals of Eq. (A-3) can be evaluated to yield an expression for $z_{\mathrm{eq},l}$. In the case of $z_{\mathrm{eq.1}}$ it simplifies to:

$$z_{\mathrm{eq},1} = \lambda + \frac{1}{2}\delta - \frac{RT}{nFE}\ln\left(\frac{\beta_{\mathrm{PS}}}{1-\beta_{\mathrm{PS}}}\frac{\sinh\left(-\frac{(1-\beta_{\mathrm{PS}})nF}{2RT}\delta E\right)}{\sinh\left(-\frac{\beta_{\mathrm{PS}}nF}{2RT}\delta E\right)}\right) \tag{A-4}$$

Under the condition of no local perturbation, the equilibrium locus is independent of the reaction rate constant k_{PS}^0. Moreover, one expects $z_{\mathrm{eq},l}$ to fall exactly at the middle of the electrode for a perfectly symmetric anodic/cathodic reaction, i.e., for $\beta_{\mathrm{Li}} = 1/2$, regardless of the electric field intensity. It is nonetheless interesting to note that, under the operating condition of relevance to

transport property measurement experiments, the amplitude of the electric field is small enough to allow linear approximation of the hyperbolic sine term on the right side of Eq. (A-4), i.e.:

$$\sinh\left(-\frac{(1-\beta_{\mathrm{PS}})nF}{2RT}\delta E\right) = -\frac{(1-\beta_{\mathrm{PS}})nF}{2RT}\delta E$$

and

$$\sinh\left(-\frac{\beta_{\mathrm{PS}}nF}{2RT}\delta E\right) = -\frac{\beta_{\mathrm{PS}}nF}{2RT}\delta E \tag{A-5}$$

Substitution of Eq. (A-5) into Eq. (A-4) causes the third term on the right side to vanish and shows that the equilibrium locus is unaffected by changing β_{PS}. In line with the above linear approximation, a plot of the percent difference in $z_{\mathrm{eq},1}$ according to Eq. (A-4) in Figure A-1 demonstrates less than 0.5% variation in $z_{\mathrm{eq},1}$ of an electrode regardless of the value of β_{PS} when exposed to an electric field as high as $E = 6.16\ \mathrm{V\ m^{-1}}$. Such an electric field is equivalent to the potential gradient along the centerline of the cell containing 1 M $LiPF_6$ in EC/DEC and operating at $I_{\mathrm{app}} = 0.2\ \mathrm{mA}$ at $t = 8\ \mathrm{h}$ (i.e., maximum potential gradient during the galvanostatic polarization experiment).

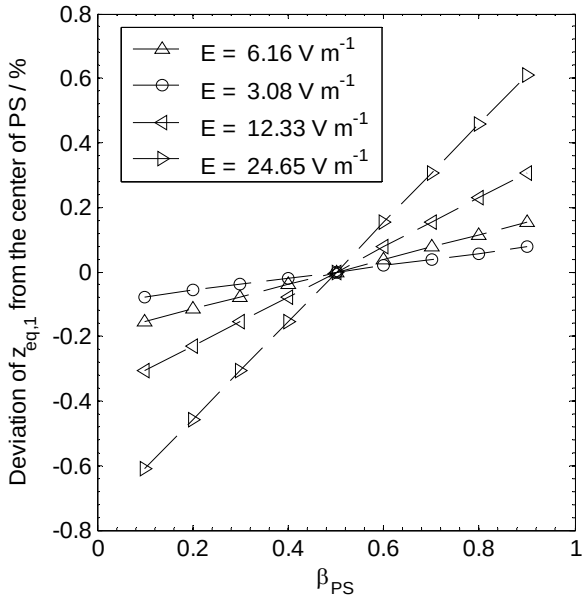

Figure A-1. Variation of the equilibrium locus of PS,1 as a function of charge-transfer coefficient exposed to electric fields with different amplitudes assuming no local perturbation (i.e., Eq. (A-4)).